

ELECTROLUMINESCENCE FROM ZINC SULFIDE THIN FILMS
DOPED WITH ERBIUM TRIFLUORIDE

By

DAVID MICHAEL DEVITO

A DISSERTATION PRESENTED TO THE GRADUATE SCHOOL
OF THE UNIVERSITY OF FLORIDA IN PARTIAL FULFILLMENT
OF THE REQUIREMENTS FOR THE DEGREE OF
DOCTOR OF PHILOSOPHY

UNIVERSITY OF FLORIDA

2006

Copyright 2006

by

David Michael DeVito

This work is dedicated to my family.

ACKNOWLEDGMENTS

So many people have helped me along this journey. It is impossible to name everyone whose effort has allowed me to achieve my goals and dreams. However, there are a few people, who through their help and support, I owe a special note of gratitude.

First, I would like to thank my advisor and mentor, Dr. Paul Holloway. The amount of knowledge I have gained from him is staggering. He has been there to support me in my personal and academic life. His constant dedication to his work and his students is an inspiration and a standard by which I will always measure myself throughout my entire career. I owe him a great deal of appreciation, and it has been an honor and a privilege to work for him.

I would like to thank Dr. Mark Davidson for his unending support and assistance throughout my work. From my very first job working with Mark, I knew I had met someone who would push me to achieve goals I did not know I could. I would also like to thank Maggie Puga-Lambers, for her tireless help, and all those at Microfabritech, especially Diane Badylak, Scott Gapinski and Chuck Rowland, for their continued assistance throughout this research. I greatly appreciate the assistance and guidance of all of my committee members as well.

As anyone who has worked in Dr. Holloway's research group knows, Ludie Harmon is the smile that brings brightness to the office every day. I appreciate all Miss Ludie's help. A number of Dr. Hollway's students, both past and present, have helped me with this research. I would like to thank, most especially, Ajay, Bill, Jie, Nigel, Jason,

Narada, Evan, Marc, Phil and Bryan and all the other members of Dr. Holloway's group for their friendship and support.

Without the thorough support of my parents, none of this would be possible. I would like to thank Mom for her help through all those years when I did not seem to know which end was up. Her love and support always makes me smile. I hope I was not too much trouble. I would like to thank Dad. I always know that he will be my biggest supporter no matter what avenue I pursue in life. Maybe someday he will be able to tell his grandchildren a story about me, over and over again. I would like to thank Jean-Paul. He has always driven me to achieve my potential and been willing to talk late into the night, even though I knew that he was exhausted. I would like to thank Allison, who is the best sister anyone could ever hope for. She makes me smile and has been a source of inspiration for me my entire life. I must thank all my grandparents, whose example has cause me to be a better man. I love them all.

I cannot thank all my family and friends enough for helping me to become the person I am today. They have all contributed greatly to my development. I would also like to thank *The Maury Povich Show* for providing me with all the proof I need that continuing education is important as I have occasionally watched this show while writing and writing and writing. I am the proud father of my wonderful Dolly. She is the perfect assistant for dissertation writing. She gladly sits on my papers and demands attention when I am deep in thought. But she is very cuddly and loving, and that helps.

Finally, I would like to thank my beautiful wife, Allyson. She has guided and supported me through this research, providing inspiration and care. She has given me so much love, and sometimes a needed push, during this work. So many more words are

needed to express how much she means to me and how much better I have become because of her. I could not have done this without her. Thank you!

TABLE OF CONTENTS

	<u>page</u>
ACKNOWLEDGMENTS	iv
LIST OF TABLES	x
LIST OF FIGURES	xi
ABSTRACT	xiv
1 INTRODUCTION	1
2 LITERATURE SURVEY	2
2.1 Introduction.....	2
2.2 Electroluminescence	4
2.3 ACTFEL Device Structure	8
2.4 ACTFEL Device Physics.....	11
2.4.1 Tunnel Injection.....	12
2.4.2 High Field Transport	14
2.4.3 Impact Excitation.....	15
2.4.4 Radiative Decay.....	17
2.4.5 Optical Outcoupling	17
2.5 ACTFELD Materials	19
2.5.1 Substrate Materials	19
2.5.2 Insulating Materials	20
2.5.3 Transparent Conductors.....	23
2.5.4 Opaque Electrode	23
2.5.5 Phosphor Materials.....	24
2.5.5.1 Host materials.....	24
2.5.5.2 Luminescent centers.....	25
2.5.6 ZnS:ErF ₃ as an ACTFEL Phosphor.....	30
2.6 ACTFELD Characterization.....	33
2.6.1 Optical Characterization.....	33
2.6.2 Electrical Characterization	35
2.6.2.1 Equivalent circuit models of ACTFELDs.....	35
2.6.2.2 Electrical characterization.....	37
3 EXPERIMENTAL PROCEDURE.....	42

3.1	ACTFEL Device Fabrication.....	42
3.1.1	Substrate Preparation.....	42
3.1.2	Thin Film Deposition.....	42
3.1.3	Post-Deposition Annealing.....	45
3.1.4	Electrode Deposition.....	46
3.2	ACTFEL Characterization.....	46
3.2.1	Thickness Measurements.....	46
3.2.2	Electroluminescence Measurements.....	46
3.2.3	Photoluminescence Measurement [101].....	48
3.2.4	Energy Dispersive Spectroscopy [102].....	48
3.2.5	Electron Probe Micro Analysis [103].....	49
3.2.6	Secondary Ion Mass Spectroscopy [101].....	50
3.2.7	Electrical Measurements.....	50
3.2.8	Statistical Analysis.....	51
4	EFFECTS OF PHOSPOR LAYER PROCESSING PARAMETERS ON ELECTROLUMINESCENCE AND CHEMICAL COMPOSITION.....	52
4.1	Introduction.....	52
4.2	Experimental Procedure.....	54
4.2.1	Substrate.....	55
4.2.2	Phosphor Layer Deposition.....	56
4.2.3	Top Opaque Electrode.....	57
4.2.4	Chemical Composition Analysis.....	57
4.3	Processing Parameters.....	59
4.3.1	Substrate Temperature.....	59
4.3.2	Duty Cycle Applied to Doped Target.....	63
4.3.3	Sputtering Gas Pressure.....	66
4.3.4	Post-Deposition Annealing Temperature.....	69
4.4	Discussion.....	72
4.5	Summary.....	85
5	EFFECTS OF PROCESSING PARAMETER INTERACTIONS ON ELECTROLUMINESCENCE AND CHEMICAL COMPOSITION.....	88
5.1	Introduction.....	88
5.2	Experimental Procedure.....	88
5.2.1	Substrate.....	88
5.2.2	Phosphor Layer Deposition.....	89
5.2.3	Chemical Composition Analysis.....	90
5.3	Effects of Processing Parameter Interactions.....	90
5.3.1	Effects on Erbium Concentration.....	90
5.3.2	Effects on Fluorine concentration.....	91
5.3.4	Effects on Threshold Voltage.....	92
5.3.4	Effects on Electroluminescent Brightness.....	93
5.4	Discussion.....	96
5.5	Summary.....	100

6	DISCUSSION.....	102
6.1	Introduction.....	102
6.2	Processing Parameter Effects on ZnS:ErF ₃ ACTFELDs.....	103
6.3	Interaction of Processing Parameter Effects.....	106
6.4	Statistical Data Analysis.....	109
7	CONCLUSIONS.....	112
7.1	Processing Parameter Effects.....	112
7.2	Processing Parameter Interactions.....	114
7.3	Experimental Evaluation.....	116
7.4	Future Work.....	117
	LIST OF REFERENCES.....	118
	BIOGRAPHICAL SKETCH.....	125

LIST OF TABLES

<u>Table</u>	<u>page</u>
2.1 Major developments of high-field electroluminescence in ZnS	6
2.2 Requirements for dielectric layers.....	21
2.3 Insulators used for ACTFEL devices and their properties	22
2.4 Properties of some II-VI ACTFEL host materials	25
2.5 Comparison of visible emission from ACTFEL phosphors.....	30
2.6 Properties of different zinc sulfide phases.	31
4.1 Processing parameters and Er and F concentrations for ZnS:ErF ₃ phosphors.....	62
4.2 Comparison of P-values for processing parameters.....	73
5.1 Processing parameters for ZnS:ErF ₃ phosphors.....	89
5.2 Comparison of P-values for processing parameter interactions.....	96

LIST OF FIGURES

<u>Figure</u>	<u>page</u>
2.1 Cross-section schematics of (a) “normal” double-insulating structure, (b) “inverted” structure and (c) “half stack” structure	11
2.2 Energy band diagram illustrating the physical processes that produce electroluminescence in zinc sulfide devices.....	12
2.3 Electron energy distribution in ZnS as a function of energy for different phosphor fields using a full-band structure model [50].	15
2.4 Schematic illustration for internal reflection in ZnS:Mn ACTFEL device [12].	18
2.5 Transmission spectrum for Corning 7059 glass [60].	20
2.6 Schematic illustration of shielding of inner $4f$ orbital of a rare earth ion by the outer $5s$, $5p$, and $6s$ shells.....	27
2.7 Partial energy level diagrams for Neodymium, Erbium and Thulium in ZnS [82, 83].....	28
2.8 Emission peaks from ZnS:ErF ₃ [98].	32
2.9 Typical Brightness versus Voltage for ACTFELD	34
2.10 Equivalent circuit models for ACTFELDs modeled as (a) a capacitor in parallel with a non-linear resistor and (b) as two back-to-back Zener diodes [61].....	36
2.11 Schematic of a Sawyer-Tower bridge circuit [53].	38
2.12 Diagram of the trapezoidal voltage waveform used in ACTFEL device operation and testing.	39
2.13 Schematic of Q-V plot for ACTFEL device. [V_{to} : electrical turn-on voltage, Q_{cond} : conduction charge, Q_{pol} : polarization charge, Q_{leak} : leakage charge, Q_{relax} : relaxation charge] Lettering refers to labels for voltage waveform in Figure 2.11..	40
3.1 Schematic of sputter deposition system used for RF magnetron sputter deposition of ZnS:ErF ₃	44
3.2 Schematic of thermal annealing furnace utilizing lamps as heating elements.....	45

3.3	Schematic of optical bench for EL/PL measurement.....	47
4.1	Energy levels and transitions of ZnS:ErF ₃ ACTFELDs that produce luminescence shown in Figure 4.2 and Figure 4.3 [79].	53
4.2	Typical visible emission at 525 and 550 nm for ZnS:ErF ₃ ACTFEL devices.	54
4.3	Typical near infrared emission at 1550 nm for ZnS:ErF ₃ ACTFEL devices.	54
4.4	Schematic of the process flow for ZnS:ErF ₃ ACTFEL devices fabrication.....	55
4.5	Typical negative ion SIMS spectrum for as-deposited ZnS:ErF ₃ phosphor layer. ...	58
4.6	Typical negative ion SIMS spectrum for ZnS:ErF ₃ phosphor layer after annealing at 425°C for 1 hr in N ₂	58
4.7	Effect of deposition temperature on threshold voltage for ZnS:ErF ₃ ACTFELDs. .	60
4.8	Effect of deposition temperature on B ₂₀ for ZnS:ErF ₃ ACTFELDs.	61
4.9	Effect of deposition temperature on Er/Zn ratio for ZnS:ErF ₃ phosphor films.....	61
4.10	Effect of deposition temperature on F concentration [cm ⁻³] for ZnS:ErF ₃ phosphor films.	62
4.11	Effect of duty cycle on threshold voltage for ZnS:ErF ₃ ACTFELDs.	64
4.12	Effect of duty cycle on B ₂₀ for ZnS:ErF ₃ ACTFELDs.....	64
4.13	Effect of duty cycle on Er/Zn ratio for ZnS:ErF ₃ phosphor films.....	65
4.14	Effect of duty cycle on F concentration [cm ⁻³] for ZnS:ErF ₃ phosphor films.....	65
4.15	Effect of Ar sputtering gas pressure on threshold voltage for ZnS:ErF ₃ ACTFELDs.	67
4.16	Effect of Ar sputtering gas pressure on B ₂₀ for ZnS:ErF ₃ ACTFELDs.	67
4.17	Effect of Ar sputtering gas pressure on Er/Zn ratio for ZnS:ErF ₃ phosphors.	68
4.18	Effect of Ar sputtering gas pressure on F concentration [cm ⁻³] for ZnS:ErF ₃ phosphors.	68
4.19	Effect of post-deposition annealing on threshold voltage for ZnS:ErF ₃ ACTFELDs.	69
4.20	Effect of post-deposition annealing on B ₂₀ for ZnS:ErF ₃ ACTFELDs.	70
4.21	Effect of post-deposition annealing on Er/Zn ratio for ZnS:ErF ₃ phosphors.....	70

4.22	Effect of post-deposition annealing on F concentration [cm^{-3}] for ZnS:ErF ₃ phosphors.	71
4.23	Effect of post-deposition annealing on O/ZnS ratio for ZnS:ErF ₃ phosphors.	71
4.24	Effect of all experimental parameters on threshold voltage for ZnS:ErF ₃ ACTFELDs.	74
4.25	Effect of all experimental parameters on B ₂₀ for ZnS:ErF ₃ ACTFELDs.....	75
4.26	Effect of all parameters on Er/Zn ratio for ZnS:ErF ₃ phosphor films.....	75
4.27	Effect of all parameters on F concentration [cm^{-3}] for ZnS:ErF ₃ phosphor films....	76
4.28	Normal probability plot of threshold voltage data values.	81
4.29	Normal probability plot of B ₂₀ data values.	81
4.30	Normal probability plot of Er/Zn ratio values.....	82
4.31	Normal probability plot of F concentration values.	82
4.32	Effect of order of data collection on threshold voltage data values.....	83
4.33	Effect of order of data collection on B ₂₀ data values.	84
4.34	Effect of order of data collection on Er/Zn ratio values.....	84
4.35	Effect of order of data collection on F concentration values.	85
5.1	Effect of interaction of duty cycle (25 and 75%) and Ar gas pressure (1 and 24 mTorr) on Er concentration.....	91
5.2	Effect of interaction of deposition temperature (120 and 150°C) and Ar gas pressure (1 and 24 mTorr) on F concentration.....	92
5.3	Effect of interaction of deposition temperature (120 and 150°C) and Ar gas pressure (1 and 24 mTorr) on V _{th}	93
5.4	Effect of interaction of deposition temperature (120 and 150°C) and duty cycle (25 and 75%) on B ₂₀	94
5.5	Effect of interaction of deposition temperature (120 and 150°C) and Ar gas pressure (1 and 24 mTorr) on B ₂₀	95
5.6	Effect of interaction of duty cycle (25 and 75%) and Ar gas pressure (1 and 24 mTorr) on B ₂₀	95

Abstract of Dissertation Presented to the Graduate School
of the University of Florida in Partial Fulfillment of the
Requirements for the Degree of Doctor of Philosophy

ELECTROLUMINESCENCE FROM ZINC SULFIDE THIN FILMS DOPED WITH
ERBIUM TRIFLUORIDE

By

David Michael DeVito

May 2006

Chair: Paul H. Holloway

Major Department: Materials Science and Engineering

Near infrared emission at a wavelength of 1.55 μm from zinc sulfide (ZnS) doped with erbium trifluoride (ErF_3) has been studied in alternating current thin film electroluminescent devices (ACTFELDs). The thin film phosphors were deposited by radio frequency (RF) planar magnetron sputtering of a 1.5 mol% ErF_3 -doped ZnS target and an undoped ZnS target. The intensity of near infrared emission is related to the processing parameters used in film deposition and post-deposition annealing. Thin films, approximately 650 nm thick, were deposited at 100 W from both targets. Deposition temperature, duty cycle, sputtering gas pressure and post-deposition annealing temperature were varied in a design-of-experiment. As deposition temperature was increased from 120 $^\circ\text{C}$ to 150 $^\circ\text{C}$, the near infrared electroluminescence increased by ~180% at an operating voltage 20 volts above the threshold voltage (B_{20}). This is attributed to better activation of erbium luminescent centers on zinc lattice sites results in a greater number of radiative events, increasing luminescence. Increasing the duty cycle

applied to the ZnS:ErF₃ doped target from 25% to 75%, increased the electroluminescence at B₂₀ by ~650%. This likely results from a greater number of ErF₃ dopants incorporated into the phosphor. As the sputtering gas pressure increases from 1 mTorr to 24 mTorr, the electroluminescence at B₂₀ increases by ~80%. At lower pressure, the phosphor undergoes negative ion resputtering removing zinc and sulfur from the film. This creates a film with a higher proportion of ErF₃ dopant incorporated. After film deposition, a portion of the phosphor films underwent annealing for 1 hour in ultra high purity nitrogen at 425 °C. Annealing films increased electroluminescence at B₂₀ by ~60%. The increase in brightness correlated with a reduction in fluorine incorporation in the film. Additionally the number of sulfur vacancies is likely reduced. This probably alters the local crystal field around the erbium dopant allowing for more adequate pathways for the near-infrared transitions, thus increasing the overall near infrared luminance. The highest brightness was observed for a deposition temperature of 150 °C, a duty cycle of 75%, argon sputtering gas pressure of 24 mTorr and post-deposition annealing at 425 °C. These conditions resulted in a brightness of the 1550 nm emission peak of 146.46 μW/cm² at 20 V above threshold.

CHAPTER 1 INTRODUCTION

Thin film electroluminescent display devices have emerged as a capable competitor to current flat panel display technologies. Commercially available displays have been developed from visible light emission of zinc sulfide doped with manganese [1-6]. As competition for share in the visible flat panel display marketplace has increased, a great deal of research has dealt with visible emission to the neglect of infrared (IR) emission from these devices. Infrared emission is used in a number of applications both consumer and military, including telecommunications, phototherapy, chemical detection, friend-foe identification, and other night-vision technologies.

This research deals with zinc sulfide (ZnS) doped rare earth fluoride thin films doped with erbium trifluoride (ErF_3) in a traditional metal-insulator-semiconductor-insulator-metal (MISIM) structure as a source for IR emission (primarily the 1550 nm transition in Er) and the compositional changes that result from processing.

Chapter 2 will present a relevant literature survey of ACTFEL devices, their structure, operating physics and their material composition. Chapter 3 will consist of the experimental and characterization methods used to study ZnS:ErF₃ devices. Chapter 4 will focus on the electroluminescence emission produced and the chemical composition changes related to device processing. In chapter 5, interactions between processing parameters of these devices will be presented. Chapter 6 will provide discussion of the results from the preceding chapters to explain observed phenomena. Finally conclusions will be presented in chapter 7.

CHAPTER 2 LITERATURE SURVEY

2.1 Introduction

Since the advent of television in 1929, displays have become an integral part of our lives. Traditional cathode ray tubes (CRT) have enjoyed decades as the primary means of visual display. Over the past decade, a paradigm shift has occurred in which flat panel displays (FPD) have begun to push CRT displays out of the marketplace [7]. The dramatic increase in demand for FPDs coincides with increased demand for cellular telephones, portable electronics devices and laptop computers. Flat panel technology has also made inroads into the home in the form of flat panel computer monitors and flat panel televisions. With market forces pushing for ever-advancing technology, continued research and development are vital to the future success of flat panel displays.

Flat panel displays encompass multiple different types of technology including liquid-crystal displays (LCD), plasma displays, field emission displays and thin film electroluminescent displays (TFELDs) [7]. Currently liquid crystal displays dominate the market, accounting for approximately 85% of all FPDs [8]. However, a variety of consumer, military and medical applications exist in which a display is needed that compensates for the weaknesses of LCDs. TFELDs offer several advantages such as a wide viewing angle ($>160^\circ$), high contrast in high ambient illumination conditions, broad operating temperature range (-60°C to $+100^\circ\text{C}$), fast response times (several μsec), very high resolution, legibility and ruggedness [9]. Alternating current thin film

electroluminescent displays (ACTFELD) have become one of the most reliable and stable currently available displays for aggressive environments [3]. ACTFEL displays can currently be produced that range from large scale monitor displays to SVGA displays smaller than a postage stamp. Because ACTFELDs possess the above useful characteristics they have great potential in a number of nontraditional applications. Of great interest is the use of infrared (IR) emitting ACTFELDS for industrial and military applications.

Gas sensing equipment may operate by observing the absorption of specific wavelengths of light. When emission wavelengths are centered at characteristic bending and stretching moments of molecular bonds, absorption of the chosen wavelength is proportional to the number of molecules in the light path [10]. Thermal sources, usually tungsten lamps, serve as these light sources. With further development, however, semiconductor based sources, like ACTFELDs, could replace these lamps and provide decreased cost through longer lifetimes.

Additionally, the United States Armed Forces can utilize IR emitting devices in a number of applications. Beginning with the development of IR sniper scopes in World War II, military interest in night vision has steadily increased. With the advantage of surprise afforded through nighttime combat, the military must seek ways to identify friend from foe to avoid friendly-fire casualties. Friend-foe identification has been of interest since British anti-aircraft artillery needed a method to distinguish British from German planes [11]. IR emission can also be utilized as means for more traditional displays for use in total darkness missions where use of visible displays may give away troop movement or positioning.

Research into a number of different electroluminescent phosphor systems exists. The review given here emphasizes the use of phosphors emitting in the near infrared region. The reader is referred to excellent reviews of EL emission in the visible region [12-14].

2.2 Electroluminescence

A phosphor is a material that emits photons when excited by a source of energy. This energy may be photonic, electronic, ionic or thermal in nature. Short periods of emission, those that cease within a few nanoseconds, are known as fluorescence [15]. Phosphorescence is luminescence over a much longer duration, lasting as long as several hours [16]. Photoluminescent devices contain phosphors that are excited by higher energy photon sources typically producing a lower energy emission. Typical photoluminescent sources are ultraviolet lamps and lasers [17]. Cathodoluminescent phosphors produce photons when struck by energetic electrons [18]. One of the most common cathodoluminescent systems is a standard cathode ray tube in a television. Electroluminescent devices produce emission when an electric field is applied across the phosphor [19]. It is this last kind of luminescence that is of most interest in this work.

Electroluminescence (EL) has experienced both high and low points in its interest as a form of light emission. EL began with the discovery by Destriau in 1936 that a high electrical field applied to an oil suspension of zinc sulfide doped with copper would produce green light [20]. This device led to the modern powder EL cell. This work became the first published report of electroluminescence. It was not until 1950, with the development of ZnO_2 , that international interest in electroluminescent research truly took off in earnest. Efforts at that time focused mainly on powder phosphors for use in lighting applications. A patent was issued to GTE Sylvania for just such an AC EL powder lamp

in 1952 [13]. Unfortunately these lamps were unable to produce the desired brightness over the minimum commercially accepted lifetimes (approximately 500 hours), and interest in them waned. [6].

Electroluminescence research experienced a rebirth in the 1960s with interest in display technologies and the advent of a number of advances in materials science and physical electronics. Though most research focused on thin film EL, Vecht produced the first DC EL powder panel in 1968 [21]. In Vecht's device the optically active layer was ZnS powder particles coated with copper ions embedded in a binder. This was similar to the earliest experiments in EL. Kahng, also in 1968, produced an AC driven device using Lumocens, which stands for luminescence from molecular centers [22]. He proposed that impact excitation of luminescent centers by "hot" electrons was the mechanism by which electroluminescence occurred.

The proposal of the insulating layer/phosphor/insulating layer sandwich structure was the first major milestone of TFEL display technology when it was proposed by Russ and Kennedy in 1967 [23]. Inoguchi *et al.* [24] at Sharp Central Research Labs utilized the double-insulating sandwich structure to produce stable, high luminance AC driven EL panels with exceptional lifetimes using zinc sulfide doped with manganese as the phosphor layer. The ZnS:Mn phosphor layer emitted yellow light, and the early TFEL displays monochrome. As a result of this work, alternating current thin film electroluminescent devices (ACTFELDs) have been more aggressively investigated for their potential use in flat panel display technologies. Uede *et al.* [25] and Takeda *et al.* [26] produced the first practical EL ZnS:Mn display units in 1981. This work allowed Sharp to introduce the first commercial ZnS:Mn thin film display in 1983 [24,27].

Throughout the 1980s other companies, including Planar Systems and Finlux, began producing EL devices to meet increasing consumer demand.

The use of zinc sulfide doped with manganese for the phosphor layer limited the color options in these devices. As such, Sharp and Planar used color filtering to produce red and green light enabling the manufacture of multicolor ZnS displays. Significant effort was made to find additional dopants that might accelerate the development of full-color displays. This led to the utilization of ZnS doped with rare earth ions to emit red, green and blue light [28,29]. Table 2.1 summarizes some of the major developments of electroluminescence in ZnS.

Table 2.1 Major developments of high-field electroluminescence in ZnS

1936	High-field electroluminescence from ZnS discovered by Destriau.
1950	Transparent electrically conductive zinc oxide developed.
1950s	Development and basic studies of AC powder EL devices. GTE Sylvania obtains a patent for powder EL lamp. Problems include low brightness, short lifetimes, poor contrast, and high operating voltages among others. Research and commercial interest fades.
1960	Electroluminescence in thin film ZnS:Mn described by Vlasenko and Popkov.
1960s	Thin film EL research by Soxman and Ketchpel. Reported in 1972.
1967	Breakthrough of double insulating layer AC thin film device structure proposed by Russ and Kennedy.
1968	Pioneering work by Kahng reported high luminescence EL from ZnS:TbF ₃ thin film phosphors, and described impact excitation. Coined term Lumocen, luminescence from molecular centers.
1968	Vecht demonstrates first DC driven powder EL panel.
1974	Inoguchi and his coworkers report first ZnS:Mn high luminance, long lifetime AC thin film EL panels. Device structure earlier proposed by Russ and Kennedy.
1974	Mito <i>et al.</i> showed that thin film EL panels could be used for TV imaging.
1981	Uede, Takeda and their coworkers reported on the production of practical ZnS:Mn AC thin film display units.
1983	Sharp introduces the first commercial ZnS:Mn AC thin film monochrome display.
1988	Prototype full-color thin film EL display demonstrated by Barrow and coworkers.
1990s	Alternating-current powder EL devices developed for specialty lighting.
1993	First commercial multicolor (red/green/yellow) ZnS:Mn AC thin film EL display introduced by Cramer <i>et al.</i>
1994	First commercial full-color AC thin film EL display panel.

An interesting result of research into the use of ZnS doped with rare earth ions for ACTFELDs was their infrared emission. This emission was seen primarily as undesired since it robbed the devices of efficiency from the visible emission. Thulium doped ZnS is a weak blue emitting phosphor and has seen little use in display devices, but does exhibit strong near infrared (NIR) emission [30]. Zinc sulfide doped with neodymium and erbium is also known to emit in both the visible and infrared regions. Erbium produces green emission with much weaker red emission and neodymium emits in the orange region. Erbium is of specific interest in the telecommunications industry where its emission at $1.54\mu\text{m}$ is commonly used [31].

Strontium sulfide has also been studied as a rare earth phosphor host. SrS is an excellent host for devices that emit in the blue due to its exceptional high-field transport properties [32]. However, ZnS serves as a better infrared host due to the fact that ‘hot’ electrons do not have enough energy to excite shorter wavelength (higher energy) transitions [33]. As a result the ratio of NIR to blue emission in ZnS is higher as compared to SrS.

A number of other sources exist for production of infrared light other than ACTFELDs. These include light emitting diodes (LEDs), lasers and thermal emitters. Infrared LEDs are analogous to visible LEDs. Rare earth phosphors may also be used to down-convert the visible emission from an LED to NIR emission by depositing the phosphor on the semiconductor chip. Such a design faces a potentially substantial loss of efficiency [34]. Infrared lasers face a number of different problems chief among them is a lack of long-term stability due to variations in amplitude when wavelength modulated [35]. Additionally they become unstable at temperatures above 150°C . Both LEDs and

lasers are point sources of light, in contrast to ACTFELs which can be made over large areas.

Thermal emitters, also known as globars, function similarly to a standard incandescent light bulb. Globars are made of silicon carbide that is heated to a desired temperature. The globar's emission approximates that of a blackbody radiator at the same temperature [36]. Because the temperatures of operation are relatively low (<1000 K), thermal emitters are not very efficient at light production. They also produce light across a broad spectrum that must be filtered if a specific wavelength is sought. As a result of the drawbacks to these other infrared emitters, ACTFELs possess the potential to supplant all of them as infrared light emitting devices in a number of applications.

2.3 ACTFEL Device Structure

The initial double insulating sandwich structure that was proposed by Russ and Kennedy and utilized by Inoguchi has been adapted over the years to what is now the most common device structure. This structure is the standard MISIM (metal-insulator-semiconductor-insulator-metal), or "full stack" structure [37] as shown in Figure 2.1 (a). This design uses a transparent substrate, typically glass, with a transparent electrode deposited on top of it. A transparent insulator, phosphor layer, second insulating layer and opaque electrode are deposited in corresponding order. Emitted light is transmitted through the glass substrate, transparent electrode and transparent bottom insulator to the viewer. A darker top insulating layer may be used to enhance contrast, as well as use of a reflecting opaque electrode to increase overall brightness.

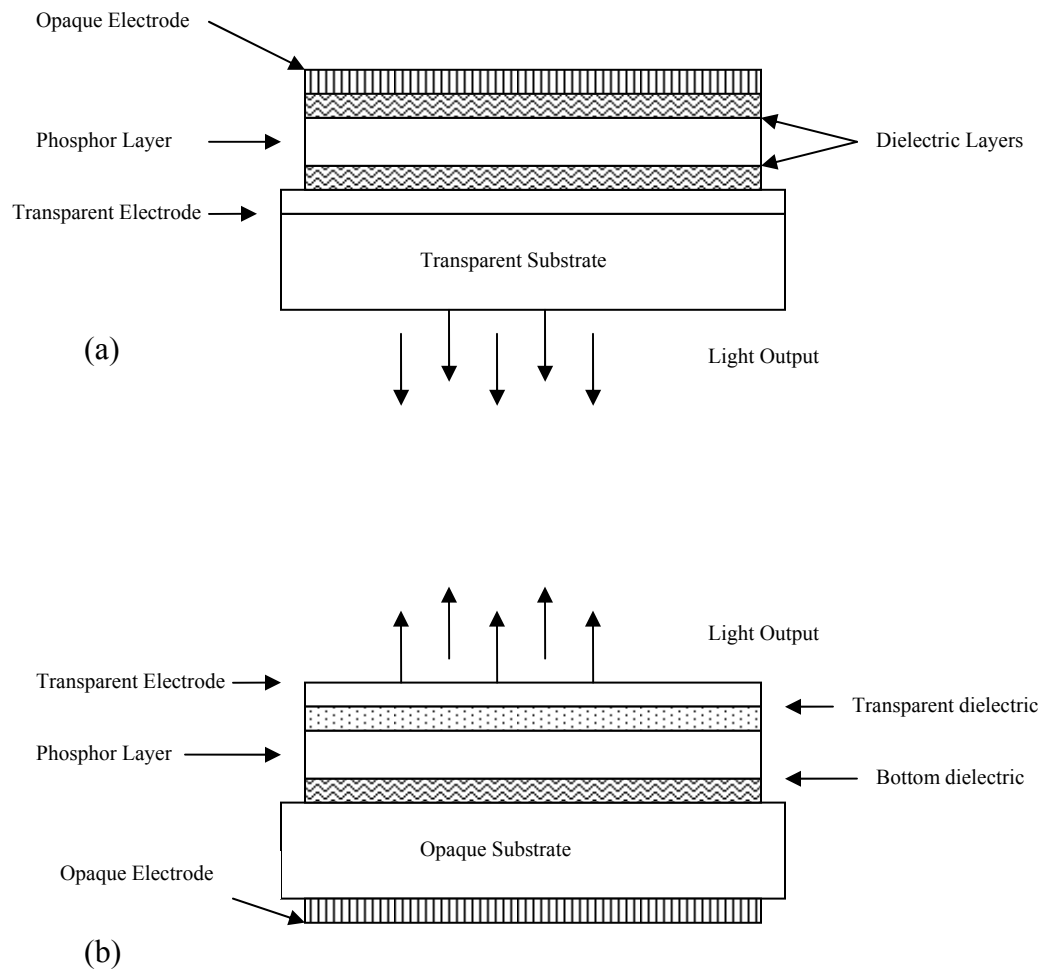
A number of distinct advantages exist for this structure, chief among them being the use of inexpensive glass substrates that are easily produced in almost any size. Another advantage is the use of aluminum for the rear opaque electrode. Aluminum is

highly reflective and possesses the ability to “self heal” when the proper rear insulator is chosen. “Self healing” describes the phenomenon that occurs when microscopic shorts develop in the phosphor layer so they cannot propagate through the film and cause catastrophic breakdown [38]. Self healing limits failure to a localized region due rapid fusing of the aluminum electrode by the large current flow from a short circuit.

An analog to the “normal” structure is the “inverted” structure. This is another common device structure in which the substrate is opaque and the top insulator and electrode are transparent [12, 39]. This structure is utilized in designs for active matrix and thick film dielectric hybrid EL devices [40, 41]. The structure shown in Figure 2.1 (b) shows the bottom electrode on the opposite side of the substrate from the phosphor. In this case the substrate is both the support structure and a dielectric layer. A high dielectric material such as BaTiO_3 may be chosen for such a design [42].

One distinct advantage of the “inverted” has over “normal” structure is the ability to use an opaque substrate. Ceramic substrates may be used that allow higher temperature device processing. This type of processing helps to optimize phosphor microstructure and subsequent performance. Silicon substrates may also be used allowing devices to be incorporated into a large number of silicon-based semiconductor devices. Inverted structures also make very simple the addition of organic filters after higher temperature processing steps are complete. Full and multicolor display applications that utilize these filters are easier to produce in inverted structures, as opposed to the normal structure where filters must be deposited before the phosphor layer. A great disadvantage however is the inability to use aluminum as the top electrode. Because the top electrode must be transparent, the “self healing” features that can be used in “normal” devices are lost.

An additional device type, shown in Figure 2.1 (c), is called the “half stack” structure used for device testing. This device may be similar to either the “normal” full stack and “inverted” structures, except there is only one insulating layers. In the standard “half stack”, the top insulating layer is omitted saving an additional processing step. This may limit or enhance the device performance in terms of brightness [43], but invariably decreases the stability, as compared to structures with top and bottom insulating layers. This device structure is used primarily for research purposes due to its relatively faster processing time.



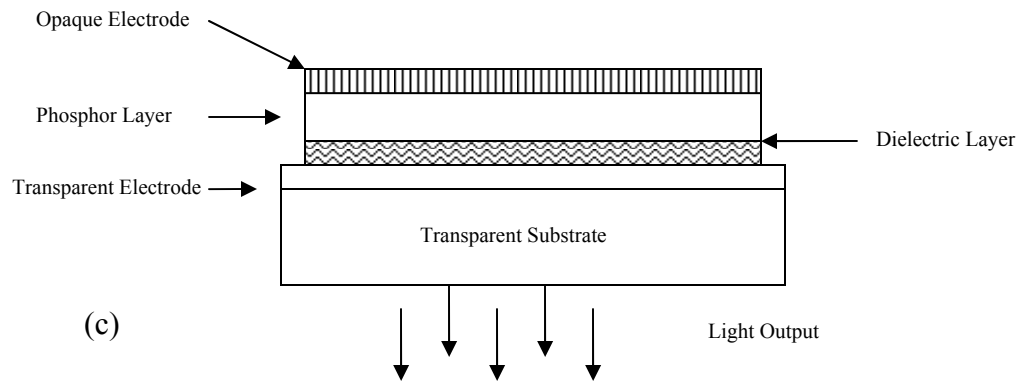


Figure 2.1 Cross-section schematics of (a) “normal” double-insulating structure, (b) “inverted” structure and (c) “half stack” structure

2.4 ACTFEL Device Physics

This section will describe the basic physical processes and the interrelations that lead to high-field electroluminescence in zinc sulfide devices. Electroluminescence occurs when an electric field is applied to a luminescent material with sufficient energy to generate charge carriers that can impact excite or impact ionize luminescent centers. Impact excitation and impact ionization are differentiated by the resulting valence state of the activator (dopant) following electron impact [44]. In cases of impact excitation, the valence of the activator does not change but the valence electrons are raised from the ground to an excited (higher) energy configuration. Impact ionization, however, results from delocalization of a valence electron into the conduction band continuum, resulting in an ionized center. Figure 2.2 shows an illustration of the physical processes that occur during operation of an ACTFEL device.

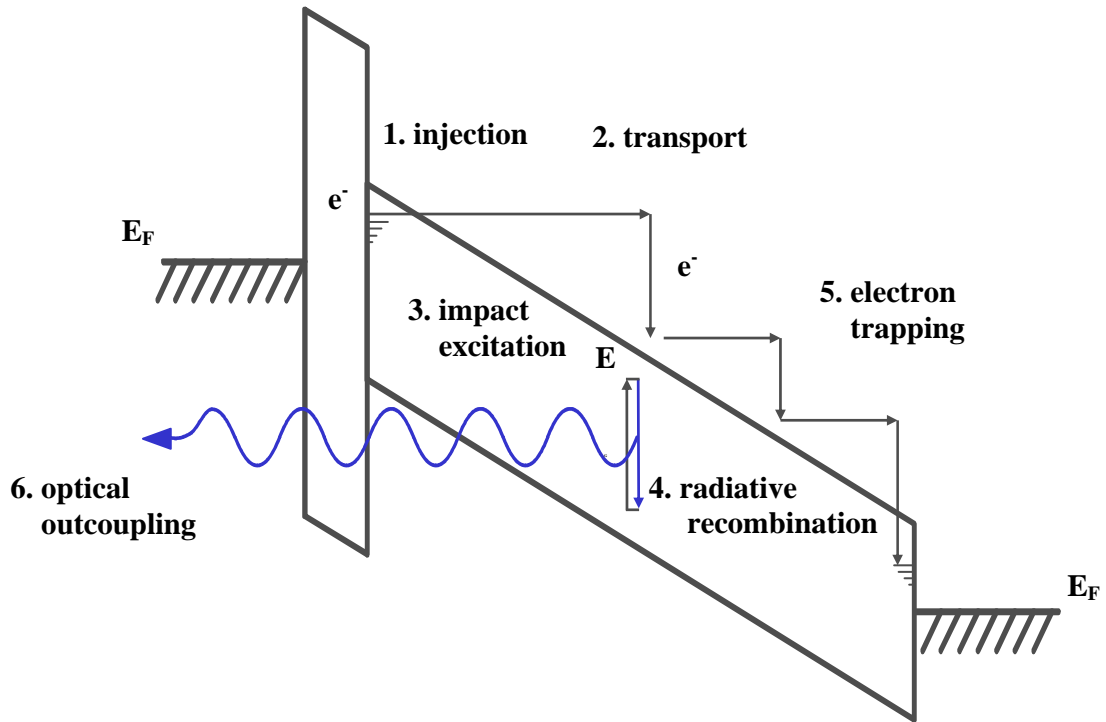


Figure 2.2 Energy band diagram illustrating the physical processes that produce electroluminescence in zinc sulfide devices.

In Figure 2.2 the following processes take place:

1. Interface state electrons tunnel into the conduction band of the phosphor under the applied field.
2. Electrons are accelerated to ballistic energies during high-field transport across the phosphor. Impact scattering can result in electron-hole production; leading to electron multiplication in the host.
3. Luminescent centers are impact excited.
4. Radiative de-excitation of impact excited centers results in emission of light.
5. Electrons are trapped at the anode interface, resulting in a counter field that stops current flow [50].
6. Optical outcoupling allows a portion of the generated light to escape.

2.4.1 Tunnel Injection

Two general mechanisms are responsible for carrier injection, thermionic emission and field emission or tunneling [45]. A number of experiments support the fact that electrons trapped at the phosphor/insulator interface are the source of carriers for these

devices and that thermally-assisted electron tunneling is the main mechanism for charge injection. Commercial ACTFEL displays are driven at 60Hz with 30 microsecond pulses and an 8 microsecond rise and fall time. As the applied electric field reaches a sufficiently large value ($\sim 1-2$ MV/cm), the energy bands are bent such that electrons trapped at interface states (and those trapped in deep states throughout the phosphor) tunnel into the phosphor conduction band. The critical value for the voltage at which this occurs is called the threshold voltage.

The insulator/phosphor interface can be modeled as a Schottky barrier. The tunnel current (J) through a Schottky barrier is given by [46]:

$$J \approx E^2 \exp \left[\frac{-8\pi \sqrt{2m^*} (q\Phi B)^{3/2}}{3qhE} \right] \quad (2.1)$$

where E is the electric field, m^* is the effective electron mass, q is the charge of an electron, ΦB is the barrier height and h is Planck's constant. To apply this equation to electron trap state emission, the barrier height must be replaced with the interface trap depth. The ideal interface trap energy should be deep enough so that the threshold fields are adequate to accelerate electrons, but shallow enough to avoid excessively high fields for electron injection. While tunneling is temperature independent, the device current is slightly dependent on temperature. Another mechanism for charge injection is thermionic emission, in which emission current (J_e) is related to temperature through the Richard-Dushman equation [47]:

$$J_e = \left[\frac{(kT)^2 m q}{2\pi^2 \hbar^3} \right] e^{-\Phi/kT} \quad (2.2)$$

where J_e is the electronic charge flux, m is the mass of an electron, k is Boltzmann's constant, \hbar is Planck's constant (h) divided by 2π , Φ is the work function and T is temperature. This equation is valid for a metal-vacuum interface and must be modified to

take the phosphor's electron affinity into account. The injection current in ACTFELs is the primary result of field emission current with a slightly reduced barrier due to thermal effects.

2.4.2 High Field Transport

After electrons are injected into the conduction band, they must be accelerated to sufficiently high energies to induce luminescence by impact excitation. The mechanism by which this occurs has been disputed. A number of Monte Carlo simulations have been reported on high-field electron transport in ACTFELDs. Brennan used a full-band ZnS structure to calculate the electron energy distribution for fields up to 1 MV/cm. He concluded that few electrons obtained sufficient energy to excite Mn luminescent centers at these field strengths [48]. Another study utilized a simple-parabolic model, representing the conduction band for ZnS as a single parabolic band. In this model it was assumed that electron scattering was dominated by polar optical phonon scattering. The results suggested that electrons in ZnS experienced nearly loss-free high-field transport, resulting in a highly energetic electron energy distribution [49]. Bhattacharyya *et al.* [50] utilized a model incorporating a nonparabolic conduction band and included scattering from polar optical phonons, acoustic phonons, intervalley scattering, and ionized and neutral impurities. This showed significant loss at high-field transport but a stable energy distribution was calculated. Bhattacharyya *et al.* determined that nonpolar interactions and conduction-band nonparabolicity increased the electron-phonon scattering rates resulting in the stable electron distribution. Figure 2.3 shows the electron energy distribution ($n(E)$) as a function of electron energy for different phosphor fields using a full-band model, as well as the Mn^{2+} impact ionization cross-section as a function of

electron energy. These data show that a significant fraction of the electrons in ZnS attain energies around 2.12 eV which is the minimum energy needed to excite Mn^{2+} .

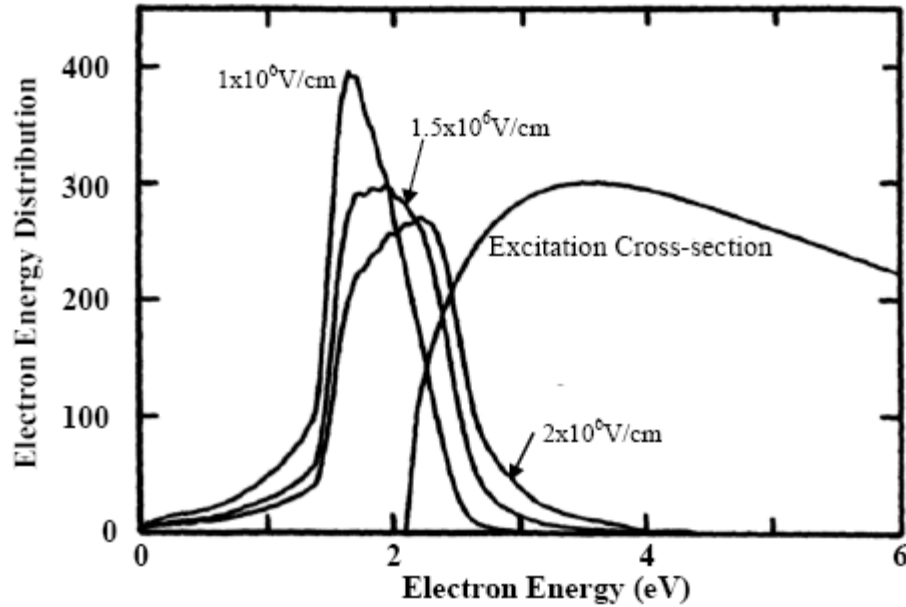


Figure 2.3 Electron energy distribution in ZnS as a function of energy for different phosphor fields using a full-band structure model [50].

Another approach to modeling high-field transport is the lucky-drift approach.

Bringuier argued that full-band Monte Carlo may be a more accurate approach, however, due to uncertainty in the physical parameters of II-VI compounds and low crystallinity in ACTFELs, the lucky-drift approach may be adequate to predict device operation [51].

Baraff developed the theory behind the lucky-drift approach which assumes two transport modes: one which is ballistic and collision-free, and another in which the electron undergoes one collision, increasing its probability of subsequent collisions [52].

2.4.3 Impact Excitation

Under the presence of a large applied electric field, some portion of the electrons will encounter luminescent centers. Sufficiently “hot” or high energy electrons will cause either impact excitation or impact ionization of these centers. Hot electrons may also

interact with the host matrix or non-luminescent centers in the host matrix. Such interactions with the host can produce electron-hole pairs which may also act as charge carriers under the applied field.

The probability of electrons interacting with the luminescent centers is related to the luminescent center radiative excitation cross-section. Impact excitation occurs when an electron in the ground state of the luminescent center is excited to a higher electronic state localized on the activator ion core. The pathway that the electron uses to return to the ground state may be either radiative or non-radiative. Radiative pathways produce a photon whose wavelength corresponds to the energy difference between the excited and the lower energy state to which the electron relaxes. Non-radiative pathways produce phonons, converting the potential energy to heat without luminescence. The delay time between excitation and relaxation may be long, e.g. milliseconds, or short, e.g. fractions of a microsecond. This delay depends on the spin and parity selection rules applied to the excited and lower energy electronic states [53].

The hot electron may also ionize the ground state electron of the luminescent center by impact scattering the electron into the phosphor conduction band. After impact ionization, the activator ion core may trap either an electron or hole and capture an opposite charge carrier to produce an electron-hole recombination with subsequent light emission. Under these high fields, electrons are accelerated to such high energies that there is a significant reduction in the cross-section of capture. The residence time of trapped carriers may also be so short that recombination is unlikely, as carriers may be easily stripped away from luminescent centers due to the high field [54]. Additionally the electrons produced by electron-host interactions, as well as those produce from impact

ionization, will undergo electron multiplication at high fields. This occurs when one electron elastically scatters off of a valence electron creating an additional conduction band electron and a valence band hole. These electrons may also be accelerated and scattered, creating more electrons and holes in a similar fashion. This is known as avalanche breakdown. The data indicate that impact excitation acts as the primary mechanism for luminescence in ZnS:Mn ACTFEL devices [45, 55].

2.4.4 Radiative Decay

With electrons in an excited state, luminescent centers may reduce their energy by emitting a photon, non-radiative relaxation (typically by phonon emission) or energy transfer to another ion. As discussed above, radiative relaxation produces photons with energy matching the difference between the excited state energy and the energy state to which the electron relaxed. The emitted photon has a wavelength corresponding to this energy difference [54]. Phonons produced through non-radiative relaxation have much smaller energies, typically around 20 meV, than any photons produced [56]. Because of interest in the production of photons, non-radiative relaxation should be minimized. Thus, the desired excited state must be one from which a photon is most likely to be produced.

2.4.5 Optical Outcoupling

Because ACTFELDs are designed to produce light, an important factor is the direction that light must escape the device. Light produced in the phosphor layer of the ACTFEL devices will see several interfaces before it exits, as is shown in Figure 2.4. Typically, the phosphor layer has the highest index of refraction of all the layers in the device and all layers have an index of refraction higher than air. As light travels from the phosphor layers through the insulators, a critical angle for internal reflection (θ_c) can be defined as:

$$\theta_c = \sin^{-1} (n_2/n_1) \quad (2.3)$$

where n_1 and n_2 are the refractive indices of the media the light is traveling in and striking, respectively [12]. The refractive index for ZnS:Mn is 2.3, while the surrounding insulating layers have smaller indices, Al_2O_3 for example has an index of 1.63, and air has a refractive index of 1.0. As a result, most of the light generated is trapped within the device because of internal reflection. To estimate the optical outcoupling efficiency (η_{opt}), the amount of light produced that leaves the device, we can simplify the system by only taking the largest refractive index (ZnS) into account. The value of η_{opt} can be defined as:

$$\eta_{\text{opt}} = \int \sin \theta \, d\theta \text{ from } 0 \rightarrow \arcsin (n_2/n_1) \quad (2.4)$$

As such $\eta_{\text{opt}} = 1 - [1 - (1/2.3)^2]^{0.5} \sim 0.1$. The optical outcoupling efficiency can be improved by more than an order of magnitude by increasing the surface roughness, thus reducing internal reflection [57]. However a surface that is too rough will reduce contrast by increasing diffuse scattering [12] and may lead to electrical breakdown at high fields.

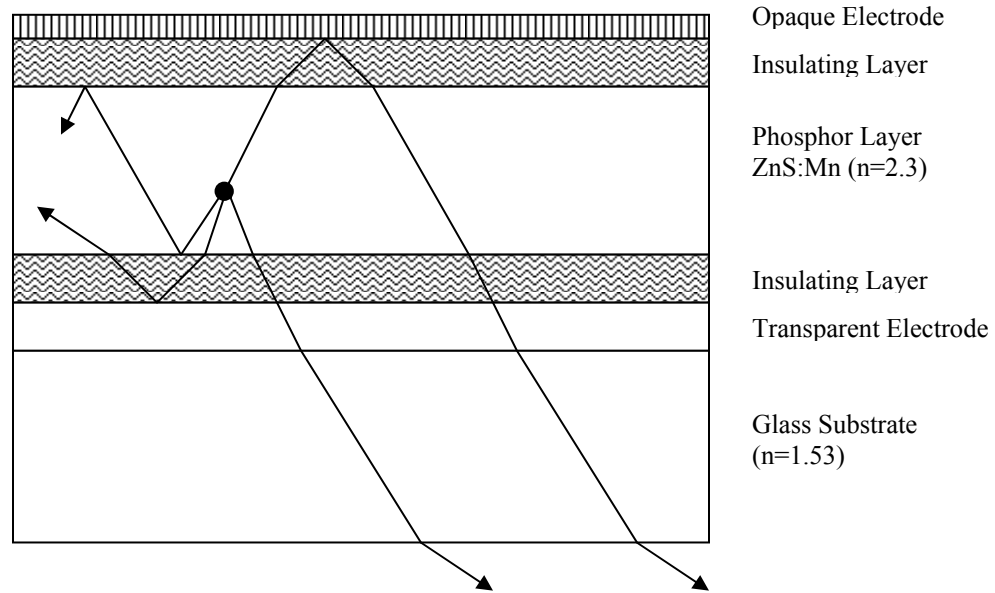


Figure 2.4 Schematic illustration for internal reflection in ZnS:Mn ACTFEL device [12].

2.5 ACTFELD Materials

2.5.1 Substrate Materials

The substrate chosen for ACTFELDs has a number of requirements [12]. It must be readily available and relatively cheap. It should have a high transmission coefficient for the wavelength region of interest, and have a coefficient of thermal expansion close to that of the deposited films. Additionally, the substrate should have a low alkali metal content to prevent diffusion of metal ions into the phosphor layer, as they will deteriorate device performance. The most common substrate used for visible ACTFELDs is Corning 7059 barium borosilicate glass used frequently for LCD substrates [58]. It has a softening temperature of approximately 598°C allowing it to endure rapid thermal annealing up to 650°C without significant damage or warping [59]. For smaller samples, anneals may reach temperatures up to 850°C for short durations without appreciable damage. The transmission spectrum for Corning 7059 glass is shown in Figure 2.5.

Applications requiring higher temperature anneals or transmission in the mid-infrared require a different substrate, e.g. silicon. With proper doping, this substrate may function as the bottom electrode in an inverted structure, as shown in Figure 2.1 (b). Silicon substrates can withstand annealing temperatures up to 1400°C, shifting the limit for higher temperature processing to the deposited layers. In addition, silicon can have high transmission coefficients in the NIR and well into the mid-infrared making it a good choice for IR emission from either the standard or inverted structure.

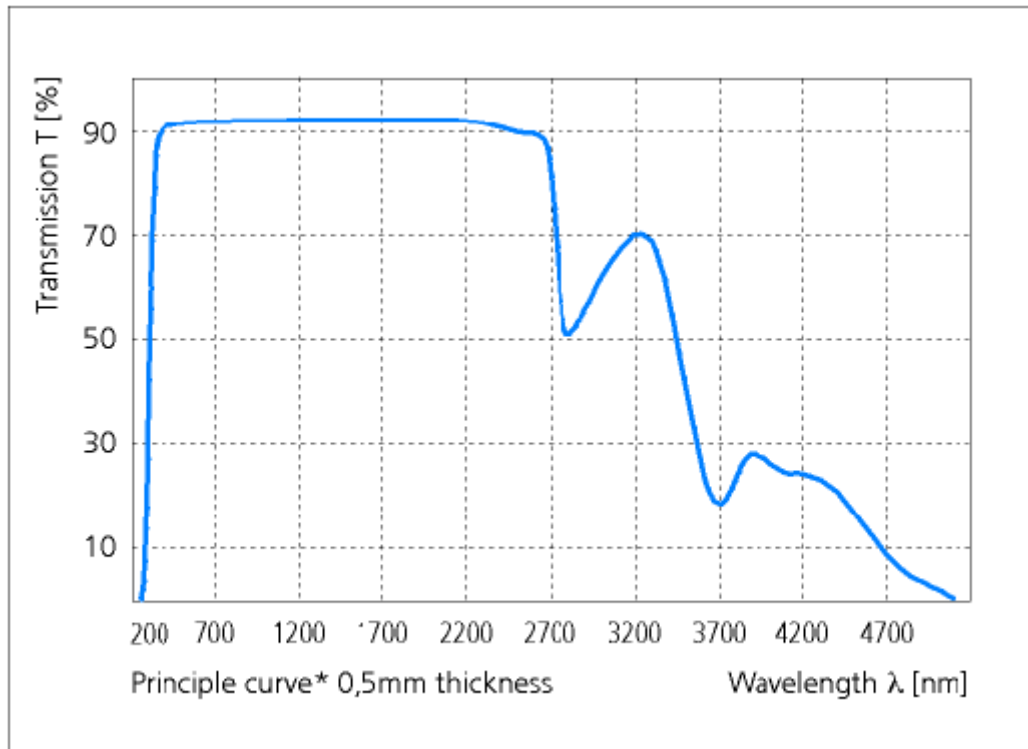


Figure 2.5 Transmission spectrum for Corning 7059 glass [60].

2.5.2 Insulating Materials

In both the standard MISIM and “half stack” devices, the phosphor layer is deposited directly onto a dielectric layer. As previously discussed, the insulator-phosphor interface states provide charge carriers for luminescence. However, the primary function for these layers is to protect the phosphor layer from runaway avalanche breakdown which leads to destruction of the phosphor at high fields, typically $>2\text{MV/cm}$. The properties of these insulating layers are thus of paramount importance. Requirements for dielectric layers are listed in Table 2.2.

Table 2.2 Requirements for dielectric layers

1. High dielectric constant.
2. High dielectric breakdown electric field strength.
3. Must provide interface states at the phosphor-insulator interface, from which electrons can tunnel into the phosphor conduction band.
4. A limited number of defects and pinholes. Defects and pinholes act as sites for local field enhancement and premature dielectric breakdown.
5. Good mechanical adhesion to both phosphor and conductive layers.
6. Good thermal and chemical stability over the processing temperature range (i.e. up to 650°C)
7. Transparency for the chosen emission region.

[12, 61-66]

For the device to operate most efficiently, the majority of the applied voltage must be dropped across the phosphor layer. The proportion of the voltage dropped across the phosphor versus insulating layers is determined by the capacitance of the phosphor, C_p , and the capacitance of the insulators, C_i . The capacitance of a layer is equal to:

$$C = (\epsilon_0 \epsilon_r) / t \quad (2.5)$$

where ϵ_0 is the permittivity of free space, ϵ_r is the relative permittivity and t is the layer thickness [67].

To maximize the voltage drop across the phosphor, the capacitance of the insulator should be much larger than that of the phosphor. Using Equation 2.5 leads to two possible results, either the insulating layer should be very thin compared to the phosphor or the relative dielectric constant should be large. The thickness of insulators is limited however, since those with <50 nm have shown charge leakage [68]. A high dielectric breakdown strength is necessary in the insulating layers because in the event that the phosphor becomes a virtual short the additional voltage will be dropped across the insulator increasing the electric field they experience. Unfortunately most insulators with high dielectric constants have low dielectric breakdown strengths [12]. Insulators with high dielectric constants will also exhibit propagation breakdown. Propagation

breakdown occurs when a portion of the insulator breaks down, forming a short that will heat up and cause catastrophic failure. Insulators with lower dielectric constants can exhibit self-healing where the breakdown area becomes an open rather than a short circuit.

Because a high dielectric constant and high dielectric breakdown strength are difficult to satisfy simultaneously, Howard developed a figure of merit to rate insulators for ACTFEL applications [65]. This is the product of the dielectric constant and the electrical breakdown field (E_{DB}) and is a measure of the maximum trapped charge density ($\mu\text{C}/\text{cm}^2$) at the insulator-phosphor interface. Table 2.3 shows a comparison of important properties for different insulators.

Table 2.3 Insulators used for ACTFEL devices and their properties

Insulator	Deposition Method*	ϵ_r	F_{BD} (MV/cm)	$\epsilon_o\epsilon_r F_{BD}$ ($\mu\text{C}/\text{cm}^2$)	Breakdown Mode**
SiO ₂	Sputtering	4	6	2	SHB
SiOxNy	Sputtering	6	7	4	SHB
SiOxNy	PVCD	6	7	4	SHB
Si ₃ N ₄	Sputtering	8	8 to 9	4 to 6	SHB
Al ₂ O ₃	Sputtering	8	5	3.5	SHB
Al ₂ O ₃	ALE	8	8	6	SHB
SiAlON	Sputtering	8	8 to 9	4 to 6	SHB
Y ₂ O ₃	Sputtering	12	3 to 5	3 to 5	SHB
Y ₂ O ₃	EBE	12	3 to 5	3 to 5	SHB
BaTiO ₃	Sputtering	14	3.3	4	SHB
SmO ₃	EBE	15	2 to 4	3 to 5	SHB
HfO ₂	Sputtering	16	0.17 to 4	0.3 to 6	SHB
Ta ₂ O ₅ -TiO ₂	ALE	20	7	12	SHB
BaTa ₂ O ₆	Sputtering	22	3.5	7	SHB
Ta ₂ O ₅	Sputtering	23-25	1.5 to 3	3 to 7	SHB
PbNb ₂ O ₆	Sputtering	41	1.5	5	SHB
TiO ₂	ALE	60	0.2	1	PB
Sr(Zr,Ti)O ₃	Sputtering	100	3	26	PB
SrTiO ₃	Sputtering	140	1.5 to 2	19 to 25	PB
PbTiO ₃	Sputtering	150	0.5	7	PB
BaTiO ₃ ****	Press/sinter	5000	?	?	?
Westaim proprietary***	Press/sinter	1700	?	?	?

2.5.3 Transparent Conductors

In the standard device structure, the first layer deposited onto the substrate is a transparent conducting layer. This layer must be sufficiently conductive so as not to affect the RC time constant of the device, must be transparent in the region in which emission will occur, and must withstand all thermal processing that the subsequent layers may need. The material most often chosen for this task is indium-tin-oxide (ITO) [12]. This is an alloy typically consisting of 90 wt% In_2O_3 with 5-10 wt% SnO_2 . ITO is optically transparent (>90%) over the visible region and NIR, and can be deposited by any number of deposition techniques, including pulsed-laser deposition, electron beam evaporation, DC magnetron sputtering, RF magnetron sputtering, plasma ion-assisted deposition, chemical vapor deposition and atomic layer deposition [12, 69-78]. The ITO layer used for ACTFEL devices is typically 200 nm thick with a resistivity of $\sim 1 \times 10^{-4} \Omega\text{-cm}$, providing a sheet resistance of $\sim 5 \Omega/\square$.

Indium-tin-oxide is a degenerately doped n-type semiconductor. The n-type conductivity is due to thermal ionization of shallow donors which arise from substitution of Sn^{4+} on In^{3+} lattice sites, as well as oxygen vacancies [79]. Thus the conductivity of ITO may be reduced if it is not suitably protected during annealing. Additionally ITO is not transparent at wavelengths greater than its plasma wavelength ($\sim 1.6\text{-}2 \mu\text{m}$) [79]. As such ITO is useful only for near infrared emitting ACTFELDs. At longer wavelengths a more suitable replacement may be the use of appropriately doped silicon substrates which may double as bottom electrodes in an inverted structure.

2.5.4 Opaque Electrode

In the standard device structure the top opaque electrode is the last layer deposited and like the bottom transparent electrode must be highly conductive. However the top

electrode does not have to meet other thermal processing requirements because any high temperature processing may be done prior to deposition of this layer. This layer must adhere well to either the top insulating layer in the case of a “normal” full stack device or to the phosphor layer itself, in the case of the “half stack” device. It must also be resistant to electromigration (metal-ion migration) [12], and be able to prevent some breakdown spread when dielectric breakdown of the insulating layer occurs, as discussed earlier.

Aluminum is easily deposited either by thermal evaporation or sputtering. It also serves as one of the most common bottom electrodes in the inverted structure but is limited due to its low melting temperature (660°C) for devices requiring high temperature processing. Gold, molybdenum, tantalum and tungsten are also well suited for bottom electrodes in inverted structures.

2.5.5 Phosphor Materials

2.5.5.1 Host materials

Phosphor systems consist of a host material and a luminescent center. In the case of high-field electroluminescence, we must identify the specific characteristics the host should possess. The host material should have a bandgap large enough that light generated during device operation is not absorbed. For near infrared emission the host bandgap must be at least 1.6 eV and for visible emission the bandgap must be at least 3.1 eV. The host material must also be non-conducting below the luminescence threshold, such that the host will be act as a capacitor at sub-threshold voltages. It should also have a high dielectric breakdown strength to allow electrons to reach appropriate energies to induce luminescence. The breakdown field of the host must be at least 1 MV/cm. The host material should have good crystallinity at appropriate doping levels, ~1 at%, and a low phonon-coupling constant to minimize electron scattering. Finally, the host must

have a substitutional lattice position of appropriate symmetry to incorporate the luminescent center.

Sulfur-based compounds have historically been used for these requirements. Among the possible choices are sulfides (e.g. ZnS, SrS and CaS) and thiogallates (e.g. CaGa_2S_4 , SrGa_2S_4 and BaGa_2S_4) [1, 2, 5, 14]. Table 2.4 lists the physical and electrical properties of the sulfide II-VI host materials. Among these, ZnS has a dielectric breakdown strength of ~ 1.5 MV/cm, making it sufficient to act as a capacitor at low fields and a conductor at high fields [80]. It also has a bandgap of 3.6 eV making it transparent from 400 nm to 10 μm [81]. These properties allow ZnS to serve as an appropriate host material choice for near infrared electroluminescent devices.

Table 2.4 Properties of some II-VI ACTFEL host materials

Property	IIb-VIb compound	IIa-VIb compound	
Compound	ZnS	CaS	SrS
Melting Pt. ($^{\circ}\text{C}$)	180-1900	2400	>2000
Band Gap (eV)	3.6	4.4	4.3
Transition Type	Direct	Indirect	Indirect
Crystal Structure*	ZB,W	Rock salt	Rock salt
Lattice constant (\AA)	5.409	5.697	6.019
Dielectric const.	8.3	9.3	9.4
Ionicity	0.623	>0.785	>0.785

*ZB = zinc blende; W = wurtzite; Orth. = orthorhombic

[12]

2.5.5.2 Luminescent centers

The luminescent center incorporated into the host material determines the emission wavelength of a phosphor. One type of radiative relaxation that occurs in traditional CRTs and many lamps results from the recombination of electrons trapped in deep donor levels and holes trapped in deep acceptor levels. In this case the phosphor host, typically

ZnS, will be doped with combinations of Ag, Cu, Au, Al acting as acceptors and Cl acting as a donor, to tailor the optical emission to the desired wavelength. This type of luminescent center can not be used in ACTFEL devices because the high electric fields used in the devices sweep electrons and holes to opposite sides of the device, quenching any luminescence [12, 13].

Another kind of radiative relaxation occurs in luminescent centers, in which a localized transition occurs between different electronic states of the isolated luminescent center (dopant). The emission that results depends on the excited energy state and the lower energy state to which the electron relaxes. In this system quantum mechanical selection rules for electronic transitions become important to understanding emission. The parity selection rule forbids transitions between energy levels of the same parity [54]. For example, transitions between the f and d shells or between the p and s shells are allowed. However transitions within a particular shell or between the f and p or d and s are forbidden. The spin selection rule forbids transitions between configurations with different spin states [54].

Transition metal ions, like Ti^{4+} , Cr^{2+} , Mn^{2+} , Cu^+ and Ag^+ , are common luminescent centers for ZnS [12]. All have a d^n valence configuration and emission spectra characteristic of intra-shell $d-d$ transitions. As such all of these transitions are forbidden by the parity selection rule. These ions tend to exhibit broad band emission, with decay lifetimes ranging from 100 microseconds to several milliseconds, depending on the spin selection rule and symmetry. Because these transitions originate in the valence shell, they are strongly influenced by the local crystal field of the host [12].

Rare earth or lanthanide ions, like Nd^{3+} , Eu^{3+} , Eu^{2+} , Tb^{3+} , Er^{3+} and Tm^{3+} , have also been used as luminescent centers for ZnS phosphors [12]. Lanthanide rare earth ions have an electron configuration of $1s^2 2s^2 2p^6 3s^2 3p^6 4s^2 3d^{10} 4p^6 5s^2 4d^{10} 5p^6 6s^2 4f^n$ with atomic orbitals filling up in order of increasing energy. As a result the $5s$, $5p$ and $6s$ orbitals all are filled before the $4f$ orbital. Because of this unique electron configuration, emission from rare earth ions typically originates in $4f$ - $4f$ transitions that are shielded from the environment by the outer $5s$, $5p$ and $6s$ electrons. Figure 2.6 shows a schematic representation of the shielding of the $4f$ electrons.

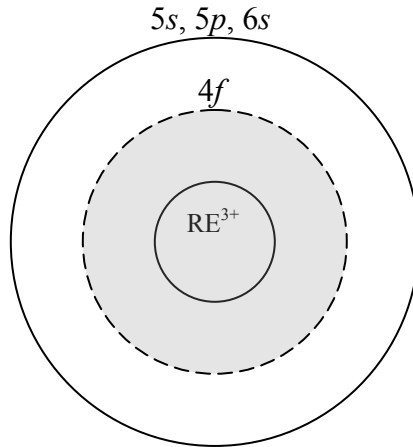


Figure 2.6 Schematic illustration of shielding of inner $4f$ orbital of a rare earth ion by the outer $5s$, $5p$, and $6s$ shells.

For certain ions, notably Ce^{3+} and Eu^{2+} , excitation into the empty outer $5d$ shell may also occur. In these cases, the parity rule is not broken, however the Eu^{2+} transition is spin forbidden. Decay times for Ce^{3+} are faster than Eu^{2+} by several orders of magnitude [54]. These $5d$ - $4f$ transitions are strongly affected by the crystal field and can shift in wavelength dependent on the host material. More typical are the transitions of rare earth ions like Tm^{3+} , Nd^{3+} and Er^{3+} , which involve $4f$ - $4f$ transitions. Because these transitions are parity forbidden they have longer decay times. Figure 2.7 shows partial

energy level diagrams for Tm^{3+} which emits in the blue, Er^{3+} which emits in the green and Nd^{3+} which emits in the orange. These ions show several emission lines in the infrared and when incorporated into ACTFEL devices could be used in a number of applications, for example telecommunications, phototherapy and sensing equipment.

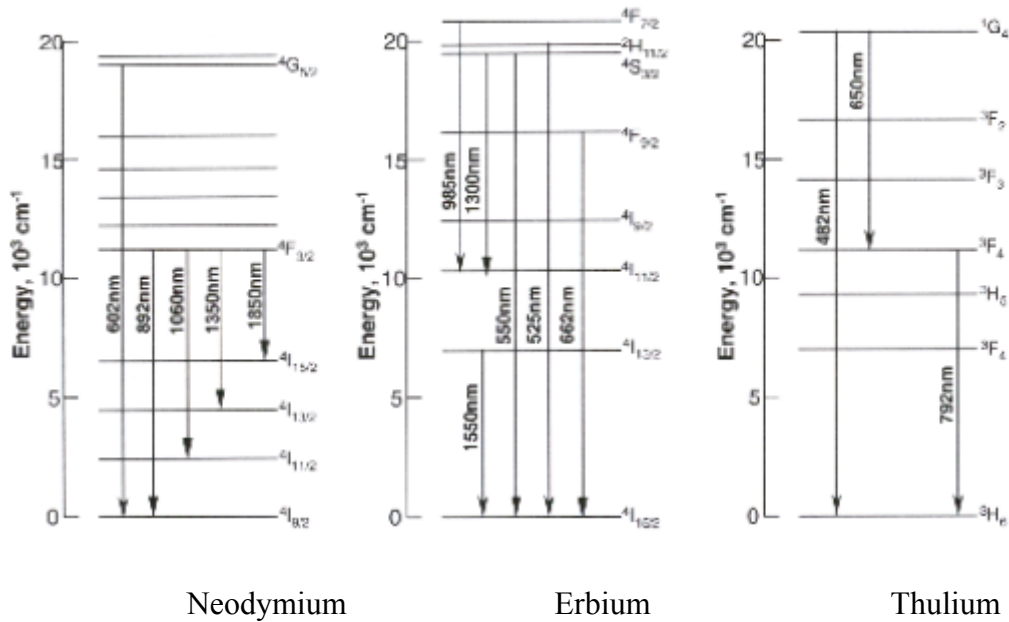


Figure 2.7 Partial energy level diagrams for Neodymium, Erbium and Thulium in ZnS [82, 83].

To create full-color displays utilizing ACTFEL devices, a number of different combinations of host material and luminescent center have been developed. Table 2.5 shows a comparison of several ACTFEL phosphors and their visible emission characteristics. The phosphor most commonly used for ACTFEL is ZnS:Mn which possesses a yellow emission. It may also be filtered to produce both red and yellow-green. However ZnS systems used to create blue emission have substantially lower luminance and are unsuitable for applications. Strontium sulfide doped with cerium is the most widely used blue emitter for full-color displays [14].

Luminescent centers sit on substitutional sites in the host lattice, therefore the charge difference between the dopant ion and displaced host ion must be compensated to maintain charge neutrality. The most common charge compensators are interstitial halide ions, typically F^- and Cl^- . These balance the $3+$ charge that occurs when a rare earth substitutes for the Zn^{2+} ions in the host. The effect of charge compensating halides on luminescence has been investigated under a number of different circumstances. Oberacker and Schock studied the effects of choice of halide, specifically fluorine and chlorine, on the SrS:Ce ACTFEL emission. They showed no appreciable influence on blue electroluminescence when samples were co-doped with LiCl. However samples co-doped with LiF showed a distinct shift to lower energies, namely green. This was attributed to the nephelauxetic effect [84].

Lithium co-doping has also been investigated in ZnS:TmF₃. In this case, the luminescent center is isolated from the surrounding crystal field, unlike cerium. The infrared emission from the device increased relative to the visible emission peaks. This was attributed to a change in oscillator strength, resulting from lower symmetry around the Tm³⁺ ion [85].

Co-doping with lithium is not the only method to control changes in electroluminescent emission from rare earth doped zinc sulfide. Post-deposition annealing has been shown to affect the concentration of fluorine, with F concentration in ZnS:TbF₃ decreased by annealing temperatures over 300°C. Since the Tb concentration was unaffected by annealing, the ratio of fluorine-to-terbium (F/Tb) decreased from 3/1 in the as-deposited condition to 1/1 in films annealed at 550°C. This corresponded to a four-fold increase in green emission [86].

Table 2.5 Comparison of visible emission from ACTFEL phosphors

Phosphor Material	Emission Color	CIE Coordinates	Subpixel Luminance at 60 Hz (cd/m ²)	Luminous Efficiency (lm/W)
ZnS:Mn	Yellow	x=0.5, y=0.5	600	5
ZnS:Mn/filter	Red	x=0.65, y=0.35	75	0.8
ZnS:Mn/filter	Yellow-green	x=0.45, y=0.55	80	
ZnS:TbOF				
ZnS: Tb, F	Green	x=0.30, y=0.60	125	1.3
	Green	x=0.30, y=0.60	90	0.5-1
ZnS: Sm, Cl				
ZnS: Sm, F	Red	x=0.64, y=0.35	12	0.08
	Orange-red	x=0.60, y=0.38	8	0.05
ZnS: Tm, F				
	Blue	x=0.15, y=0.15	<1	<0.01
ZnS:Mn/ SrS:Ce	White	x=0.42, y=0.48	450	1.6
SrS: Ce, Eu	White	x=0.41, y=0.39	36	0.2
CaS: Eu	Red	x=0.68, y=0.31	12	0.05
CaS: Ce	Green	x=0.27, y=0.52	10	0.1
CaGa ₂ S ₄ : Ce	Blue	x=0.15, y=0.19	13	0.04

[14]

2.5.6 ZnS:ErF₃ as an ACTFEL Phosphor

Rare earth doped zinc sulfide may be deposited by a number of different methods. These include chemical vapor deposition (CVD), metal oxide chemical vapor deposition (MOCVD) and thermal evaporation [87-89]. At room temperature, zinc sulfide may exist in either the cubic zincblende structure called sphalerite and the hexagonal, wurtzite structure. The properties of these phases are listed in Table 2.6.

Table 2.6 Properties of different zinc sulfide phases.

Parameter	Value	
	Zincblende	Wurtzite
Lattice Constant (Å)	5.409	a=3.814; c=6.258
Mass Density (g/cm ³)	4.08	4.1
Melting Point (K)	2100	2100
Heat of Formation (kJ/mol(300K))	477	-206
Specific Heat (J/kg-K(300K))	472	
Debye Temperature (K)	530	

[90]

Erbium is one of the rare earth ions most known for infrared emission.

Telecommunications utilizes the 1550 nm infrared emission produced by erbium for use in fiber optic cables because the fibers have an absorption minimum at this same wavelength [91]. As mentioned in Section 2.5.5.2, the transitions of erbium are parity forbidden $4f$ intrashell transitions. As such, the surrounding crystal field has little effect on the emission wavelength. ZnS:ErF₃ has green emissions at 525 nm ($^2H_{11/2} \rightarrow ^4I_{15/2}$) and 548 nm ($^4S_{3/2} \rightarrow ^4I_{15/2}$), red emission at 662 nm ($^4F_{9/2} \rightarrow ^4I_{15/2}$) and near infrared emissions at 985 nm ($^2F_{7/2} \rightarrow ^4I_{11/2}$) as shown in Figure 2.8. The 1550 nm emission is not shown. Some studies have indicated that the luminescence intensity from erbium at room temperature is strongly influenced by the semiconductor host bandgap. Semiconductors with larger bandgaps exhibited less temperature quenching of erbium luminescence [92]. As such, a number of research efforts have reported on erbium doping of wide bandgap semiconductors [92-96]. The ratio of visible-to-infrared emission intensities has been reported to depend on both the host material and erbium concentration [97].

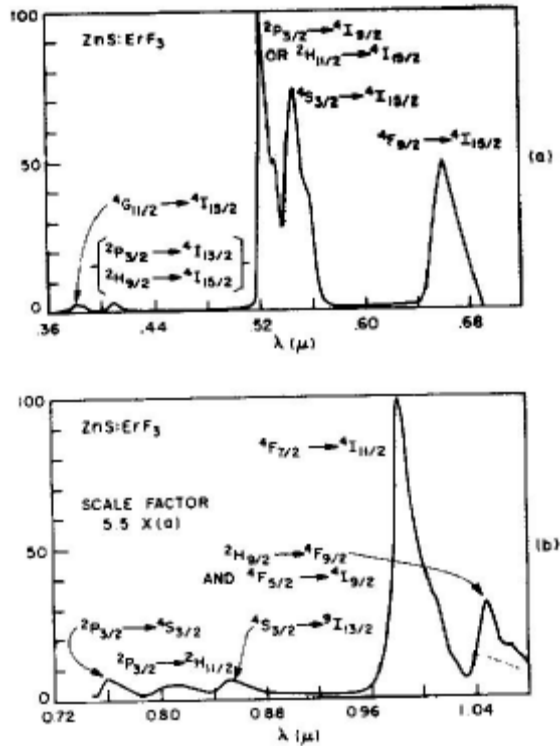


Figure 2.8 Emission peaks from ZnS:ErF₃ [98].

Kale *et al.* [99] have shown that annealing of ZnS:ErF₃ films results in enhancement of the infrared luminescence from ACTFEL devices. Increased infrared and decreased visible emission were reported for annealing temperatures up to 425°C for 1 hour in a nitrogen atmosphere. This was attributed to defect removal from the film upon annealing, allowing acceleration of ballistic electrons to higher energies. Studies by Keir *et al.* [33] compared ZnS and SrS as host materials for ACTFEL. Their research showed that SrS was a better high-field electron transport material than ZnS, allowing creation of a “hotter” electron distribution. As a result ZnS may be a better choice for infrared emission applications because of better excitation of the longer wavelength, low energy, transitions.

2.6 ACTFELD Characterization

2.6.1 Optical Characterization

Two different units are typically used to quantify optical output, radiometric units used to quantify electromagnetic radiation and photometric units used to quantify optical output for systems with visible emission. Radiometry quantifies the photon flux density, or irradiance, measured in $\text{W}/\text{cm}^2\cdot\text{nm}$. In the photometric system, the spectral response of the human eye is taken into account. As such two wavelength emissions with the same radiometric output may have very different photometric values based on human perception.

Among the most common measurements of optical output from ACTFEL devices is the measurement of EL light intensity as a function of applied voltage. This is typically referred to as a Brightness versus Voltage, or B-V, data. These measurements involve the use of a variable AC voltage source, commonly using a trapezoidal pulse and frequencies of either 60 Hz or 2.5 kHz. This is used along with a suitable spectrometer to collect the brightness data. A typical B-V curve is shown in Figure 2.9. This figure shows that the onset of emission occurs when the voltage reaches a critical value, known as the luminescence threshold voltage (V_{th}), determined by extrapolation of the maximum slope to the intercept with the voltage axis. At this value, the electric field is capable of accelerating electrons to energies which excite luminescent centers and result in light emission.

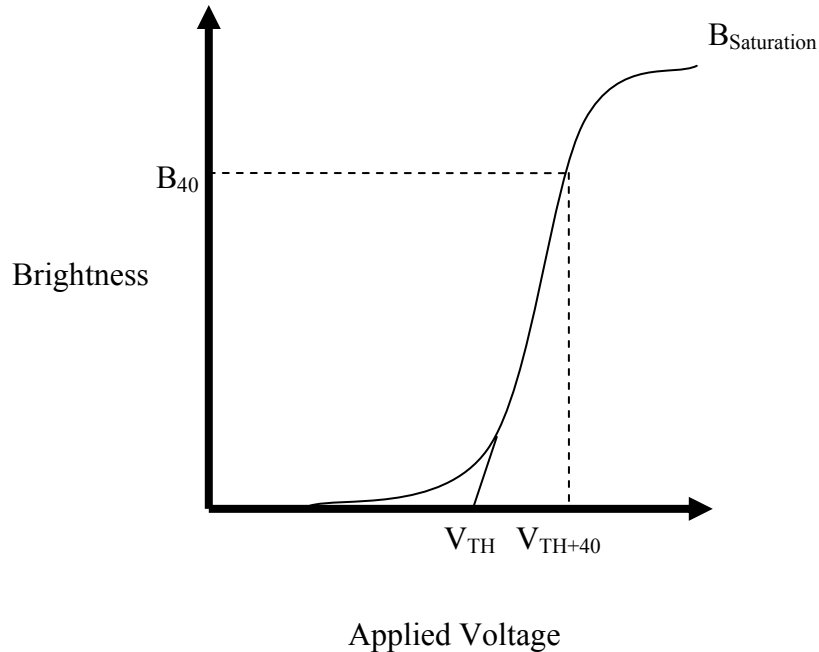


Figure 2.9 Typical Brightness versus Voltage for ACTFELD

Above the threshold value, brightness increases linearly with increasing field until the device saturates or the phosphor undergoes catastrophic dielectric breakdown. Any voltage above threshold may be used to compare samples (i.e. B_x), however B_{20} and B_{40} are most common. The brightness at 40 V above threshold is often used as a characteristic value because ACTFELDs are commonly modulated over this voltage range. In order to use B_{40} for comparisons, the phosphor layers should have nearly identical thicknesses and be driven at the same frequency. Thicker phosphor films may contain a higher number of luminescent centers, resulting in a greater number of light emitting events over the same amount of time. To compare brightness taken at different frequencies or with different thicknesses, it is frequently assumed that brightness depends linearly on the phosphor thickness and voltage frequency.

2.6.2 Electrical Characterization

2.6.2.1 Equivalent circuit models of ACTFELDs

ACTFEL devices consist of a phosphor layer sandwiched between two insulating layers. The ideal electrical behavior of this system, shown in Figure 2.10 (a), can be modeled as a capacitor in parallel with a non-linear resistor. Another model for this device has the two insulating layers as perfect capacitors and the phosphor layer as a capacitor shunted by two back-to-back Zener diodes, as shown in Figure 2.10 (b).

For the model in Figure 2.10 (a), the applied voltage, (V_a), is the voltage across the phosphor layer, (V_p), plus the voltage across the insulating layers, (V_i) and

$$V_a = V_p + V_i \quad (2.6)$$

Below the threshold voltage, the applied voltage is divided according the values of capacitance of the phosphor and insulators as follows:

$$V_p = [C_i / (C_i + C_p)] V_a \quad (2.7)$$

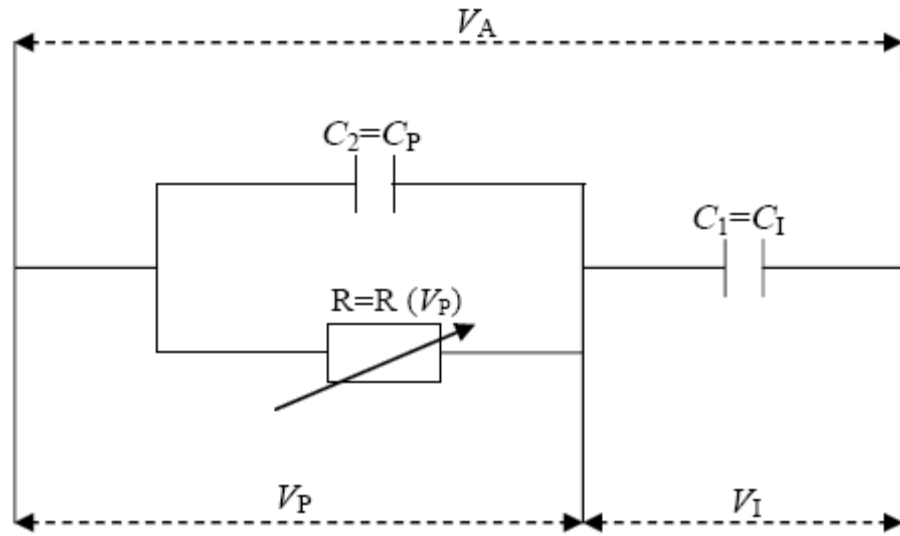
$$V_i = [C_p / (C_i + C_p)] V_a \quad (2.8)$$

where V_a is the applied voltage, V_i and V_p are the voltages across the insulators and the phosphor, respectively, and C_i and C_p are the capacitance of the insulators and phosphor, respectively.

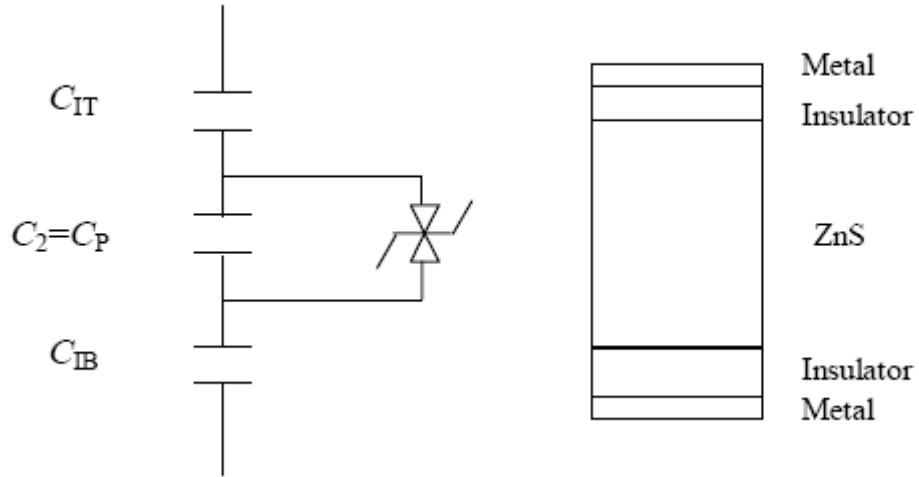
Above the threshold voltage, the resistive portion of the phosphor allows current to flow (called conduction current), until the voltage across the phosphor returns to the threshold value. The conduction current must be balanced by a capacitive current which will charge the insulating capacitors in order to maintain the overall voltage across the device. As a result the voltages for the phosphor and insulator are represented by the following:

$$V_{p,f} = V_{p, TH} = [C_i / (C_i + C_p)] V_{TH} \quad (2.9)$$

$$V_{i,f} = V_a - V_{p,f} = [C_p / (C_i + C_p)] V_{TH} \quad (2.10)$$



(a)



(b)

Figure 2.10 Equivalent circuit models for ACTFELDs modeled as (a) a capacitor in parallel with a non-linear resistor and (b) as two back-to-back Zener diodes [61].

The concept of field clamping follows from these equations, where the electric field across the phosphor layer is maintained at the threshold voltage divided by phosphor thickness regardless of the voltage applied to the device. A more detailed discussion of this model can be found in Ono [12] and Wager [19].

In the model in Figure 2.10 (b), both the top and bottom insulating layers are assumed to be perfect capacitors. Their total effective capacitance is:

$$C_i = C_{it}C_{ib} / (C_{it} + C_{ib}) \quad (2.11)$$

where C_{it} and C_{ib} are the capacitance of the top and bottom insulating layers, respectively. Below the threshold voltage, the phosphor layer acts as a capacitor. Above the threshold voltage, a dissipative current flows through the phosphor layer resulting in light emission. The device brightness is proportional to the power consumed by the resistive branch of the circuit [12].

2.6.2.2 Electrical characterization

The circuit typically used for electrical device testing is a Sawyer-Tower arrangement with either a sense capacitor or sense resistor as shown in Figure 2.11 [53]. A waveform generator is used to produce a voltage pulse that is amplified to drive the circuit. The circuit consists of a series resistor, ACTFEL device and a sense element in series. The series resistor is used to limit current to the ACTFEL device in the event of catastrophic failure. If the sense element is a capacitor the internal charge is measured; if a resistor is used as the sense element then external current is measured. When sensing charge, the sensing capacitance must be larger than that of the device. In cases where a resistor is used, the resistance should not be too large. The dynamic response of the circuit will be decreased as the RC time constant of the circuit increases.

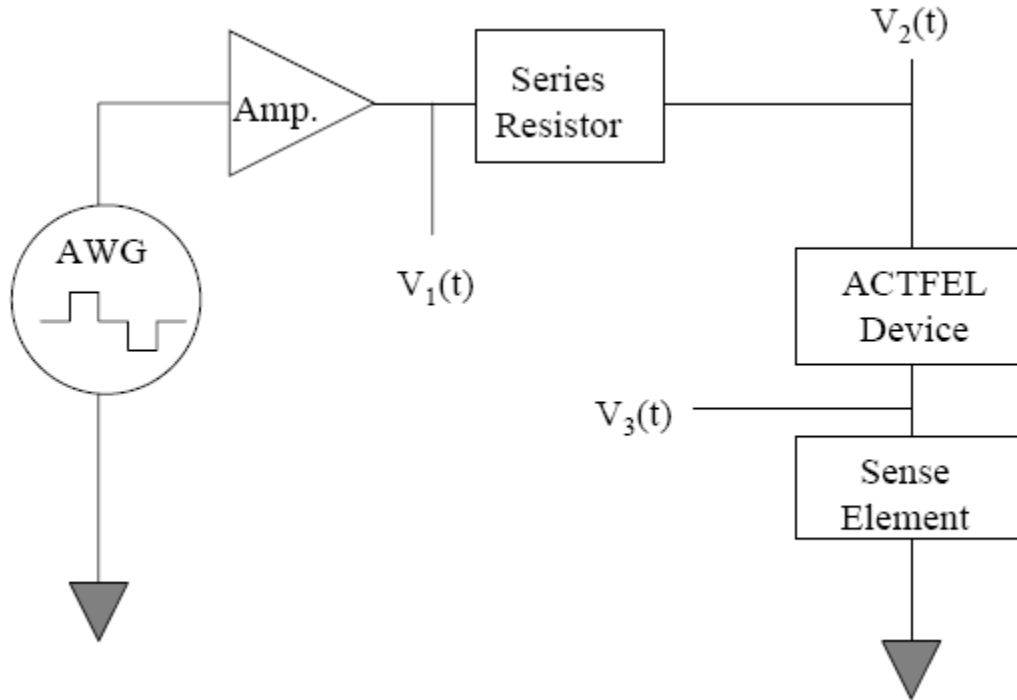


Figure 2.11 Schematic of a Sawyer-Tower bridge circuit [53].

The electrical characteristics of ACTFEL devices consist of charge versus voltage, or a Q-V plot. A Q-V plot shows the charge stored across the two external terminals of the capacitive ACTFEL devices versus the voltage applied across those terminals. As a device is driven below the threshold voltage, the plot is a straight line with a slope equal to the total capacitance of the device, assuming negligible leakage current. When the device is driven above the threshold voltage, the Q-V plot forms a hysteresis loop due to the conduction charge that flowed through the phosphor. Q-V plots allow a determination of the conduction threshold voltage of the device, which is shown in Figure 2.13 as V_{to} .

The voltage drop across the ACTFEL device is found from V_2 and V_3 in Figure 2.11 as follows:

$$V_{EL}(t) = V_2(t) - V_3(t) \quad (2.12)$$

When using a capacitor as the sense element, the external charge is determined by:

$$Q_{\text{ext}}(t) = C_s V_3(t) \quad (2.13)$$

where C_s is the sense element capacitance. When using a sense resistor, the current passing through the device is equal to:

$$i(t) = [V_1(t) - V_2(t)] / R_{\text{series}} \quad (2.14)$$

The resulting external charge is found by integrating this current over time, such that:

$$Q_{\text{ext}}(t) = \int i(t) dt \text{ from } 0 \rightarrow t \quad (2.15)$$

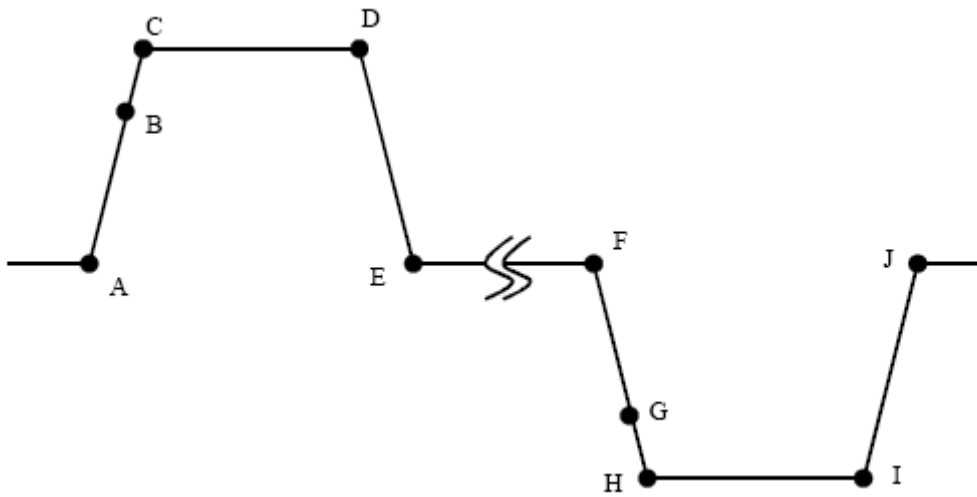


Figure 2.12 Diagram of the trapezoidal voltage waveform used in ACTFEL device operation and testing.

The typical waveform used for testing is a bipolar trapezoidal wave as shown in Figure 2.12. The pulses have a rise and fall time of $\sim 5 \mu\text{s}$, a $30 \mu\text{s}$ plateau and a frequency between 60 Hz and 2.5 kHz. The corresponding points (A-J) of Figure 2.12 are self-explanatory with the exception of points B and G. These correspond to the voltage values where the conduction charge becomes significant.

Figure 2.13 shows a typical Q-V plot using the labeling scheme from Figure 2.12. Conduction charge, discussed for the simplified models, can still be seen. Additionally one can see the relaxation charge and leakage charge. Relaxation charge occurs when the

applied voltage reaches a maximum value and reflects current which flows during the plateau of the voltage pulse (C-D in Figure 2.12). This nomenclature reflects the fact that, at constant applied voltage, the conduction charge creates an opposing electric field that relaxes across the phosphor. Voltage decreases linearly during the falling segment, D-E of Figure 2-12. After the voltage reaches zero between the pulses of opposite polarity, there is a leakage charge, Q_{leak} . This is typically assigned to electrons escaping from shallow interface states in the ACTFELD. Assuming device symmetry, the features of the Q-V hysteresis from F to J are equivalent to those from A to F, with the exception that

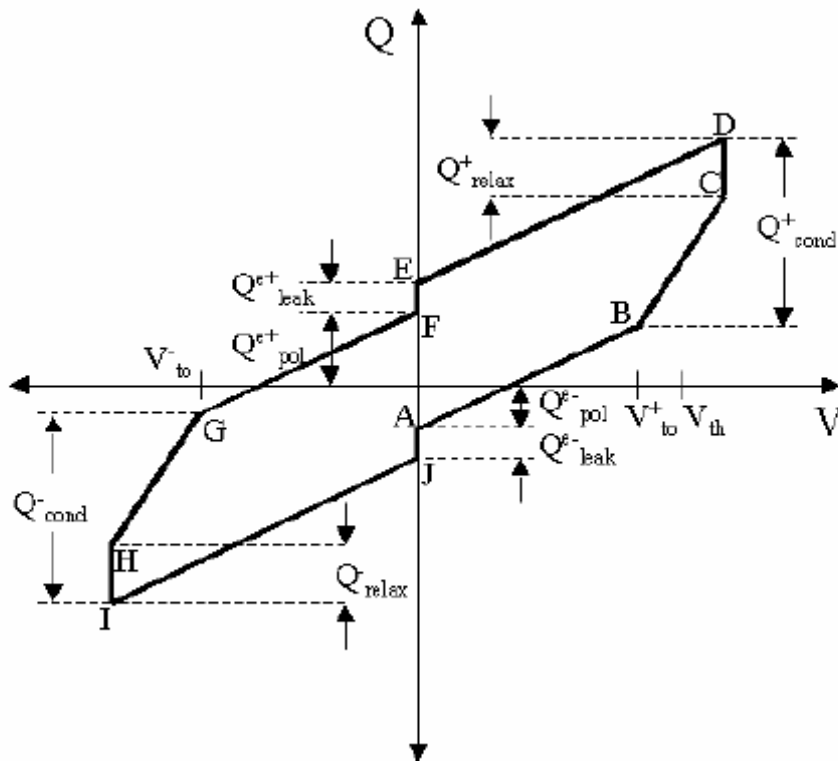


Figure 2.13 Schematic of Q-V plot for ACTFEL device. [V_{to} : electrical turn-on voltage, Q_{cond} : conduction charge, Q_{pol} : polarization charge, Q_{leak} : leakage charge, Q_{relax} : relaxation charge] Lettering refers to labels for voltage waveform in Figure 2.11.

the voltage pulse is of opposite polarity. Also, Q_{cond} , represents the conduction charge above the threshold voltage. This charge is responsible for light emission in ACTFELDs [50].

Q-V data can be used to determine a number of useful parameters about an ACTFEL device. First, the slope of the Q-V plot below the threshold voltage is equal to the total capacitance of the device. Second, above the threshold voltage the phosphor is considered a conductor and the slope of the Q-V plot is used to measure the capacitance of the insulating layers. If the device is not completely shorted, however, the slope will be greater than that of the insulating layers themselves as it will incorporate some residual component of the phosphor layer. Also if there is a build-up of space charge in the phosphor, the slope will be larger than the insulator capacitance [83]. Third, the area inside the Q-V plot is proportional to the input electrical power density delivered per pulse [100].

CHAPTER 3 EXPERIMENTAL PROCEDURE

3.1 ACTFEL Device Fabrication

3.1.1 Substrate Preparation

Substrates consist of Corning 7059 glass, 0.04 inches thick, coated with 360 nm of polycrystalline indium tin oxide (ITO) (90 wt% In_2O_3 + 10 wt% Sn_2O_3) as the transparent conducting electrode and 160 nm of amorphous aluminum titanium oxide (ATO) (Al_2O_3 / TiO_2) as the bottom insulating layer. These were supplied by Planar Systems. The ATO dielectric layer was deposited by atomic layer deposition (ALD) to ensure a high quality, homogeneous insulator. Each substrate is dusted using dry nitrogen gas to remove airborne particulate. Substrates are also cleaned in a UVOCS, Inc. ultraviolet light ozone cleaner for six minutes to remove organic contaminants. Additional substrates of bare Corning 7059 glass were prepared using the same method for use in thickness measurement.

3.1.2 Thin Film Deposition

ZnS:ErF_3 thin films were deposited onto the ATO/ITO/glass substrates by radio frequency (RF) planar magnetron sputtering to a layer thickness of $650 \text{ nm} \pm 15\%$. Two sputter targets were used for this study, an undoped ZnS and a ZnS doped with ErF_3 . The undoped ZnS target was grown by chemical vapor deposition (CVD) by Morton Thiokol and cut to appropriate thickness (1 mm) using a diamond saw. The doped ZnS target was powder pressed and doped with 1.5 mol% of 99.9% pure ErF_3 . This was manufactured by Target Materials Inc. All sputter targets are 2 inches in diameter and $\frac{1}{4}$ inch thick.

The sputter deposition system is designed to allow up to three R.F. magnetron sputter guns to be used simultaneously. An Angstrom Science Onyx 2 magnetron sputtering gun was used for the undoped target and an AJA A300 magnetron sputtering gun was used for the doped target. The target-to-substrate distance is 10 cm for the (undoped) Angstrom Science gun and 5 cm for the (doped) AJA gun. Power to each gun was provided by an RF Power Products RF5S radio frequency controller with an RF Power Products matching network. Duty cycles can be varied on both targets independently from 0% to 100%. By altering the duty cycle of the power applied to the target, the composition of dopant in the deposited film was changed. Applied power was set to 100 watts for both sources.

Substrates are held on a sample holder with capacity for four 2" x 2" substrates or eight 1" x 2" substrates. When placed in the deposition chamber, samples are rotated at 11 seconds per revolution using a constant speed stepping motor. Substrates are heated, up to 300°C by means of carbon fiber heating elements underneath the sample stage. A thermocouple is used to monitor chamber temperature. A schematic of the sputter deposition system is shown in Figure 3.1. Deposition rates varied depending on the duty cycle of the targets and the substrate temperature. As a result, deposition times were varied to maintain film thicknesses as close to 650 nm as possible.

Samples are introduced through a load lock which is pumped down to a pressure of 10 mTorr using a Leybold Trivac D65B wet rotary pump. The deposition chamber is pumped down by a Leybold Mag 1600 turbomolecular pump backed by the Leybold Trivac D65B wet rotary roughing pump. The ultimate pressure for the system varied between 6.1×10^{-7} and 1.2×10^{-6} Torr. Ultra high purity (99.9999%) argon was used as

the sputtering gas for this study. The gas was introduced into the chamber using Unit UFC 1100A 20, 50 or 100 sccm mass flow controllers on three inlet lines. Argon gas pressure was regulated using the flow controllers and a throttle valve installed between the deposition chamber and the turbomolecular pump. A number of gauges on the system allow monitoring of pressure in various regions of the system. Thermocouple gauges are used to monitor pressure in the fore line and load lock. An ionization gauge is used to measure pressure in the main chamber and a capacitance manometer monitors argon gas pressure in the chamber during deposition.

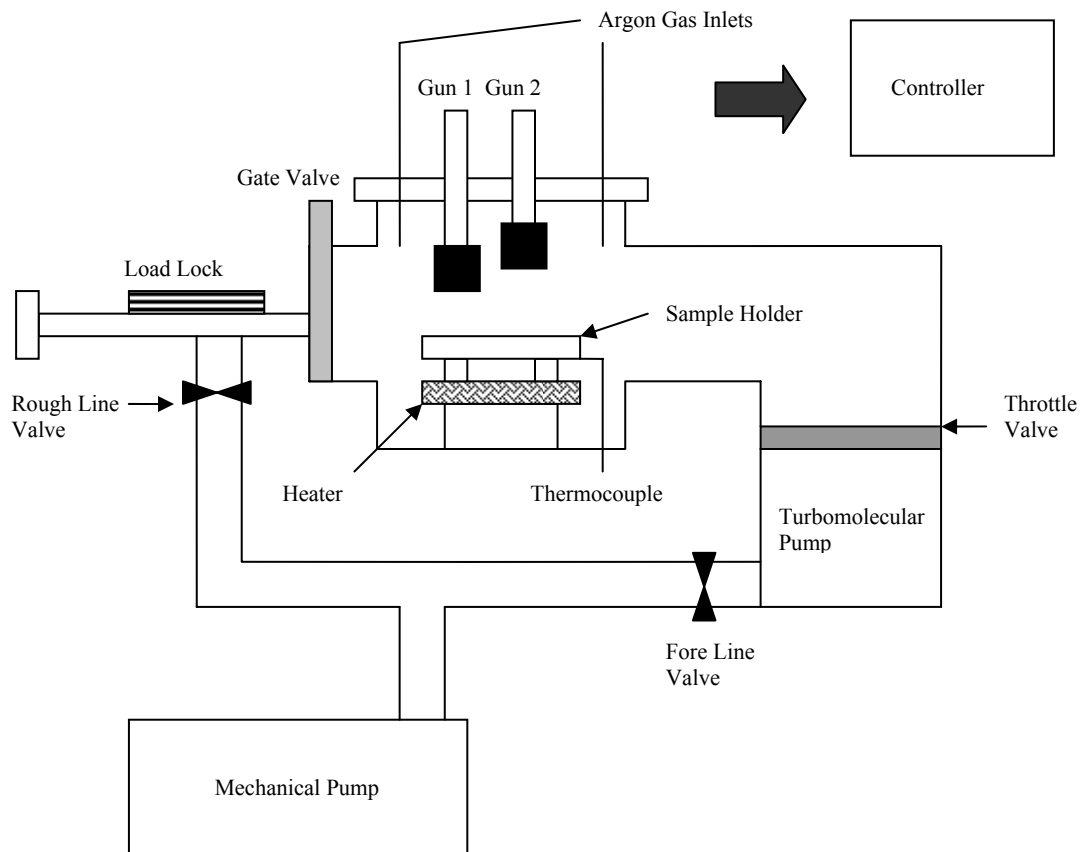


Figure 3.1 Schematic of sputter deposition system used for RF magnetron sputter deposition of ZnS:ErF_3 .

3.1.3 Post-Deposition Annealing

Sputter deposited films are annealed using nitrogen and water-cooled halogen lamps. A schematic of the annealing furnace is shown in Figure 3.2. The halogen lamps are located above and below a quartz tube to provide adequate heating. The quartz tube is loaded from one end and samples are placed on a graphite tray in the center. The tube is then compression sealed and purged with ultra high purity (99.9999%) N₂ gas for approximately 30 minutes. For this study annealing was performed at 425°C for 60 minutes. The nitrogen purge continues during the anneal and post-annealing cool down period until the sample reaches room temperature. A thermocouple is placed on the graphite tray to measure the sample temperature during annealing. The annealing cycle is controlled by a Micristar controller which allows for alteration of the ramp up and cool down profile. Typical ramping time to 425°C is 5 minutes.

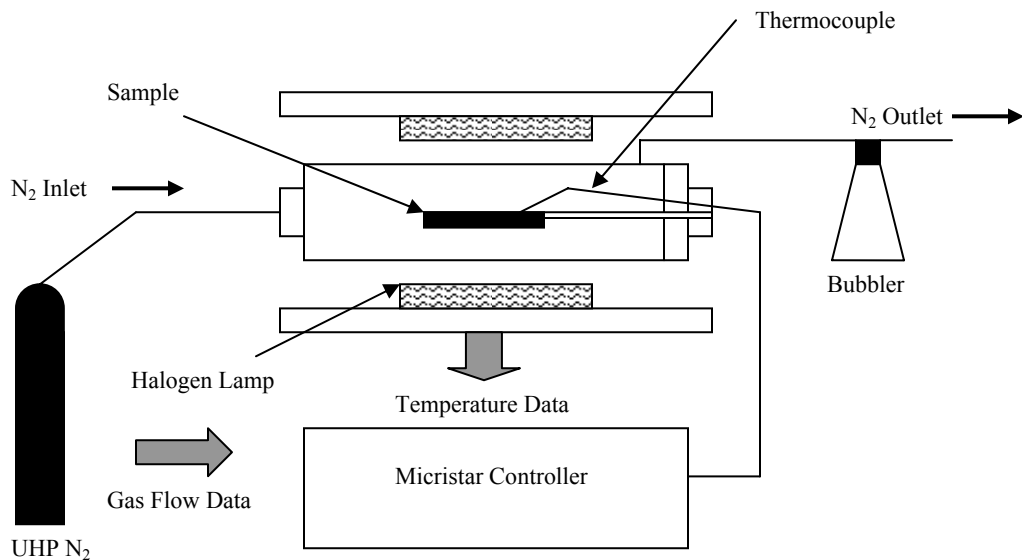


Figure 3.2 Schematic of thermal annealing furnace utilizing lamps as heating elements.

3.1.4 Electrode Deposition

All devices in this study used the half-stack configuration such that the top electrode was deposited directly onto the phosphor layer. Electrodes are needed on both sides of the phosphor to apply an electric field. The bottom electrode made of ITO was already deposited on the received substrates. The top electrode is made by thermally evaporating aluminum. A stainless steel shadow mask was used to create an array of aluminum contacts. Aluminum is evaporated using an Edwards Coating System E306 thermal evaporator. The aluminum contacts were circles with a diameter of 0.3 cm and a thickness between 200 and 230 nm. Electrical contact to the ITO layer is made by scratching through the phosphor and ATO layers with a diamond scribe. Pure indium is then melted onto the scratched surface such that it wets the bottom ITO electrode for electrical contact.

3.2 ACTFEL Characterization

3.2.1 Thickness Measurements

Along with ATO/ITO/glass substrates, bare glass Corning 7059 slides are placed in the sample holder. These slides are masked with glass microscope cover-slips during the deposition to create a step in the deposited film. Film thickness is measured by moving the tip of a Tencor (Alpha-Step 500) profilometer across the step in different areas. An average of the values is taken as the film thickness.

3.2.2 Electroluminescence Measurements

The optical properties of brightness and emission spectrum are measured for all deposited films. Electroluminescent (EL) emission is driven by a custom driver based on a design by Planar Systems, Inc. Devices are excited by applying a 2.5 kHz positive and negative trapezoidal pulses with a rise time of 5 μ s, a 30 μ s hold time and 5 μ s fall time.

Emitted light is analyzed using an Oriel MS257 0.25m monochromator using reflective optics. A chopper and lock-in detection scheme is used to improve the signal-to-noise ratio. Filter wheels are used at the input to the monochromator to prevent collection of secondary and tertiary harmonics. An Oriel model 77345, silicon-based photomultiplier tube (PMT) is attached to the off-axis port to detect emission up to 800 nm. An Oriel model 71614, thermo-electrically cooled germanium photodiode is attached to the on-axis port to detect emission up to 2 μm . An Oriel Merlin radiometry system interfaced with the monochromator and detectors utilizing custom software written with Visual Basic. The Merlin system also controlled the chopper. A schematic of the optical bench is shown in Figure 3.3.

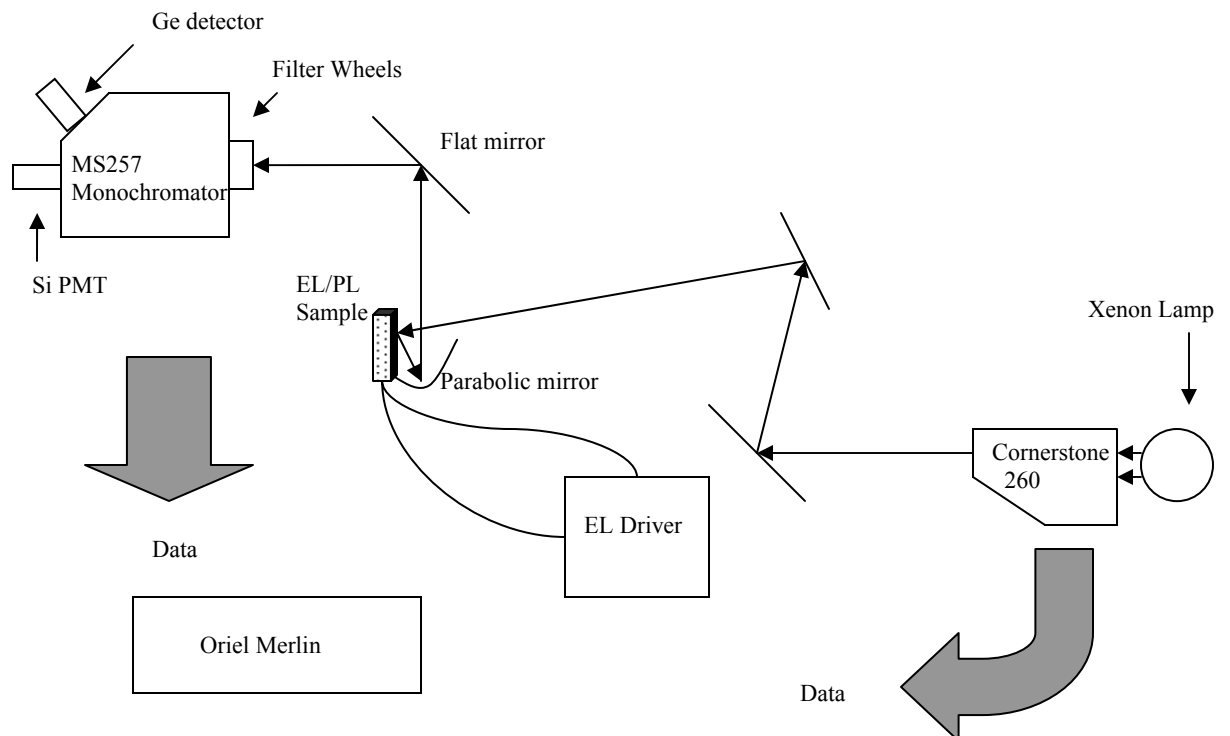


Figure 3.3 Schematic of optical bench for EL/PL measurement.

The spectrometer was calibrated using an Oriel model 63358 QTH calibrated lamp. The lamp utilized NIST standards in the 200-2400 nm range. A 1 cm² aperture was used and the lamp was placed 50 cm from the sample position to minimize reflected light. The full spectrum was measured using the fixed optics and monochromator settings so that a known irradiance value was produced at the sample position. This measurement provided a calibration curve, with units of $\mu\text{W}/\text{cm}^2 \cdot \text{V}$, that can be applied to collected data. Thus the irradiance of EL devices is obtained by measurements taken using the sample position, fixed optics and monochromator settings used during the collection of the correction curve. Irradiance is obtained by multiplying collected data, in V, by the calibration constant for a given wavelength, giving units of $\mu\text{W}/\text{cm}^2$.

3.2.3 Photoluminescence Measurement [101]

A Oriel model 66902 xenon lamp is used as the source for photoluminescent (PL) excitation. Excitation wavelength is selected by using an Oriel Cornerstone 260 source monochromator between the lamp and the sample. The monochromator is capable of producing wavelengths from 200-1200 nm. PL measurements are done at room temperature using the optical bench setup as shown in Figure 3.3. The emission spectrum is collected from 300-1800 nm using the proper filters, an Oriel model 77345, silicon-based (PMT) for visible emission and an Oriel model 71614, thermo-electrically cooled germanium photodiode for infrared emission.

3.2.4 Energy Dispersive Spectroscopy [102]

Energy dispersive spectroscopy (EDS) is used to verify chemical composition of the film. EDS uses the x-rays produced by high energy electron bombardment of the sample. A scanning electron microscope (SEM) is used to produce the electrons which inelastically scatter off of the atomic components of the film. This causes an inner shell

electron to be ejected from the atom. As an outer shell electron de-excites to fill the inner shell hole either an Auger electron or characteristic x-ray is produced. In EDS, the characteristic x-rays are collected by a silicon diode producing a charge pulse proportional to the energy of the incident x-ray. The pulses are amplified and adjusted to produce a spectrum of the incident x-ray energies [102].

A JEOL 6400 SEM is used in conjunction with an EDS detector to analyze x-rays produced by the samples. Primary electrons are generated by thermionic emission from a tungsten filament. The operating voltage must equal or exceed 10 kV as the L emission line of the rare earth requires this energy for excitation. Typically the operating voltages used are 20 kV to allow for greater penetration into the sample and greater excitation depth. Samples are tilted to prevent electron penetration into the ATO layer. Tested samples consisted of half-stack devices without the top electrode. Samples were not coated as the ITO layer provided a sufficiently conductive pathway so that charging did not occur. Additionally, carbon stickers were used to attach samples to the sample holder to prevent charging. Rare earth standards are used as references for determining concentration in samples.

3.2.5 Electron Probe Micro Analysis [103]

Electron probe x-ray microanalysis (EPMA) is a quantitative analysis technique used to provide chemical composition data of the samples. This technique uses highly energetic electrons to eject core level electrons from the atomic components of the film. The core level vacancy is filled by an outer level electron producing a characteristic x-ray as described above. In EPMA, the wavelength and intensities of the characteristic x-rays provide the chemical composition information. EPMA uses linear focusing spectrometers to determine the energy of the x-rays [103]. The geometry of the spectrometer allows for

high x-ray intensities and wavelength resolution. A JEOL Superprobe 733 is used for the samples of this study. Primary electrons are generated by thermionic emission from a tungsten filament. Because high beam currents, $\sim 20\text{nA}$, are used in microprobe analysis the operating voltage is substantially lower than that needed for EDS.

3.2.6 Secondary Ion Mass Spectroscopy [101]

Secondary ion mass spectroscopy (SIMS) is a quantitative characterization technique that provides a high degree of element sensitivity and excellent depth resolution. A beam of primary ions is used to sputter the sample surface. The primary beam used depends on the elements to be studied. For electropositive elements, like Na, Ca and transition metals, an oxygen ion beam is used. For electronegative elements, like C, N and O, a cesium primary beam is used. The positive and negative secondary ions formed during sputtering are analyzed using a quadrupole mass spectrometer. The continuous sputtering of the sample surface and analysis of resulting secondary ions allows for monitoring of specific elements as a function of depth. This technique is known as dynamic SIMS. A Perkin-Elmer/Physical Electronics 6600 Quadrupole Dynamic SIMS system is used to analyze the samples in this study. [101]

3.2.7 Electrical Measurements

A detailed review of the electrical characterization is given in section 2.6.2.2. For electrical characterization, a voltage is applied to the device. This voltage is applied as 2.5 kHz trapezoidal pulses as described in section 3.2.2. A Tektronix TDS 2024 digitizing oscilloscope is used to measure the voltage at points V_1 , V_2 and V_3 shown in Figure 2.11. The sense element used is a 60.4 nF capacitor. The external charge ($Q_{\text{ext}}(t)$) is determined by equation 2.12. Electrical data is collected with the aluminum electrode under positive and negative polarities.

3.2.8 Statistical Analysis

The data produced from luminescence and chemical analysis measurements is analyzed using a Minitab version 14.2 statistical software package [104]. Statistical analysis is employed to summarize or describe the data as well as understand inferences that may be drawn as a result. This analysis also provides a methodology to distinguish between random and systematic errors in the data. A design-of-experiments is used to evaluate the critical experimental parameters and enable statistical analysis of the data. Specifically, a full factorial experiment is used in which each experimental run is characterized by all of the critical factors. Analysis of variance is then performed to determine which of the variables results in a statistically significant change in the electroluminescent brightness.

CHAPTER 4
EFFECTS OF PHOSPHOR LAYER PROCESSING PARAMETERS ON
ELECTROLUMINESCENCE AND CHEMICAL COMPOSITION

4.1 Introduction

The effects of parameters used during RF magnetron sputtering, as well as post-deposition annealing, on infrared electroluminescence (EL) from ZnS:ErF₃ ACTFEL devices are reported in this chapter. The experimental procedures used are given followed by the effect that each parameter had on the optical and chemical characteristics of the devices. Erbium possesses a near infrared optical transition at 1550 nm, which has potential applications in optical communication and advanced wound healing therapy. The emission is the result of excitation and radiative relaxation of erbium luminescent centers in the phosphor film. As a result, the concentration of erbium ions in the film is important. The fluorine counter-ion used for charge balance in the films is also important to the resulting emission [84]. The purpose of this study was to investigate the effects and interrelationships of critical processing parameters on ACTFEL devices.

ZnS:ErF₃ ACTFEL devices have several EL emission peaks [79]. Significant visible emission at 525 and 550 nm corresponds to $^2H_{11/2} \rightarrow ^4I_{15/2}$ and $^4S_{3/2} \rightarrow ^4I_{15/2}$ transitions, respectively. Near infrared emission at 1550 nm corresponds to the $^4I_{13/2} \rightarrow ^4I_{15/2}$ transition. Additional emission peaks occur at 662, 985 and 1300 nm corresponding to the $^4F_{9/2} \rightarrow ^4I_{15/2}$, $^4F_{7/2} \rightarrow ^4I_{11/2}$ and $^4S_{3/2} \rightarrow ^4I_{11/2}$ transitions, respectively. The energy levels and transitions for Er are shown in Figure 4.1 [79].

A typical visible electroluminescence (EL) emission spectrum showing the 525 and 550 nm transitions for ZnS:ErF₃ ACTFEL devices is shown in Figure 4.2. A typical near infrared emission spectrum from the 1550 nm transition is shown in Figure 4.3. An Oriel model 63358 QTH calibrated lamp did not produce detectable photoluminescence emission from these ZnS:ErF₃ layers.

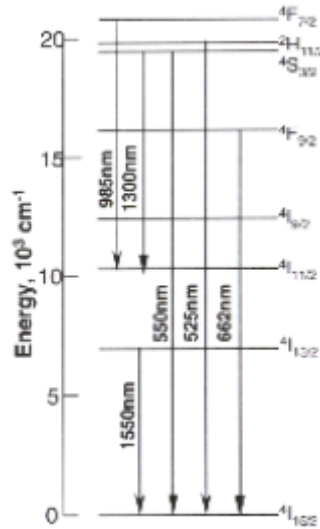


Figure 4.1 Energy levels and transitions of ZnS:ErF₃ ACTFELDs that produce luminescence shown in Figure 4.2 and Figure 4.3 [79].

The effects on the EL emission of variations during sputter deposition substrate temperature (120°C and 150°C), duty cycle on the doped target (25% and 75%) and sputtering gas pressure (1 mTorr and 24 mTorr) and of post-deposition annealing temperature (as-deposited and 425°C for 1 hr in N₂) were investigated, as well as effects on the resulting change in chemical composition. Each variable was altered with respect to the others to produce eight pair of data for each deposition parameter. Applied power to the sputter targets was maintained at 100 W for all samples produced, and the duty cycle on the undoped ZnS source was constant at 100%.

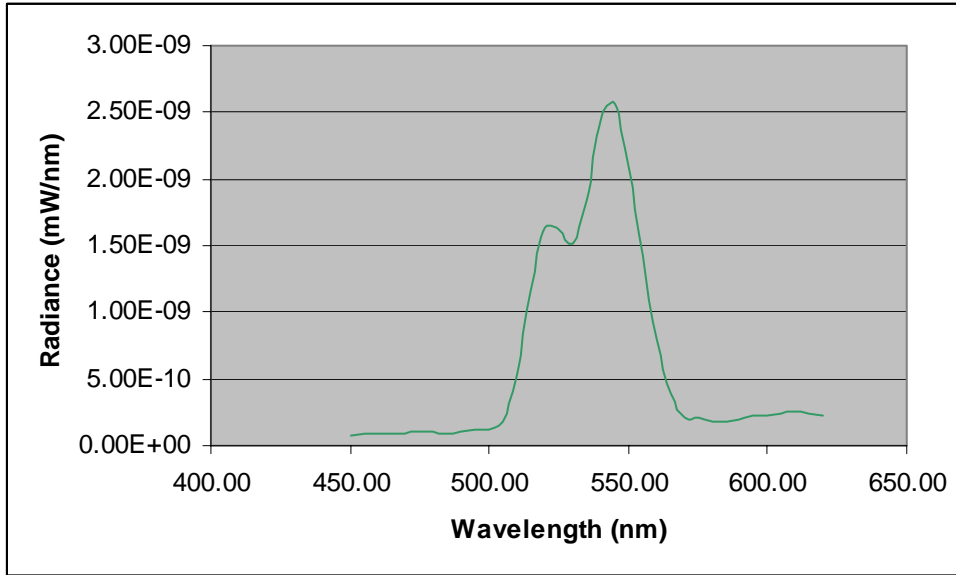


Figure 4.2 Typical visible emission at 525 and 550 nm for ZnS:ErF₃ ACTFEL devices.

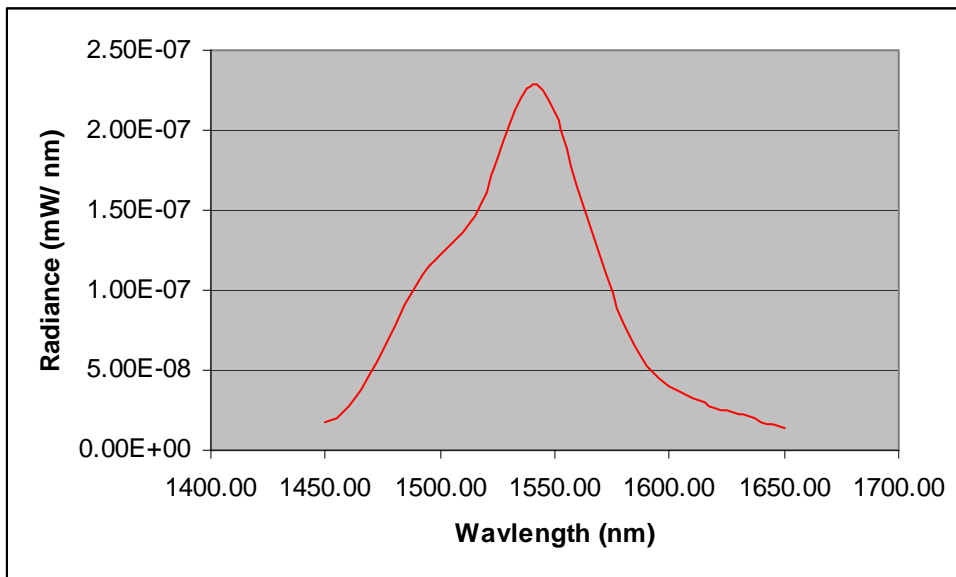


Figure 4.3 Typical near infrared emission at 1550 nm for ZnS:ErF₃ ACTFEL devices.

4.2 Experimental Procedure

The EL phosphors consisted of ZnS:ErF₃ thin films that were RF magnetron sputter deposited onto standard glass/indium tin oxide-ITO/aluminum-titanium oxide-ATO substrates. The process flow for device fabrication is shown in Figure 4.4 and consisted of the “half-stack” structure described in Section 2.3.

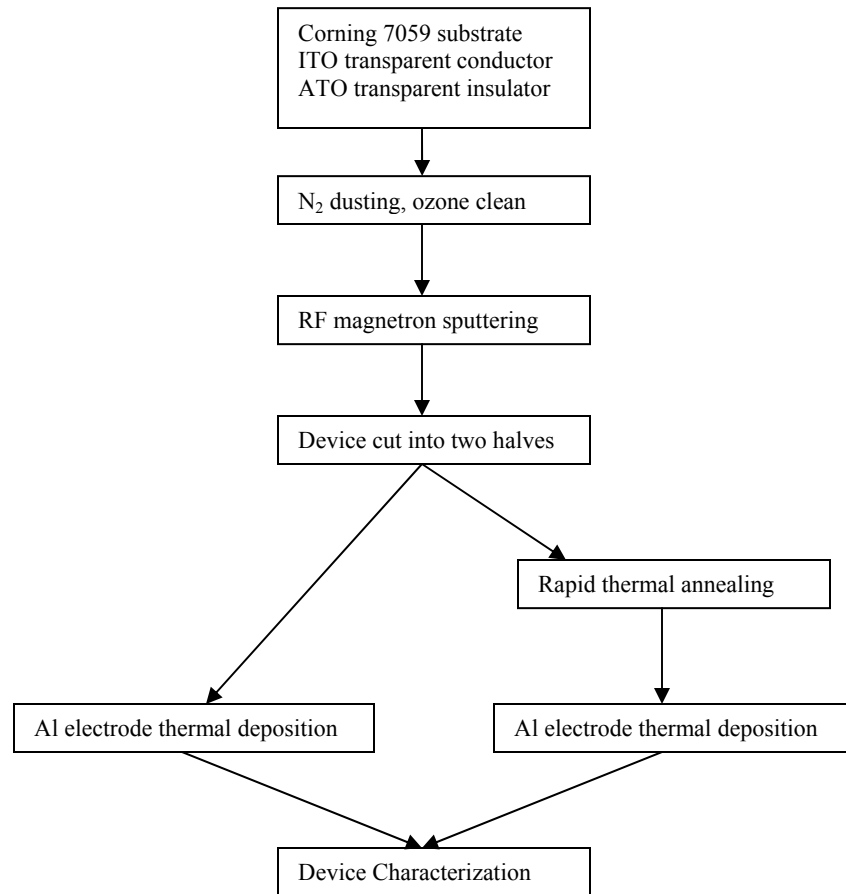


Figure 4.4 Schematic of the process flow for ZnS:ErF₃ ACTFEL devices fabrication.

4.2.1 Substrate

Substrates consist of Corning 7059 glass, 0.04 inches thick, coated with 360 nm of polycrystalline indium tin oxide (ITO) (90 wt% In₂O₃ + 10 wt% Sn₂O₃) as the transparent conducting electrode and 160 nm of amorphous aluminum titanium oxide (ATO) (Al₂O₃ / TiO₂) as the bottom insulating layer. These were supplied by Planar Systems. The ATO dielectric layer was deposited by atomic layer deposition (ALD) to ensure a high quality, homogeneous insulator. Each substrate is first dusted using dry nitrogen gas to remove airborne particulate. Substrates are also cleaned in a UVOCS, Inc. ultraviolet light ozone

cleaner for six minutes to remove organic contaminants. Additional substrates of bare Corning 7059 glass were prepared using the same method for use in thickness measurement.

4.2.2 Phosphor Layer Deposition

The ZnS:ErF₃ phosphor layer is deposited by two independently controlled RF magnetron sputter guns. One sputter gun contains a CVD grown polycrystalline pure ZnS target source purchased from Morton Thiokol, Inc. The other sputter gun uses a ZnS:ErF₃ compound target purchased from SCI Engineering Materials. The doped target is prepared by mixing 98.5 wt% ZnS powder and 1.5 wt% ErF₃ powder and hot pressing in inert gas to form the target. The coated glass substrates are placed on a sample platter with the capacity for four 2" x 2" substrates or eight 2" x 1" substrates. These are rotated at a speed of 8 revolutions per minute. The deposition chamber is evacuated to a base pressure between 6.5×10^{-7} and 1×10^{-6} Torr prior to phosphor deposition. Argon is used as the sputter gas and is introduced into the chamber using Unit UFC 1100A 20, 50 or 100 sccm mass flow controllers on three inlet lines. The power applied to both the targets was 100 W for all samples, but the duty cycle for the doped target was varied from 25% to 75%. Additional deposition conditions are discussed in corresponding sections of Section 4.3.

Following phosphor layer deposition, a portion of the devices were annealed in a quartz tube with an ultra high purity nitrogen (99.9999%) ambient at 425°C for 60 minutes prior to deposition of the opaque top electrode. Halogen lamps placed above and below the quartz tube provided appropriate heating. The temperature inside the quartz tube was monitored by a thermocouple in conjunction with a Micristar controller used to

control the power applied to the heating lamps. Samples not annealed are noted to have been measured at room temperature (25°C).

4.2.3 Top Opaque Electrode

The top opaque electrode is deposited by thermal evaporation of aluminum. A shadow mask with a circular dot size of 0.069 cm^2 is used. Aluminum is evaporated using an Edwards Coating System E306 thermal evaporator to a thickness of 225 nm. The base pressure for this process is approximately 1×10^{-6} Torr. Electrical contact to the bottom (ITO) electrode is made by scratching through the phosphor layer and dielectric layer with a diamond-tip scribe. A pure indium metal is then melted, using a soldering iron, into the scratch such that it wets the ITO layer resulting in electrical contact to the layer.

4.2.4 Chemical Composition Analysis

In this study, the chemical constituents of the film were characterized using secondary ion mass spectroscopy (SIMS) [101] and by energy dispersion spectroscopy (EDS) on the scanning electron microscope (SEM) [102]. SIMS is a quantitative characterization technique that provides a high element sensitivity and excellent depth resolution. A beam of primary ions is used to sputter the sample surface. For electropositive elements, like Zn, Er and Al, an oxygen ion beam is used. For electronegative elements, like S, F and O, a cesium primary beam is used. The positive and negative secondary ions formed during sputtering are analyzed using a quadrupole mass spectrometer. The continuous sputtering of the sample surface and analysis of resulting secondary ions allows monitoring of specific elements as a function of depth. This technique is known as dynamic SIMS. A Perkin-Elmer/Physical Electronics 6600 Quadrupole Dynamic SIMS system is used to analyze the samples in this study [101].

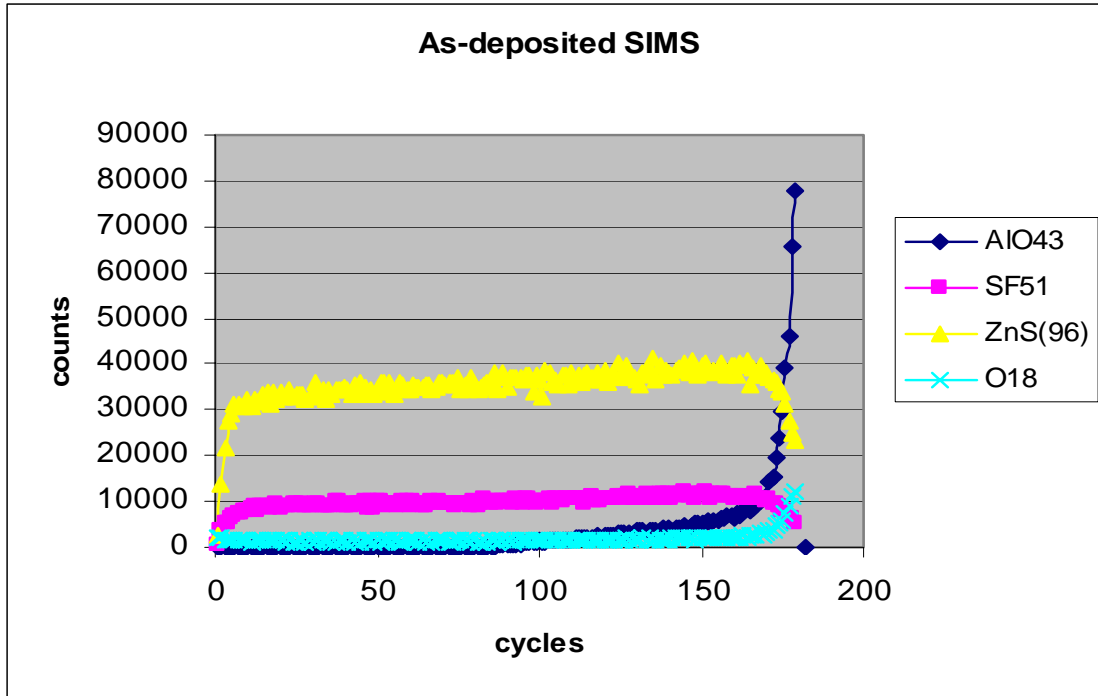


Figure 4.5 Typical negative ion SIMS spectrum for as-deposited ZnS:ErF₃ phosphor layer.

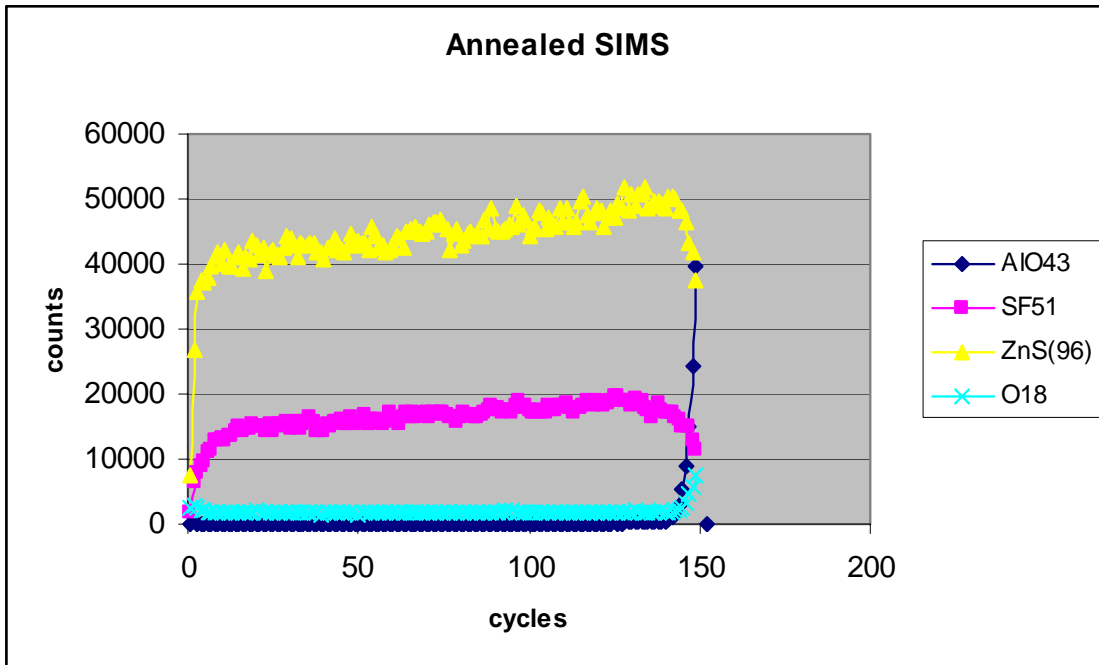


Figure 4.6 Typical negative ion SIMS spectrum for ZnS:ErF₃ phosphor layer after annealing at 425°C for 1 hr in N₂.

Typical negative ion SIMS spectra from an as-deposited and an annealed ZnS:ErF₃ ACTFEL film are shown in Figures 4.5 and 4.6, respectively. The spectra were collected using a 5 keV, 83nA rastered cesium primary ion beam. The raster size was 400x400 μm^2 with 65% gating. At least two profiles were acquired for each sample to check for reproducibility which was judged to be good. The signal for F was acquired as mass to charge $^{51}\text{SF}^-$, and the balance of the species was acquired as $^{96}\text{ZnS}^-$, $^{18}\text{O}^-$ and $^{43}\text{AlO}^-$. The sensitivity factors for quantifying the F concentration in ZnS were determined from a ZnS standard implanted with ^{19}F (100keV, $5.6 \times 10^{14}/\text{cm}^2$). To quantify the F SIMS concentrations, the intensity ratio of $^{51}\text{SF}^-$ to the matrix ion (^{96}ZnS) is calculated, and multiplied by the F sensitivity factor.

For analysis of $^{166}\text{Er}^+$ and $^{66}\text{Zn}^+$ secondary ions, a 6 keV, 72 nA O_2^+ primary ion beam was used with a raster size 350 x 350 μm^2 and 65% grating. Again, two profiles were acquired for each sample to verify reproducibility. No standard was available for erbium so the profiles are plotted as the ratio of erbium-to-zinc (Er/Zn) in the film.

4.3 Processing Parameters

4.3.1 Substrate Temperature

The substrates are radiatively heated during phosphor deposition by resistive carbon cloth heaters located underneath the sample holder. The deposition temperature was either 120°C or 150°C. After annealing, if appropriate, and deposition of the top contact, EL from the devices were measured using an Oriel MS257 monochromator using reflective optics fitted with a silicon-based PMT (visible emission) or a thermoelectrically cooled germanium photodiode (NIR). Several brightness vs. voltage data sets were measured using each set of deposition parameters. The values of brightness, threshold voltage, etc. reported below are the average values of at least two

and as many as seven data points from the same sample or samples with the same treatment. The primary EL peak monitored was that at 1550 nm. The threshold voltage and brightness value at 20 volts above threshold (B_{20}) are derived from these data, as described in Chapter 3. Deposition time was varied between 120-150 minutes to produce films with thicknesses of $650 \text{ nm} \pm 15\%$.

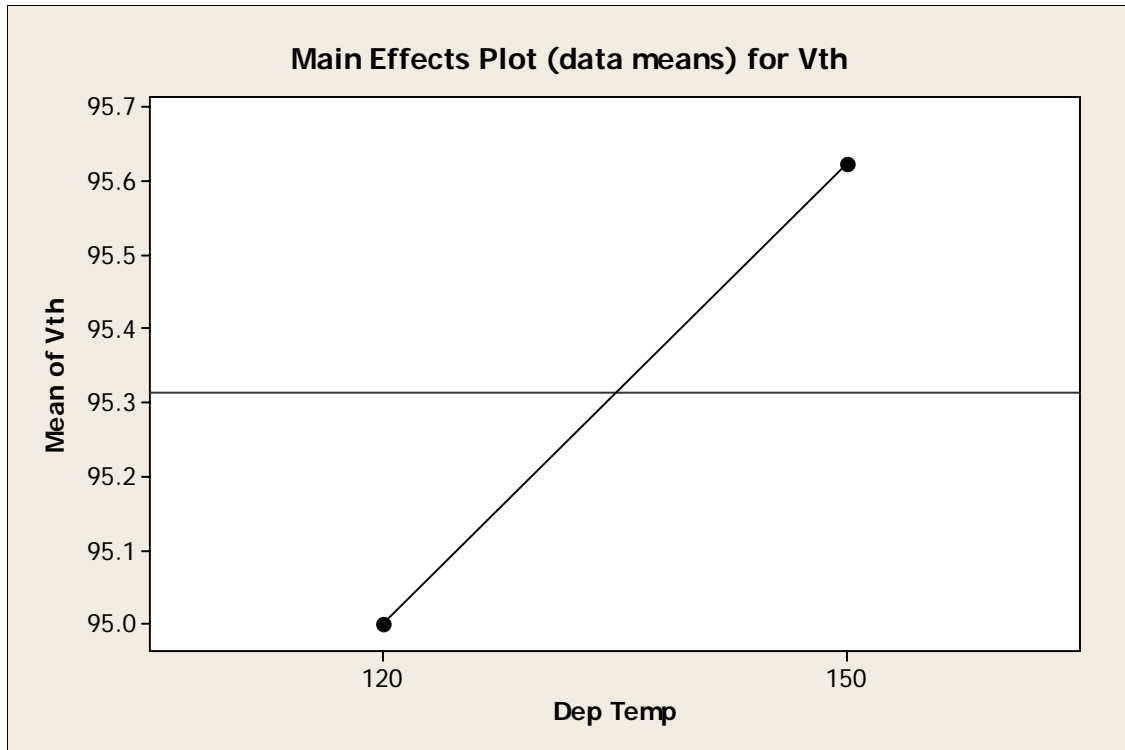


Figure 4.7 Effect of deposition temperature on threshold voltage for ZnS:ErF₃ ACTFELDs.

Threshold voltage is plotted versus deposition temperature of either 120°C or 150°C in Figure 4.7. The change in threshold voltage is insignificant (a change of only 0.625 V for $V_{th} \sim 95\text{V}$, i.e. <1%) for a significant change in deposition temperature. Increased film thickness will result in increases in V_{th} due to the requirement of a high electric field to reach electrical breakdown of the phosphor film. Film thicknesses were only constant to within $\pm 15\%$ at approximately 650 nm.

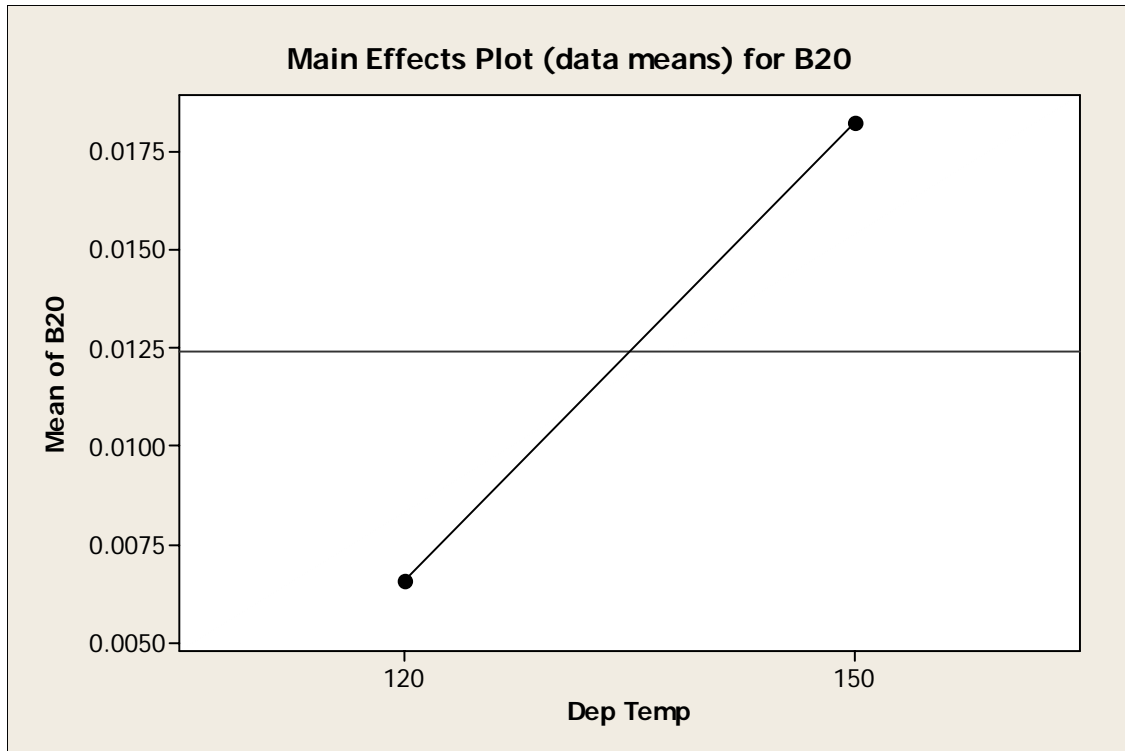


Figure 4.8 Effect of deposition temperature on B₂₀ for ZnS:ErF₃ ACTFELDS.

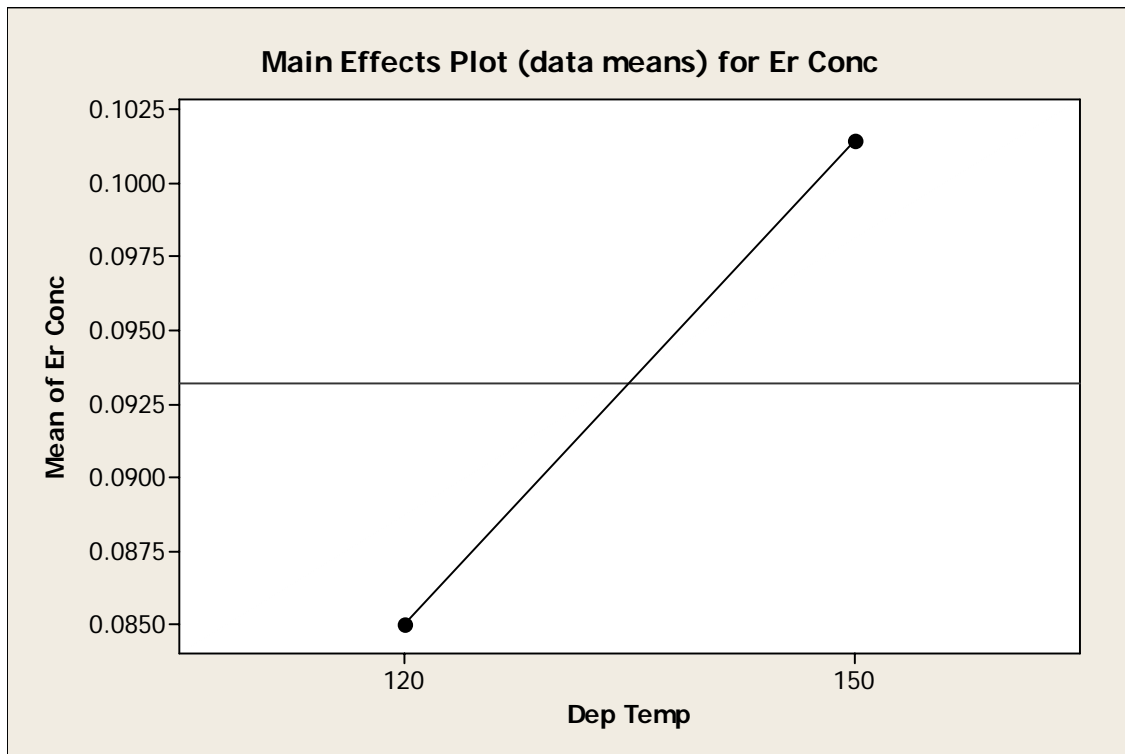


Figure 4.9 Effect of deposition temperature on Er/Zn ratio for ZnS:ErF₃ phosphor films.

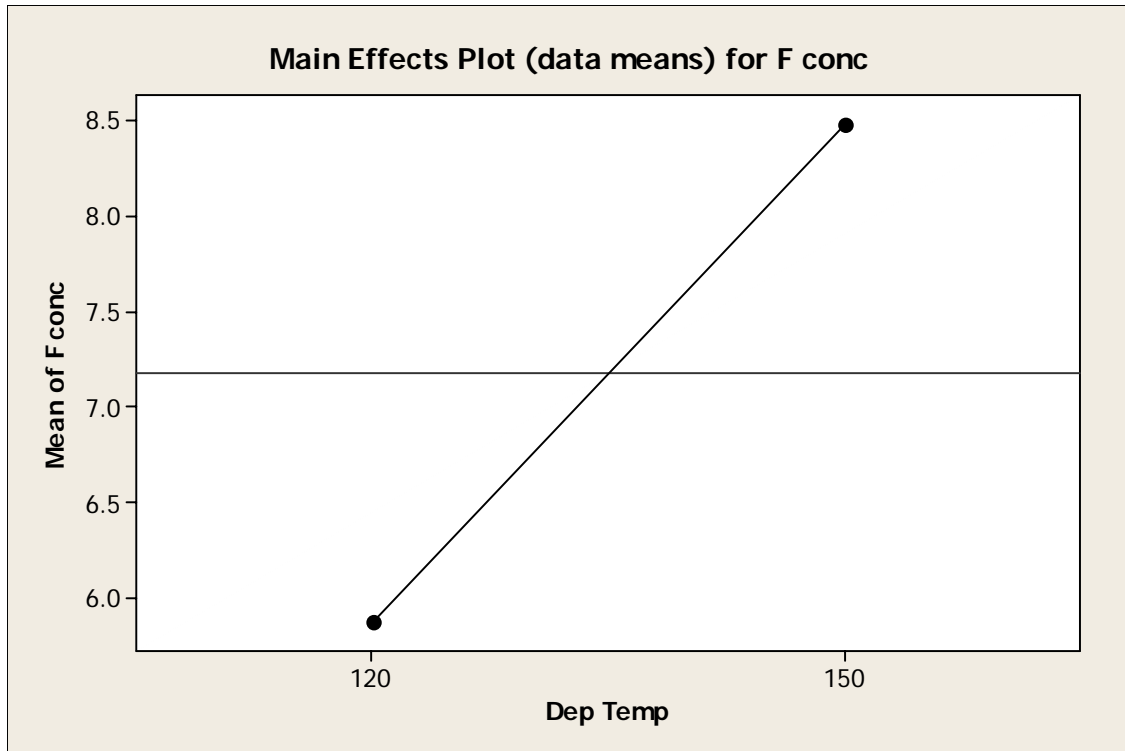


Figure 4.10 Effect of deposition temperature on F concentration [cm^{-3}] for ZnS:ErF₃ phosphor films.

Table 4.1 Processing parameters and Er and F concentrations for ZnS:ErF₃ phosphors.

Dep T (°C)	Duty Cycle	Pressure (mTorr)	Anneal (°C)	Er/Zn	F conc ($\times 10^{20} \text{ cm}^{-3}$)
120	25	1	25	0.072	8.18
120	25	1	425	0.058	2.72
120	25	24	425	0.048	1.32
120	25	24	25	0.065	7.58
120	75	24	25	0.049	5.00
120	75	24	425	0.086	4.21
120	75	1	425	0.184	7.21
120	75	1	25	0.117	10.80
150	75	1	25	0.209	7.79
150	75	1	425	0.139	8.34
150	75	24	425	0.094	4.23
150	75	24	25	0.082	22.69
150	25	24	25	0.058	2.72
150	25	24	425	0.067	8.55
150	25	1	425	0.092	4.22
150	25	1	25	0.071	5.64

An increase in brightness, in arbitrary units, of the 1550 nm emission measured 20 V above threshold (B_{20}) was measured with increasing deposition temperature as shown in Figure 4.8. In this case, the brightness increases from 0.0066 at 120°C to 0.0182 at 150°C, a significant increase of approximately 180%.

The erbium concentration in the ZnS films showed a small change with increasing deposition temperature as shown in Table 4.1. The ratio of Er/Zn of 0.085 at 120°C increased to 0.101 at 150°C as shown in Figure 4.9. This represents an increase of approximately 5% which is within the margin of error (~30%). The fluorine concentration showed a larger increase with increasing temperature. The increase in fluorine from $5.8 \times 10^{20} \text{ cm}^{-3}$ at 120°C to $8.5 \times 10^{20} \text{ cm}^{-3}$ at 150°C ($\Delta \sim 44\%$) is shown in Figure 4.10.

4.3.2 Duty Cycle Applied to Doped Target

The duty cycle applied to a sputtering target refers to the percentage of time where power is applied. Duty cycles were varied between 25% and 75% on the ZnS:ErF₃ doped target. The power applied to both doped and undoped targets was maintained at 100 W for all samples, and the duty cycle used for the undoped target was kept constant at 100%.

The threshold voltage, V_{th} , significantly increased with increasing duty cycle, as shown in Figure 4.11. The threshold voltage increases from 77.5 V at 25% to 113 V at 75%, a difference of ~45%. The brightness of the 1550 nm emission at 20 V above threshold increases by a factor of six for 75% duty cycle. The increase in B_{20} with

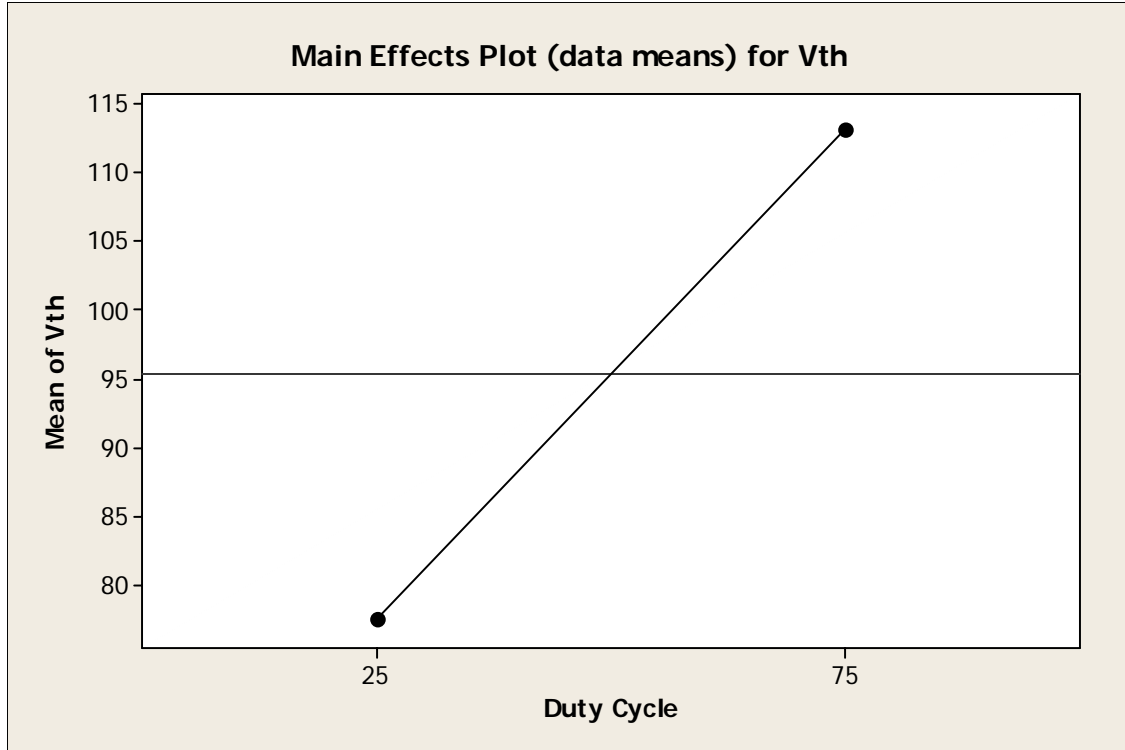


Figure 4.11 Effect of duty cycle on threshold voltage for ZnS:ErF₃ ACTFELDs.

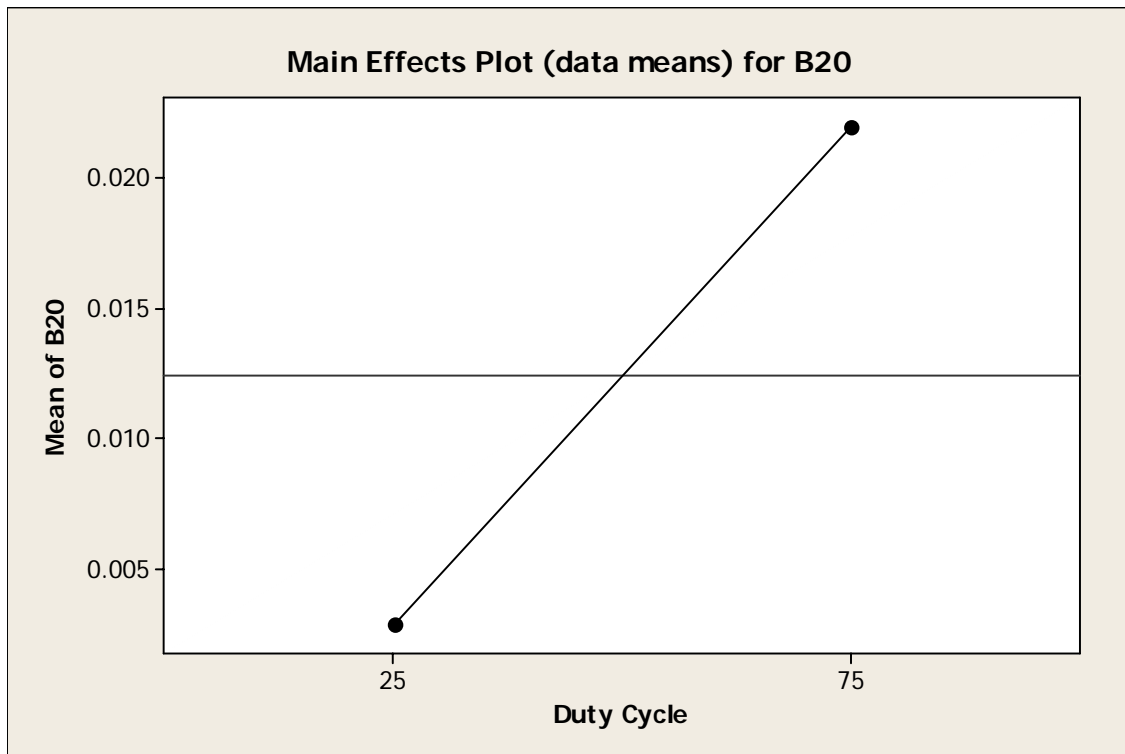


Figure 4.12 Effect of duty cycle on B₂₀ for ZnS:ErF₃ ACTFELDs.

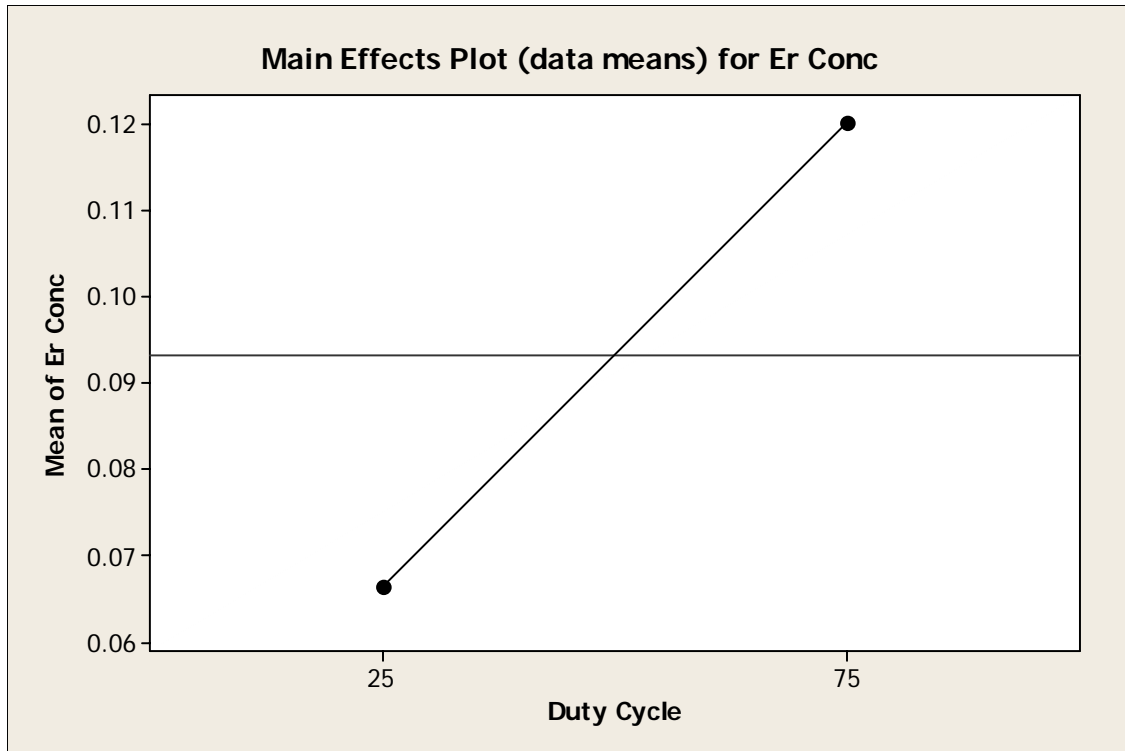


Figure 4.13 Effect of duty cycle on Er/Zn ratio for ZnS:ErF₃ phosphor films.

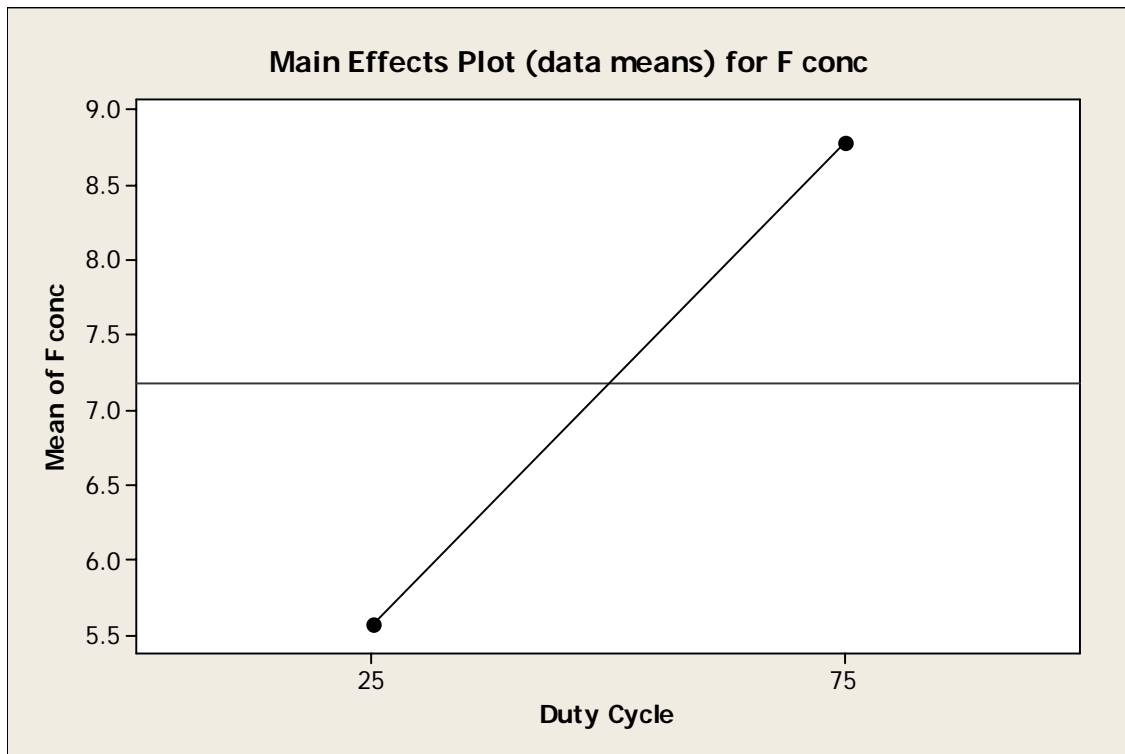


Figure 4.14 Effect of duty cycle on F concentration [cm⁻³] for ZnS:ErF₃ phosphor films.

increasing duty cycle is shown in Figure 4.12. Brightness increases from 0.0029 at 25% to 0.0219 at 75%. This represents an increase of approximately 650%.

The erbium concentration significantly increased with increasing duty cycle. The Er/Zn ratio at 25% duty cycle was 0.066 and at 75% duty cycle the ratio was 0.12, as shown in Figure 4.13, for an increase of ~80%. The fluorine concentration data mirrors the significant increase in the erbium data, increasing from $5.1 \times 10^{20} \text{ cm}^{-3}$ at 25% duty cycle to $8.8 \times 10^{20} \text{ cm}^{-3}$ at 75% duty cycle as shown in Figure 4.14. This represents an increase of ~70% in F concentration.

4.3.3 Sputtering Gas Pressure

The argon sputtering gas is introduced into the deposition chamber by means of mass flow controllers and multiple gas inlets. A throttle valve between the deposition chamber and the turbomolecular pump is used to keep the vacuum pressure sufficiently high to maintain the plasma for sputtering. The pressure was varied between 1 mTorr and 24 mTorr. Increasing the argon sputtering gas pressure from 1 to 24 mTorr does not cause a significant change in the threshold voltage (95 V and 95.6 V) as shown in Figure 4.15. This increase of 0.6 V means that no statistically significant change resulted from the increase in sputtering gas pressure. However the B_{20} of the 1550 nm emission increased with increasing argon sputtering gas pressure as shown in Figure 4.16. The brightness increased from 0.0089 at 1 mTorr to 0.0159 at 24 mTorr, an increase of ~80%. The erbium-to-zinc ratio is 0.118 and 0.069 for sputter gas pressures of 1 and 24 mTorr, respectively, representing a 40% decrease as shown in Figure 4.17. In contrast, the fluorine concentration data is virtually constant with sputtering gas pressure, being 6.9×10^{20} and $7.0 \times 10^{20} \text{ cm}^{-3}$ at 1 and 24 mTorr, respectively, as shown in Figure 4.18.

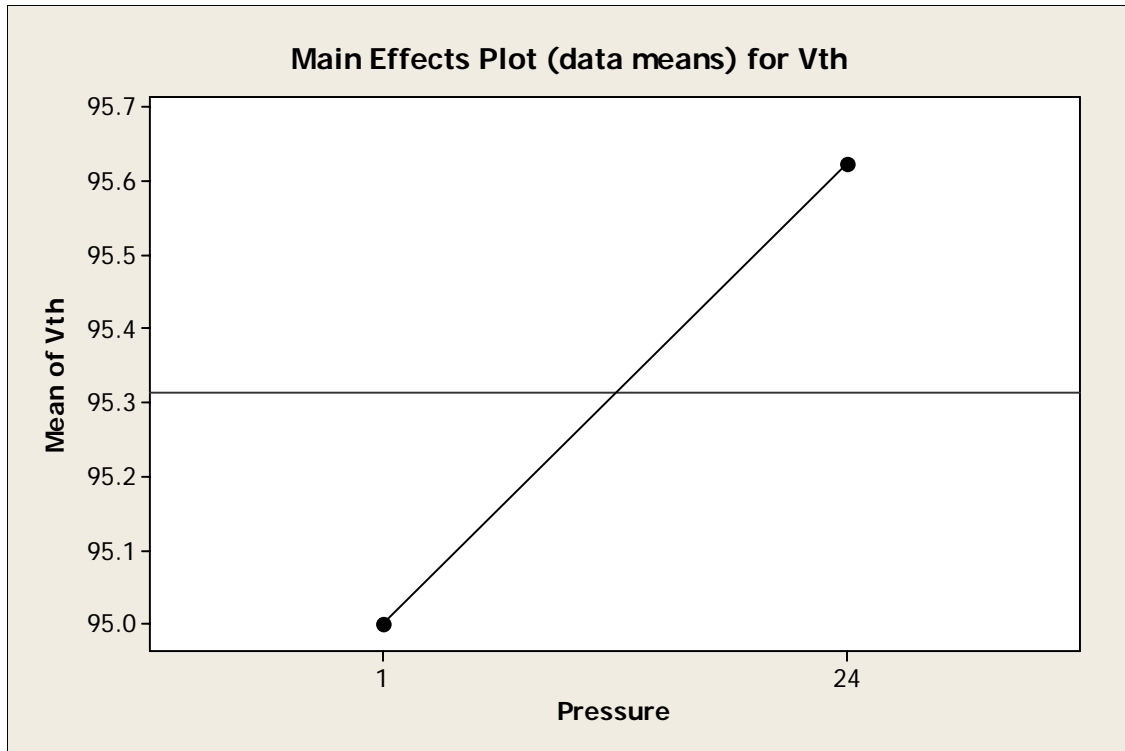


Figure 4.15 Effect of Ar sputtering gas pressure on threshold voltage for ZnS:ErF₃ ACTFELDs.

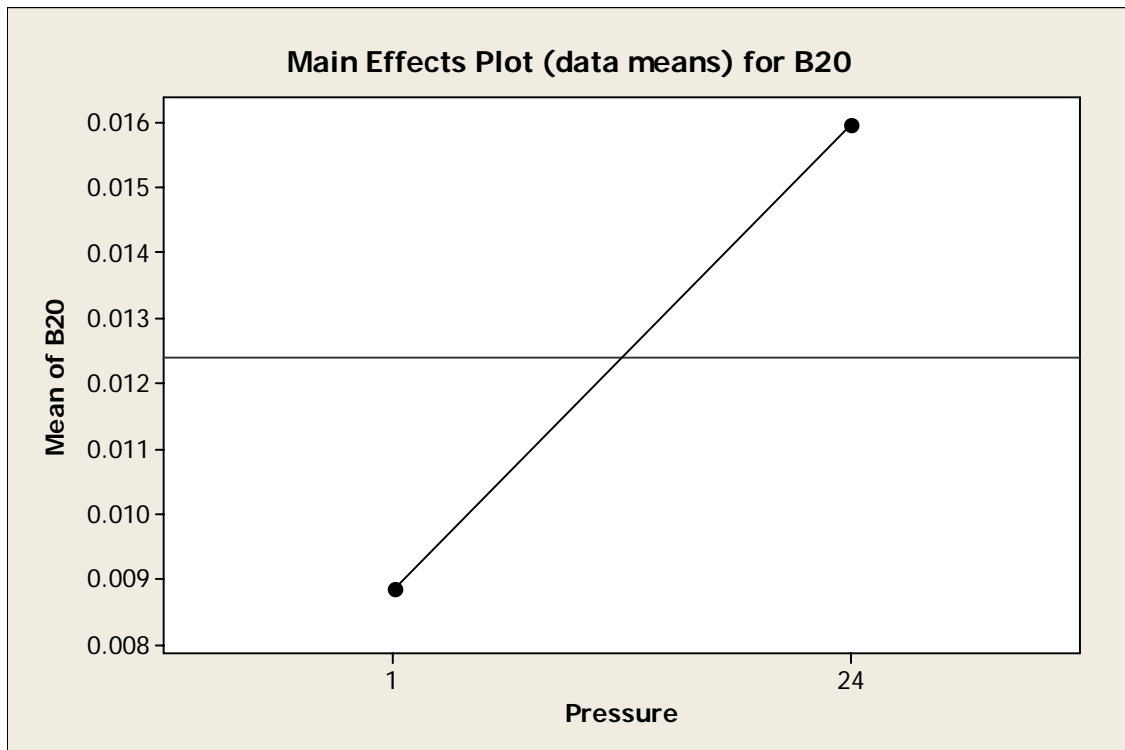


Figure 4.16 Effect of Ar sputtering gas pressure on B₂₀ for ZnS:ErF₃ ACTFELDs.

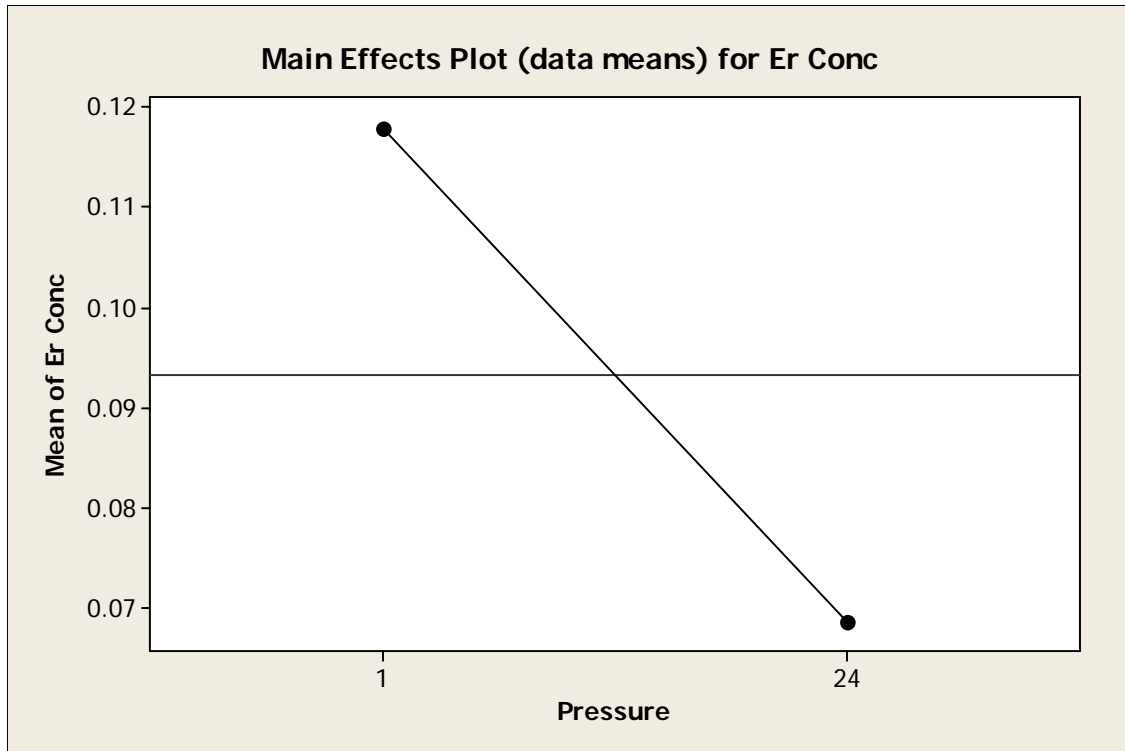


Figure 4.17 Effect of Ar sputtering gas pressure on Er/Zn ratio for ZnS:ErF₃ phosphors.

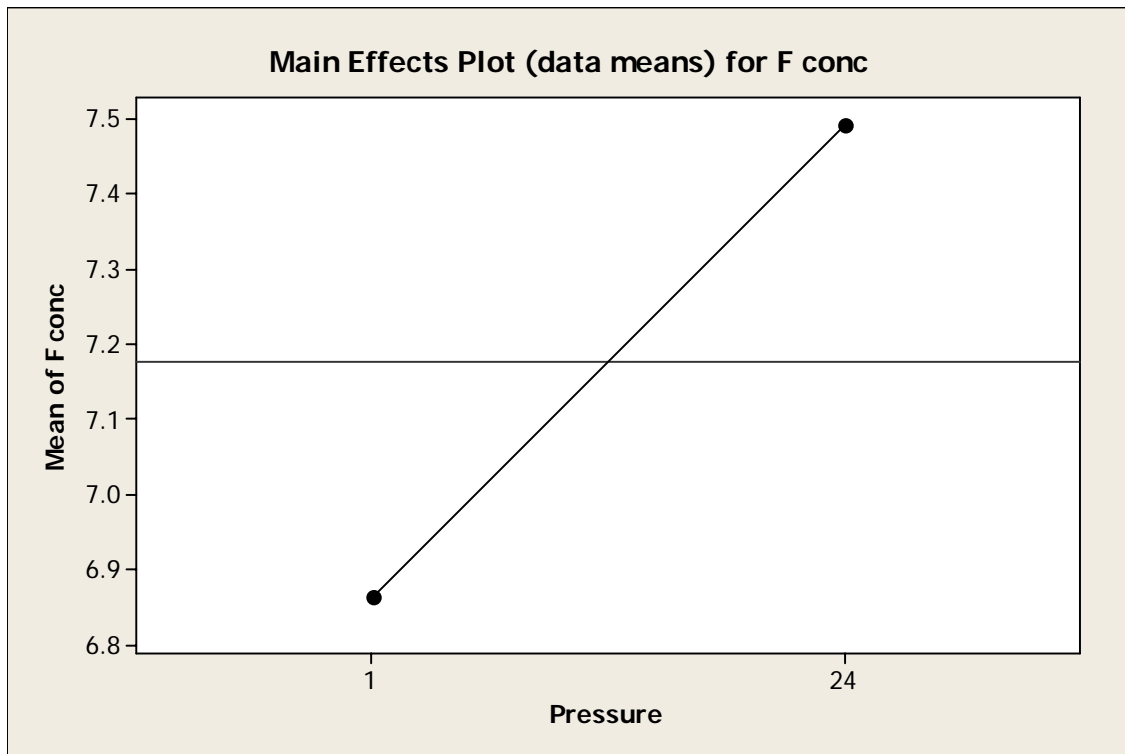


Figure 4.18 Effect of Ar sputtering gas pressure on F concentration [cm⁻³] for ZnS:ErF₃ phosphors.

4.3.4 Post-Deposition Annealing Temperature

Annealing of samples at 425°C resulted in a statistically insignificant increase in threshold voltage of 1.9 V compared to as-deposited samples. The brightness of the 1550 nm emission increased from 0.0097 to 0.0152 (~60%) after annealing shown in Figure 4.20. The change in the Er/Zn ratio from 0.090 to 0.096 with annealing (shown in Figure 4.21) is not statistically significant. The fluorine concentration, however, shows a marked reduction from 8.8×10^{20} to $5.1 \times 10^{20} \text{ cm}^{-3}$ for as-deposited and annealed films, respectively, as shown in Figure 4.22. This is a decrease of ~40%. The effect of post-deposition annealing on oxygen concentration is shown in Figure 4.23. The oxygen concentration was calculated as the ratio of O/ZnS. Oxygen concentration decreased from 0.046 for as-deposited samples to 0.041 for annealed samples.

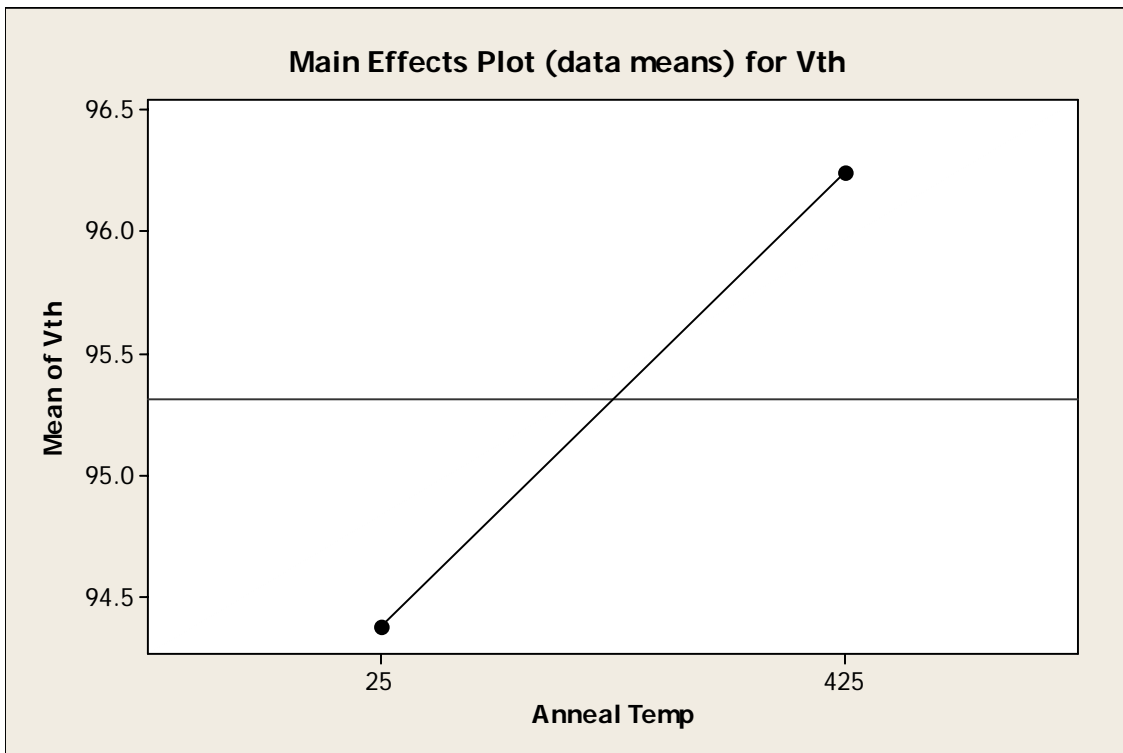


Figure 4.19 Effect of post-deposition annealing on threshold voltage for ZnS:ErF₃ ACTFELDs.

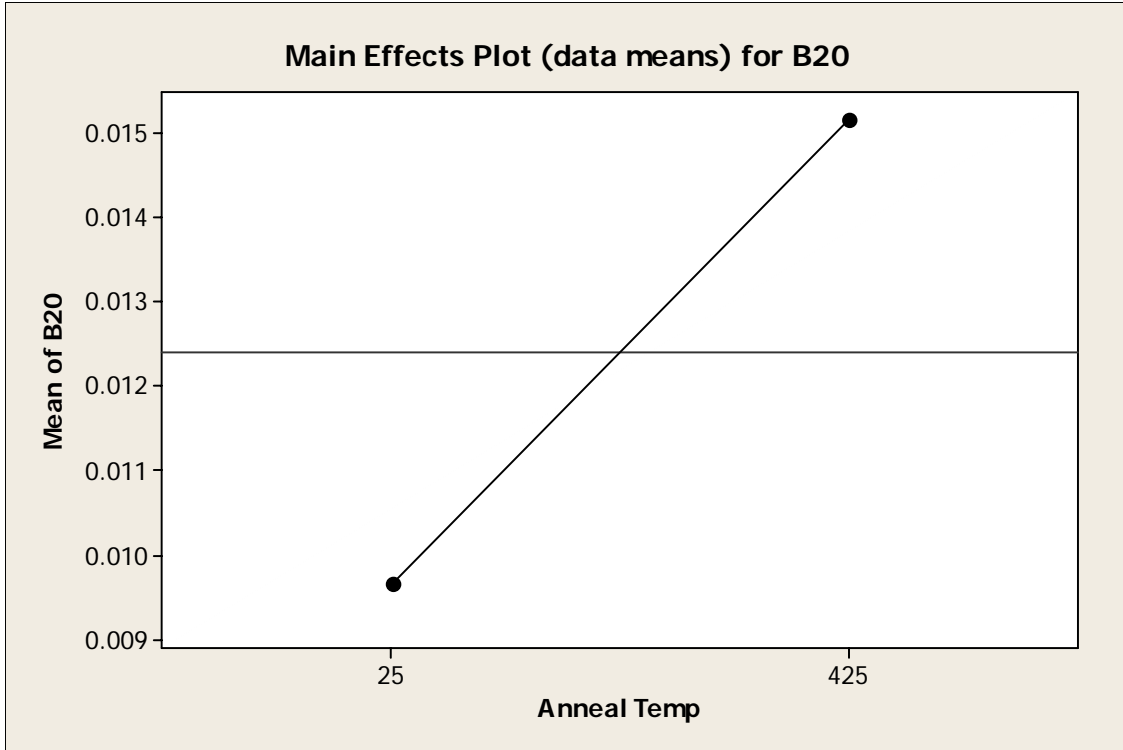


Figure 4.20 Effect of post-deposition annealing on B_{20} for ZnS:ErF₃ ACTFELDs.

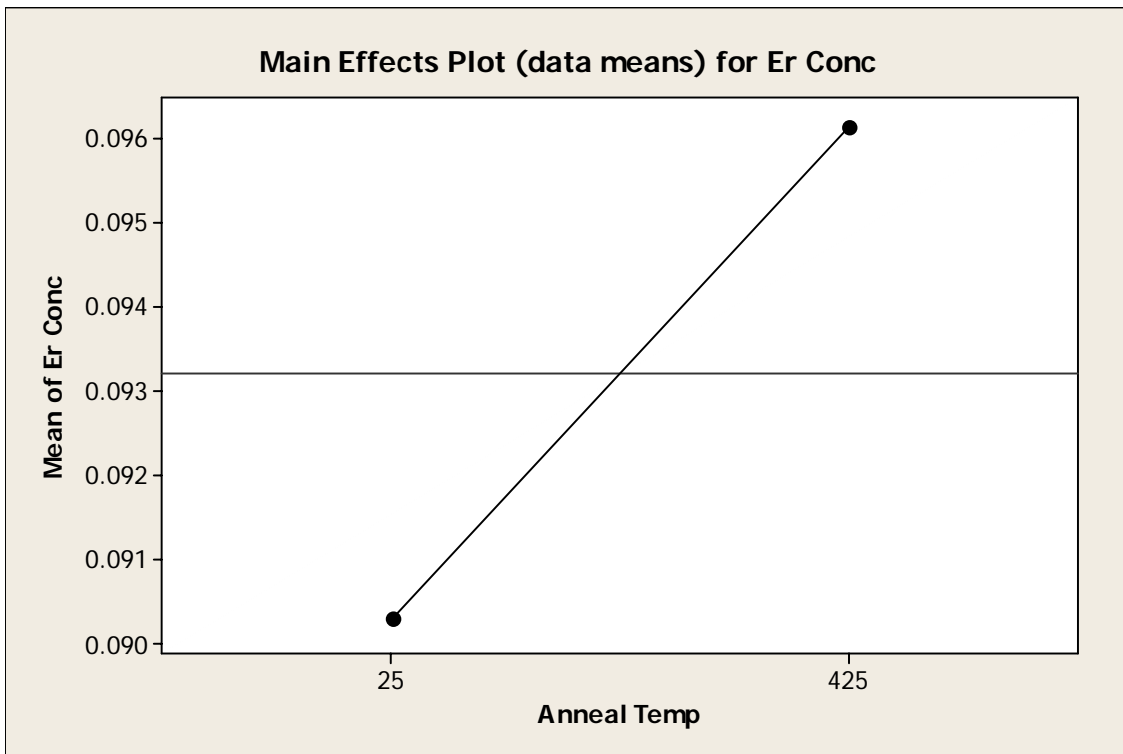


Figure 4.21 Effect of post-deposition annealing on Er/Zn ratio for ZnS:ErF₃ phosphors.

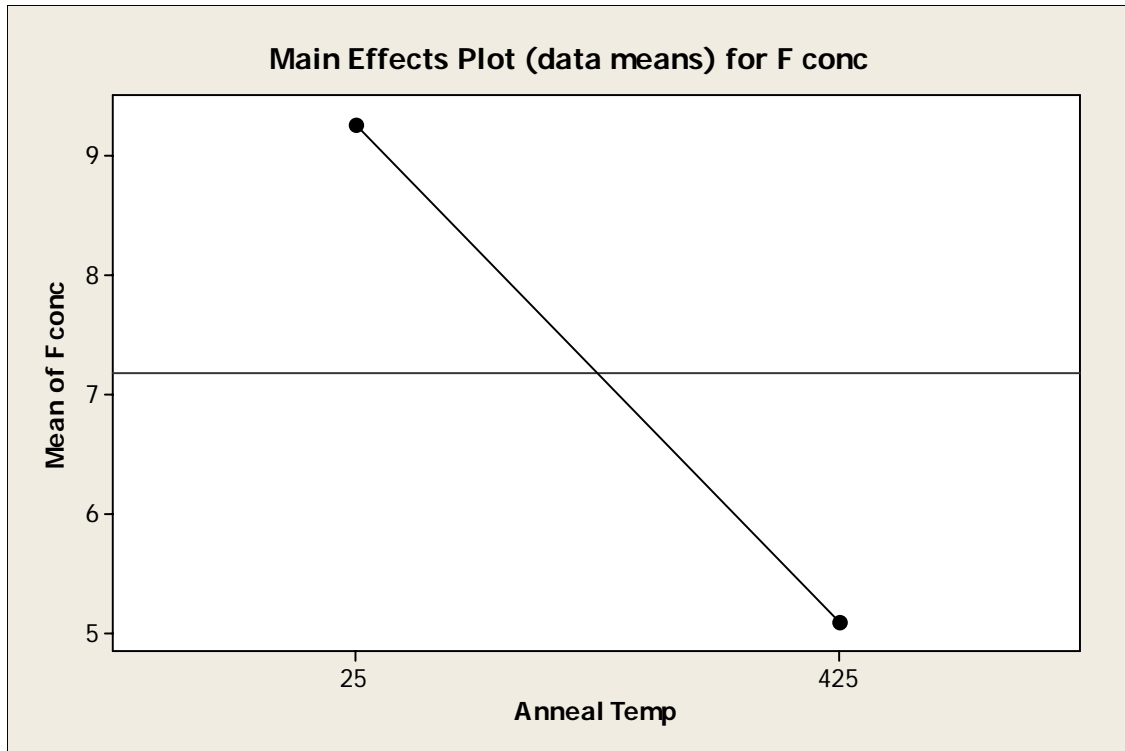


Figure 4.22 Effect of post-deposition annealing on F concentration [cm^{-3}] for ZnS:ErF₃ phosphors.

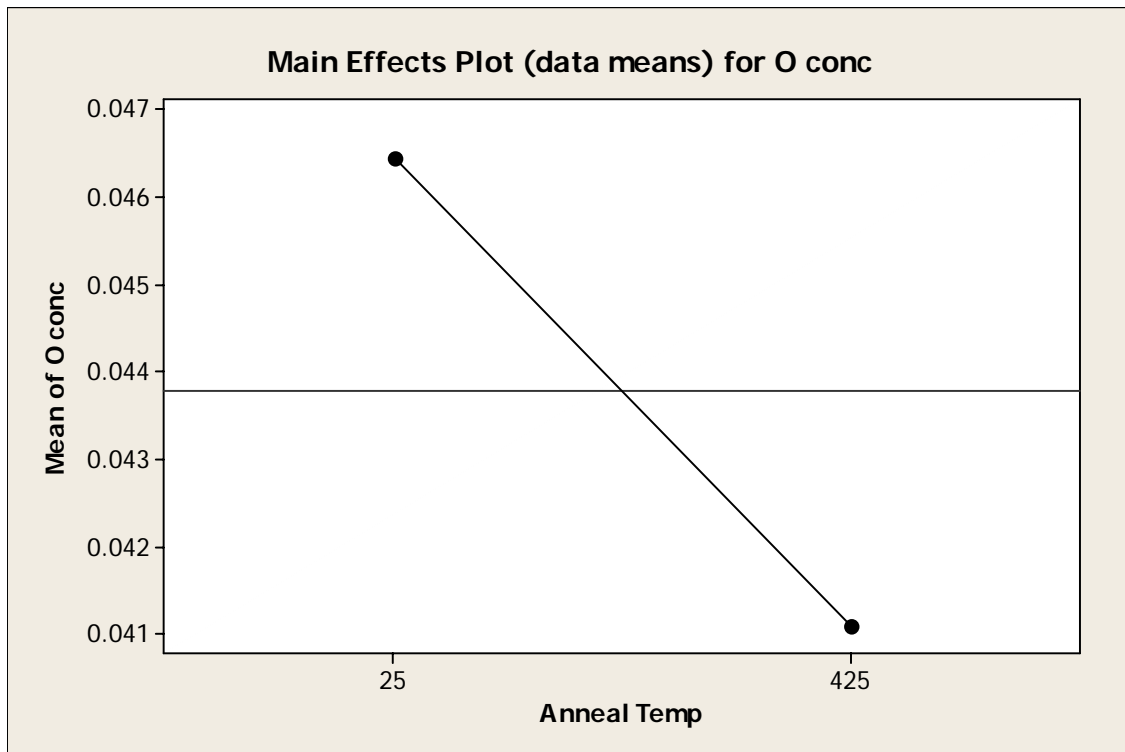


Figure 4.23 Effect of post-deposition annealing on O/ZnS ratio for ZnS:ErF₃ phosphors.

4.4 Discussion

In order to analyze the statistical significance of changes in the experimental data with changes in experimental parameters, an appropriate confidence level must be established. This confidence level is attributed to the level of confidence that the true value is within the range of data presented. Typically the confidence level is chosen as 95%, that is, there is a 95% certainty that the true value of the data lies within the range of values presented. For the data sets presented here a confidence level of 70% will be used. This confidence level is chosen based upon the fact that the film thickness varied by $\pm 15\%$ between samples, as well as recognition of the fact that small changes in device alignment during EL measurements led to errors in B_{20} estimated to be $\pm 20\%$. Additionally, SIMS analysis measurements exhibit errors within a range of $\pm 20\%$ as a result of sample charging and compositional variations across the sample, leading to an estimated error $([\sum x_i^2]^{1/2})$ of $\pm 30\%$.

P-values are used in the analysis of variance of the data to indicate which effects are statistically significant. P-values are the calculation of the probability that the value of the test data, or something more extreme, may be observed assuming that the parameter will have an effect on the data [105]. The α -level selected for the design-of-experiments (DOE) is expressed in Equation 5.1. The p-value is compared to the α -level, and if $p \leq \alpha$, the effect is statistically significant. If, however $p > \alpha$, the

$$\alpha\text{-level} = 1.00 - \text{confidence level} \quad (5.1)$$

effect is not significant. The p-values for each processing parameter's effect on E_r and F concentration, V_{th} and B_{20} are tabulated in Table 4.2. The α -level for this DOE is 0.3.

Table 4.2 Comparison of P-values for processing parameters.

Parameter	Er conc	F conc	V_{th}	B₂₀
	P-values	P-values	P-values	P-values
Dep. Temp.	0.347	0.366	0.915	0.035
Duty Cycle	0.02	0.274	0.001	0.005
Pressure	0.027	0.82	0.915	0.141
Anneal Temp.	0.728	0.173	0.75	0.233

The experimental data show that changes of substrate deposition temperature, duty cycle, sputtering gas pressure and annealing all have an effect on electroluminescence intensity from ZnS:ErF₃, with duty cycle having the greatest effect (factor of six times brighter for 75% duty cycle). As reported above, the small changes in threshold voltage with deposition temperature, sputtering gas pressure and annealing temperature are not significant. Only duty cycle changes resulted in a significant increase in threshold voltage. Erbium concentration changed significantly with changes in duty cycle and pressure. Fluorine concentration showed a corollary change with increasing duty cycle and significant change resulted from post-deposition annealing.

The effects of a processing parameter is more easily seen when comparing all results together, as shown in Figure 4.24 with identical ordinate scales. Based on data in this figure, it is obvious that the effect of all processing parameters, other than duty cycle, on threshold voltage is negligible. The increase in threshold voltage with increasing duty cycle may be attributed to greater incorporation of erbium dopant into the film. The larger size of the erbium ion substituted onto a zinc ion lattice position results in greater distortion of the crystal lattice and poorer crystallinity, increasing the number of scattering events in which hot electrons may encounter before dopant ion excitation. As a result, higher threshold voltages are necessary to induce electroluminescence.

The effect that each processing parameter had on brightness at 20 V above threshold (B_{20}) was more apparent when plotted with a constant ordinate as illustrated in Figure 4.25. It is easily seen from this figure that increasing duty cycle on the doped target has the largest relative effect. The effect of all experimental parameters on the Er/Zn ratio is shown in Figure 4.26 with identical ordinate scales. In this figure it becomes apparent that the Er/Zn ratio is greatly increased with increasing duty cycle and greatly decreased with increasing sputtering gas pressure. Similarly, the effect of each processing parameter on fluorine concentration is shown in Figure 4.27 with identical ordinate scales. Increased duty cycle resulted in increased fluorine concentration, while post-deposition annealing temperature corresponded to decreased concentration. There was no statistically significant change with deposition temperature or pressure,

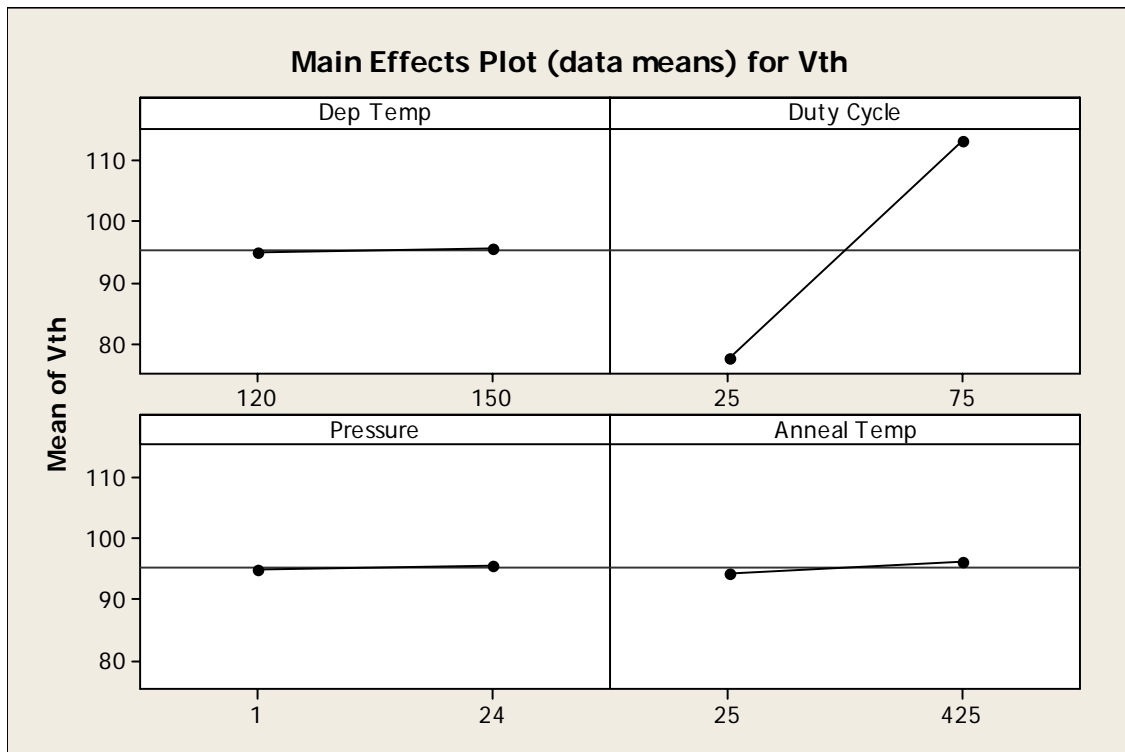


Figure 4.24 Effect of all experimental parameters on threshold voltage for ZnS:ErF₃ ACTFELDs.

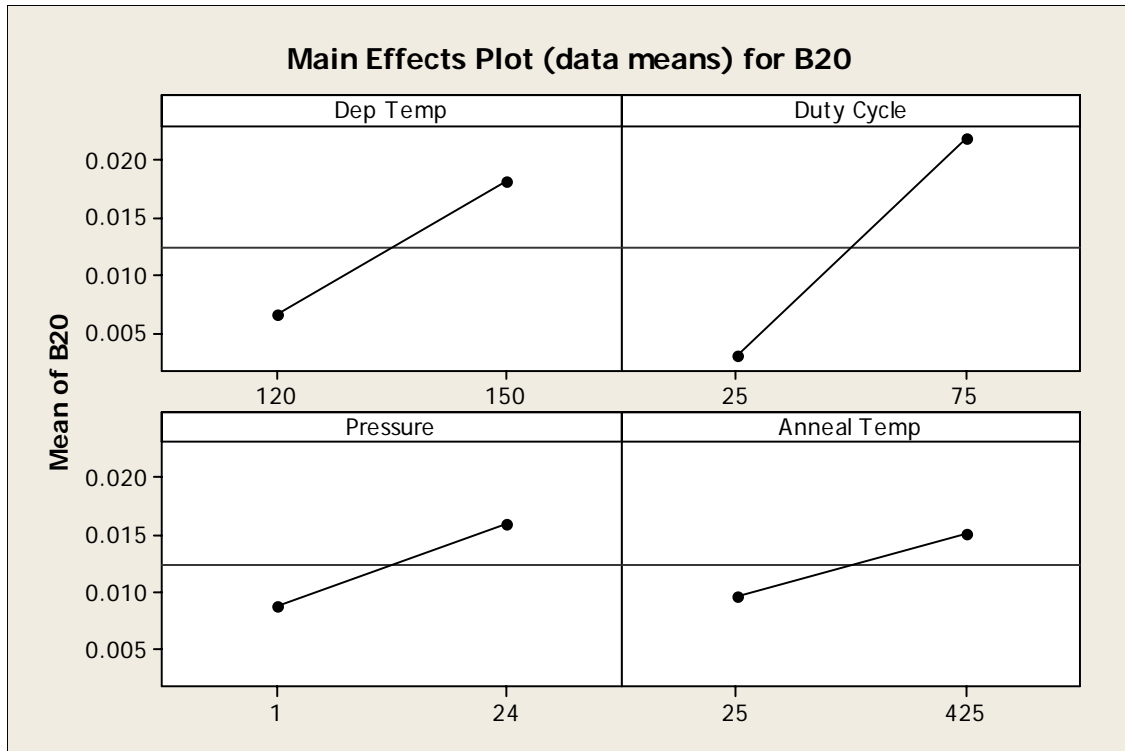


Figure 4.25 Effect of all experimental parameters on B₂₀ for ZnS:ErF₃ ACTFELDs.

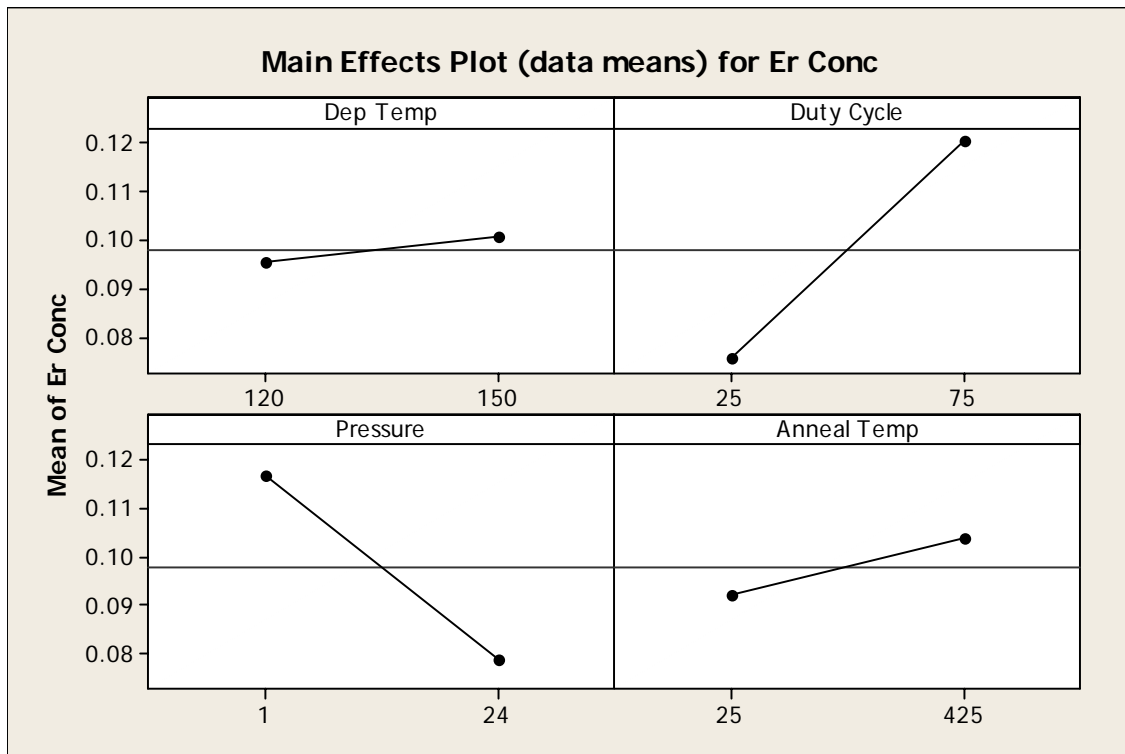


Figure 4.26 Effect of all parameters on Er/Zn ratio for ZnS:ErF₃ phosphor films.

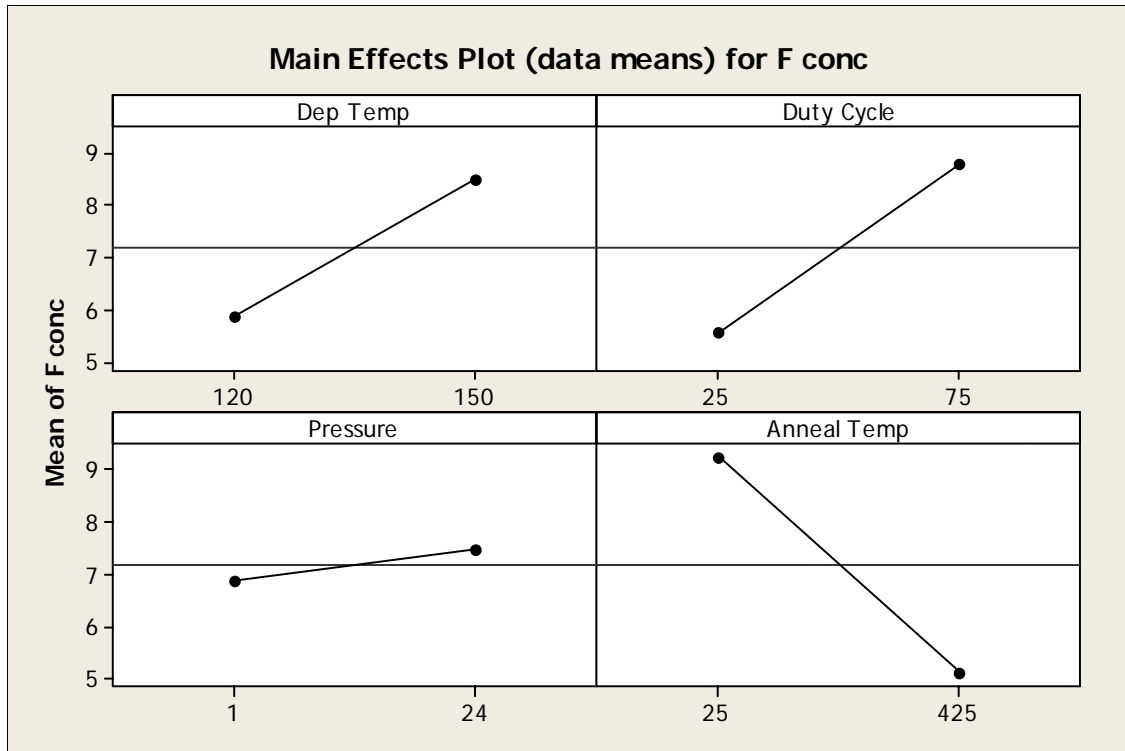


Figure 4.27 Effect of all parameters on F concentration [cm^{-3}] for ZnS:ErF_3 phosphor films.

Brightness increases by a factor of two as deposition temperature increases from 120°C to 150°C . At the higher deposition temperature, the Zn, S, Er and F present on the depositing film surface will have a greater surface mobility. As ions become incorporated into the lattice, they should sit on cation sites (Er^{3+} or Zn^{2+}) or anion sites (F^- or S^{2-}). Higher mobility will allow atomic species the ability to find appropriate lattice positions resulting in better bonding arrangements. In order to produce emission, erbium must be activated, by sitting on a cation lattice site. Higher surface mobility should result in a film with more activated luminescent centers and therefore higher luminescence.

At higher deposition temperatures, thermal desorption of Zn and S has been used to affect concentrations in $\text{ZnS}_x\text{Se}_{1-x}$ [106]. Thermal desorption is the result of a lower sticking coefficient for Zn and S at raised temperatures. If a constant deposition time is

used, thinner phosphor films will result. Little, if any thermal desorption of Zn and S occurred in these experimental depositions, based on the fact that a reduced Zn deposition rate would have altered the ratio of Er/Zn and shown a relative increase in Er concentration. The Er concentration remained relatively constant with changing deposition temperature, justifying the conclusion that thermal desorption did not significantly affect the films. The maintaining of a constant film thickness and the relatively low deposition temperatures used limited the amount of thermal desorption. While there is a slight increase in fluorine concentration with increasing deposition temperature it is not statistically significant based upon the p-value (0.366) in Table 4.2.

The increase in brightness with increasing duty cycle applied to the doped target is a factor of 6. As the percentage of time in which power is applied to the doped target increases, the number of dopant ions incorporated into the deposited film increases. This is consistent with the data that show that increasing the duty cycle from 25 to 75% resulted in an increase by 80% and 70% in the Er/Zn ratio and the F concentration, respectively. An increase in the number of erbium ions incorporated into the phosphor layer will result in an increase in the number of radiative events that may occur under applied voltage. As such the overall brightness of the device will increase with an increase in dopant concentration. At high dopant concentrations, there is the possibility of decreased brightness due to concentration quenching [107]. This has been attributed to interactions between neighboring luminescent centers leading to non-radiative relaxation through self-quenching. Once this threshold has been reached luminescence will decrease with increasing concentration.

Brightness increased by 80% with increasing argon sputtering gas pressure. This increase is attributed to a greater amount of negative ion resputtering at lower pressures [108]. During sputtering, Ar^+ ions are generated and accelerated towards the ZnS:ErF_3 target to cause sputtering and deposition of the phosphor film. However, if negative ions, e.g. O_x^- or S^- , are formed, they are accelerated towards the deposited film and may be sufficiently energetic to cause re-sputtering of the Zn, S and/or F. In addition, some of the negative ions may be neutralized in the sputter plasma after being accelerated to high energies, and these excited neutrals may also cause re-sputtering. However, at higher sputter gas pressure, the distance between the target and substrate may be greater than the ion/excited neutral molecular mean free path (i.e. the distance traveled before an inelastic collision between the ion/neutral and an Ar atom). In an inelastic collision, the energy of the ion/neutral may be reduced below that necessary for sputtering. Therefore it is reasonable that as the Ar gas pressure and therefore gas density increases, the number of inelastic collisions between negative ions, energetic neutrals and argon increase, causing the ions and excited neutrals to lose energy. At lower pressures, negative ions and energetic neutrals are thus better able to maintain sufficiently high energies to cause re-sputtering of the Zn and S atoms in the deposited film.

As the sputtering gas pressure increases from 1 mTorr to 24 mTorr, little change occurs in the fluorine concentration, while a large decrease (~40%) occurs in the Er concentration, i.e. the Er/Zn ratio, as shown in Table 4.2. This may be understood by recognizing that zinc and sulfur are more closely matched in mass with O_x^- and S^- than is erbium, resulting in a larger fraction of transferred energy to Zn and S. As a result, Zn and S exhibit a larger negative ion sputter yield than does Er, leading to Er enrichment in

the film deposited at low Ar pressure. Re-sputtering of the deposited surface would also result in damage to the crystal structure, limiting the ability of Er to find cation sites on which to activate. While there are a greater number of luminescent centers in the film there is greater film damage and limited activation of Er ions at 1mTorr pressure. This effect would also lead to lower luminescence at lower gas pressures. Given adequate time and energy, there will be diffusion of Zn and S constituents through the film to provide some healing of the damage.

Annealing phosphor films at 425°C for 1 hour resulted in an increase of 60% in brightness. A significant increase of brightness upon post-deposition annealing has been reported in the literature [99]. Hsu *et al.* [86] reports that annealing at temperatures 300°C will reduce the concentration of fluorine in ZnS:TbF₃ ACTFELDs. Hsu *et al.* attributed this effect of annealing upon brightness to a reduction in fluorine concentration in the film and improved film crystallinity. This corresponds well to the observed reduction in F concentration of ~40%. The nearest neighbors to Er are F as shown in X-ray absorption fine structure spectroscopy (XAFS) measurements [109]. Fluorine ions are substituted onto the sulfur lattice positions nearest the zinc lattice sites on which erbium sit. This occurs because both the F and Er prefer a more ionic bond than the covalently natured bonds that are formed with Zn and S, respectively. As films are annealed, the fluorine ions incorporated into the crystal for charge balance are reduced. This alters the local crystal field around the erbium luminescent centers. The change in local crystal field allows for more radiative oscillator strength for the near infrared luminescent transitions.

No increase in erbium concentration is observed for samples annealed at 425°C as compared to as-deposited samples. While there is a slight increase in the average Er/Zn

ratio after annealing (Figure 4.26), the change is well within the experimental error estimated to be $\pm 15\%$. The fact that post-deposition annealing has no appreciable effect on the concentration of erbium in the ZnS film suggests that erbium does not diffuse out of the film into the underlying ATO layer. Additionally no significant change in the O/ZnS ratio resulted from annealing. This indicates that oxygen is not substituting fluorine in the lattice nor replacing sulfur during annealing.

As this study involved the statistical analysis of multiple experiments simultaneously, it is important to verify that no systematic errors occurred during the analysis. Normal probability plots for the threshold voltage and brightness data are shown in Figures 4.28 and 4.29, respectively. The probability plots to evaluate for systematic errors in the Er/Zn ratio and F concentration are shown in Figures 4.30 and 4.31, respectively. These plots help to illustrate whether the data are normally distributed, whether other variables are influencing the response and whether outliers exist in the data. If the data did not lie along a straight line this would signal that the data deviated from a normal distribution. A point far away from the line would indicate an outlier which may be a result of data collection or data entry errors. A changing slope would indicate an unidentified variable. For data sets incorporating fewer than 50 observations, such as this one, some curvature of the tails may result even though the data are normally distributed. As can be seen from these figures, the data fall close to a normal distribution with no apparent influence from unknown variables or data outliers. As such, the data appear to be statistically sound.

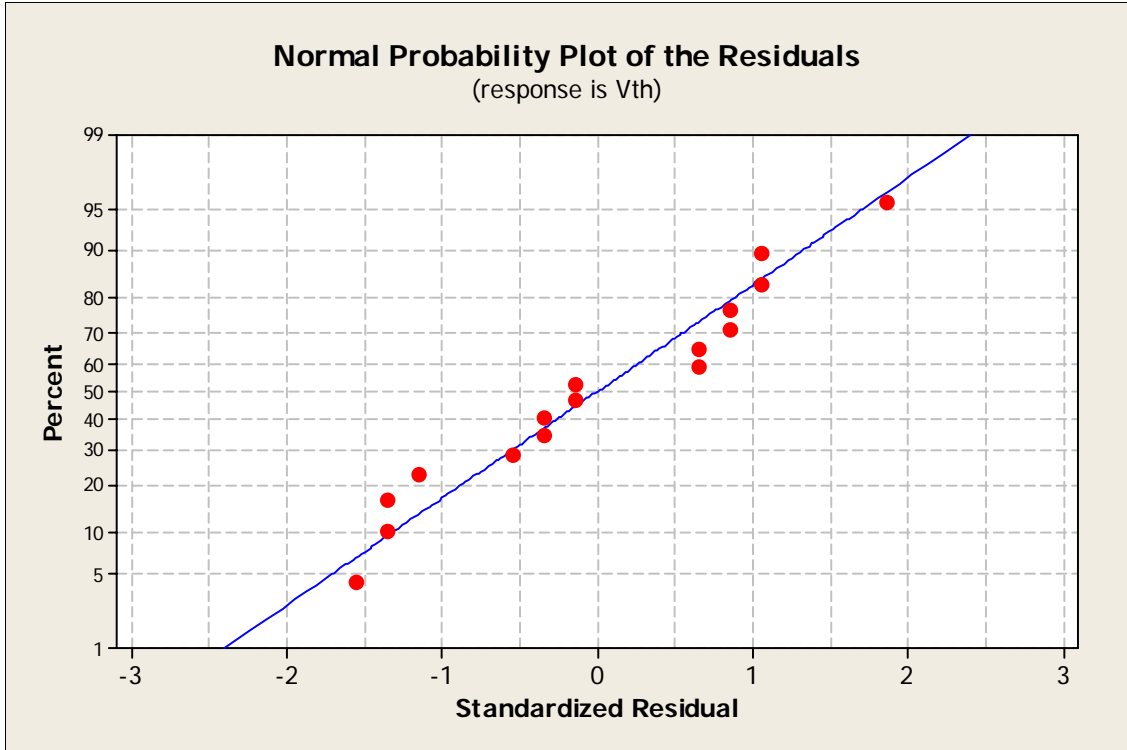


Figure 4.28 Normal probability plot of threshold voltage data values.

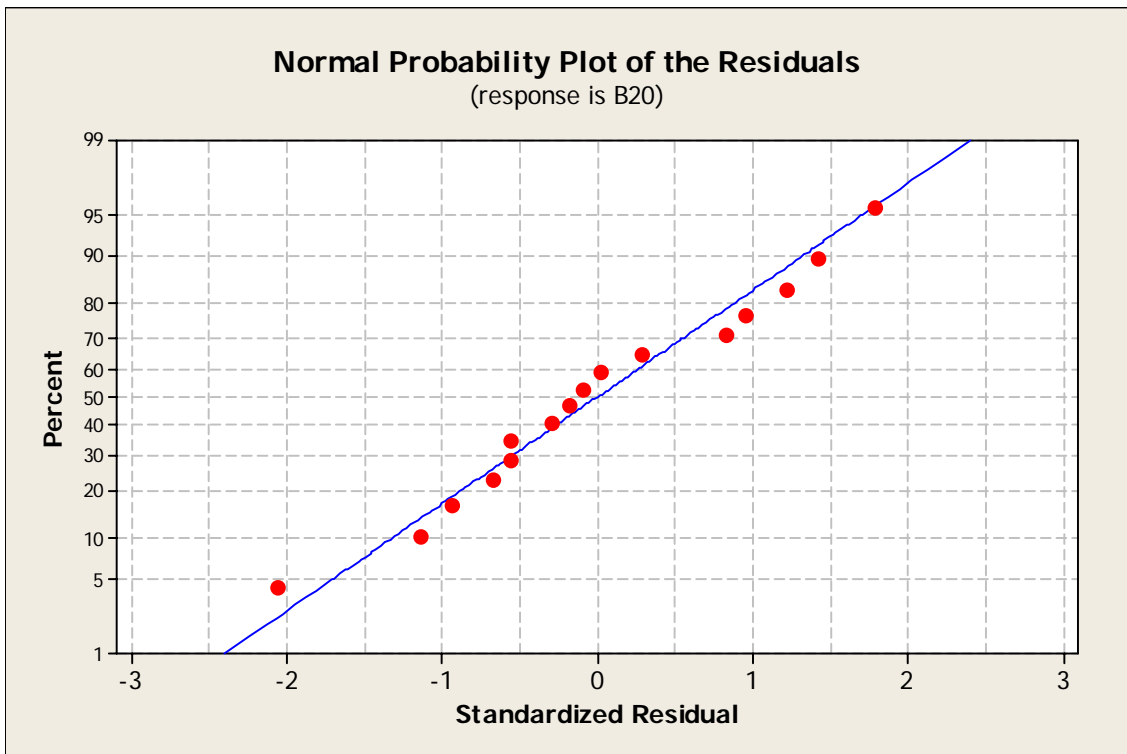


Figure 4.29 Normal probability plot of B₂₀ data values.

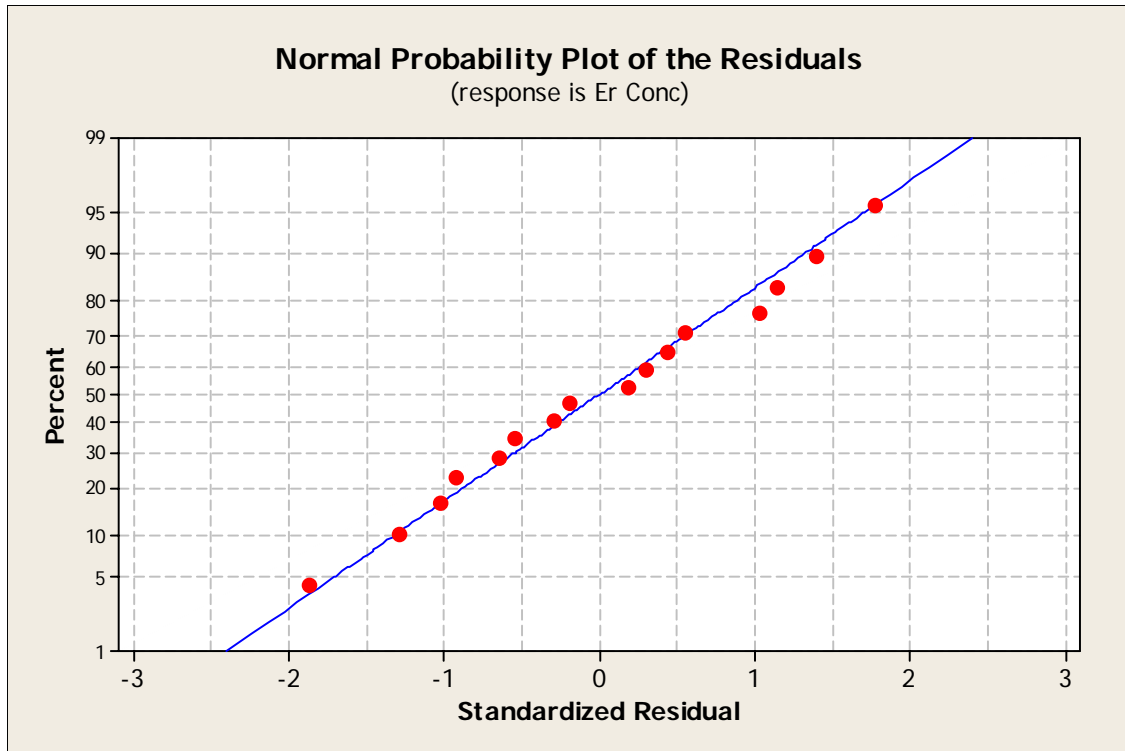


Figure 4.30 Normal probability plot of Er/Zn ratio values.

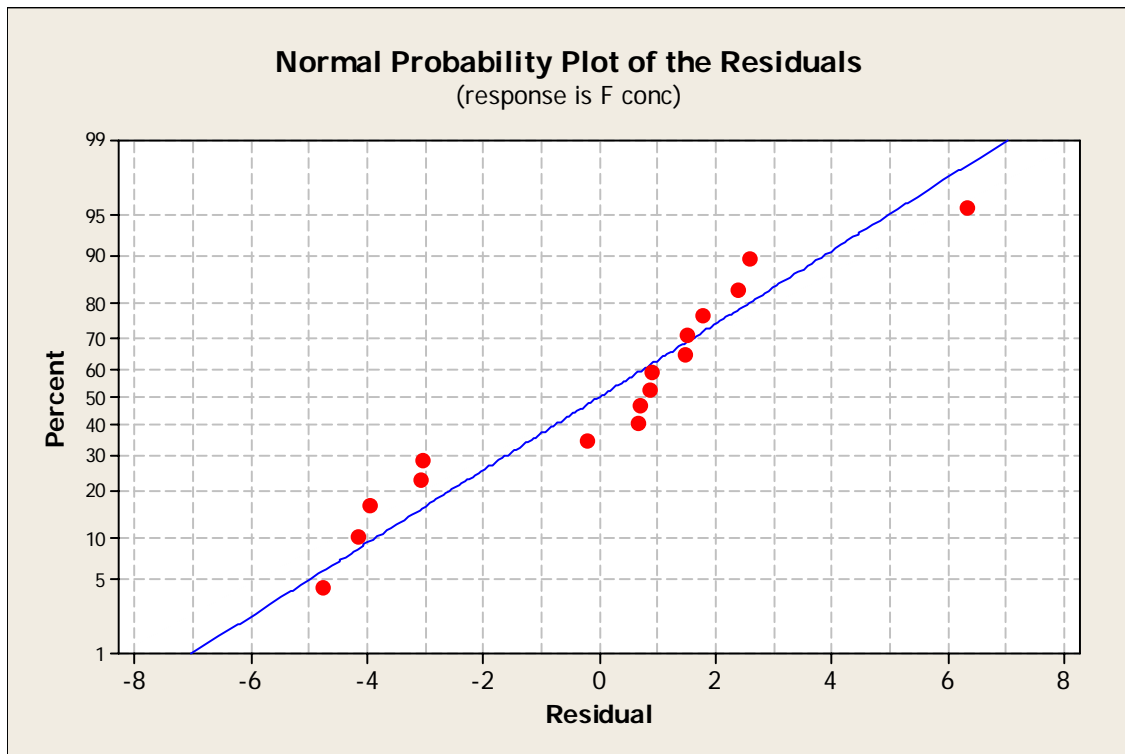


Figure 4.31 Normal probability plot of F concentration values.

Also of importance is an evaluation of any effects of the order of data collection on the data itself. The plot of residual versus order of collection of the data for threshold voltage and B_{20} are shown in Figures 4.32 and 4.33, respectively. The plots of residual versus order of collection of the data for Er/Zn ratios and F concentration are shown in Figures 4.34 and 4.35, respectively. Residuals are the differences between the observed values for the response and the predicted values [110]. Such data plots indicate whether there are systematic effects in the data due to when the data are collected or in which order they are collected. Systematic effects would be suggested by an ascending or descending trend, or by rapid changes in signs of adjacent residuals. These data show no apparent trends in which either threshold voltage, B_{20} , Er/Zn ratio or F concentration were affected by the order in which experiments were performed or when data were collected.

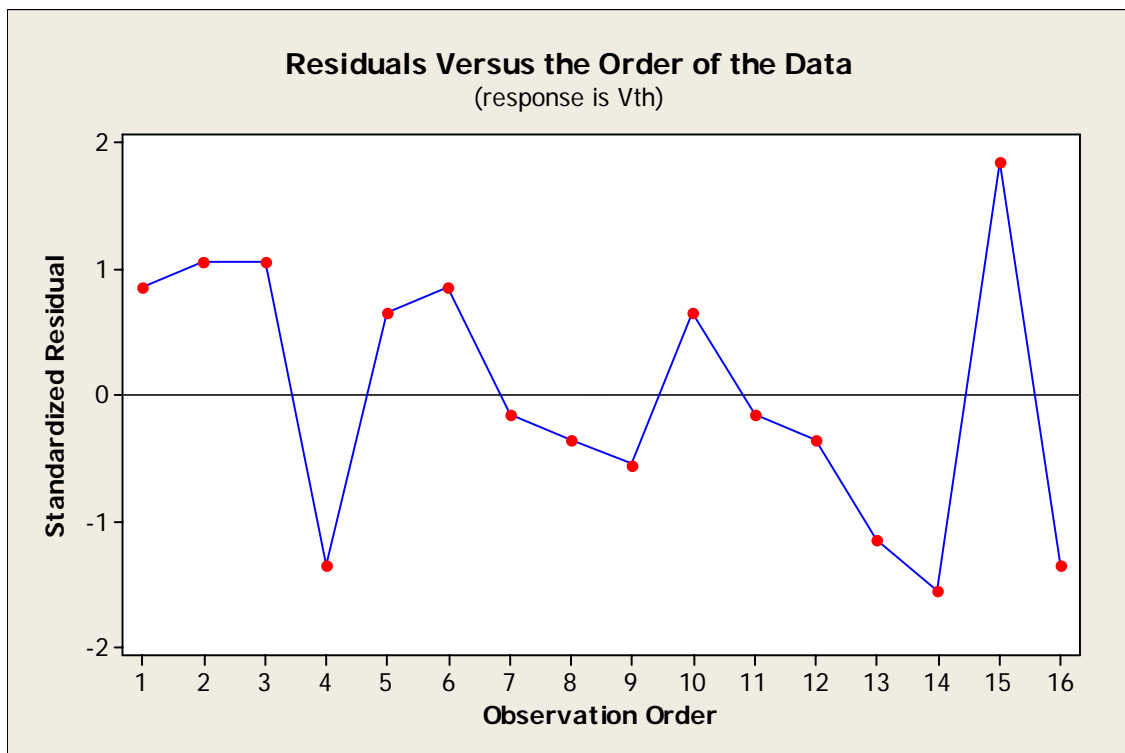


Figure 4.32 Effect of order of data collection on threshold voltage data values.

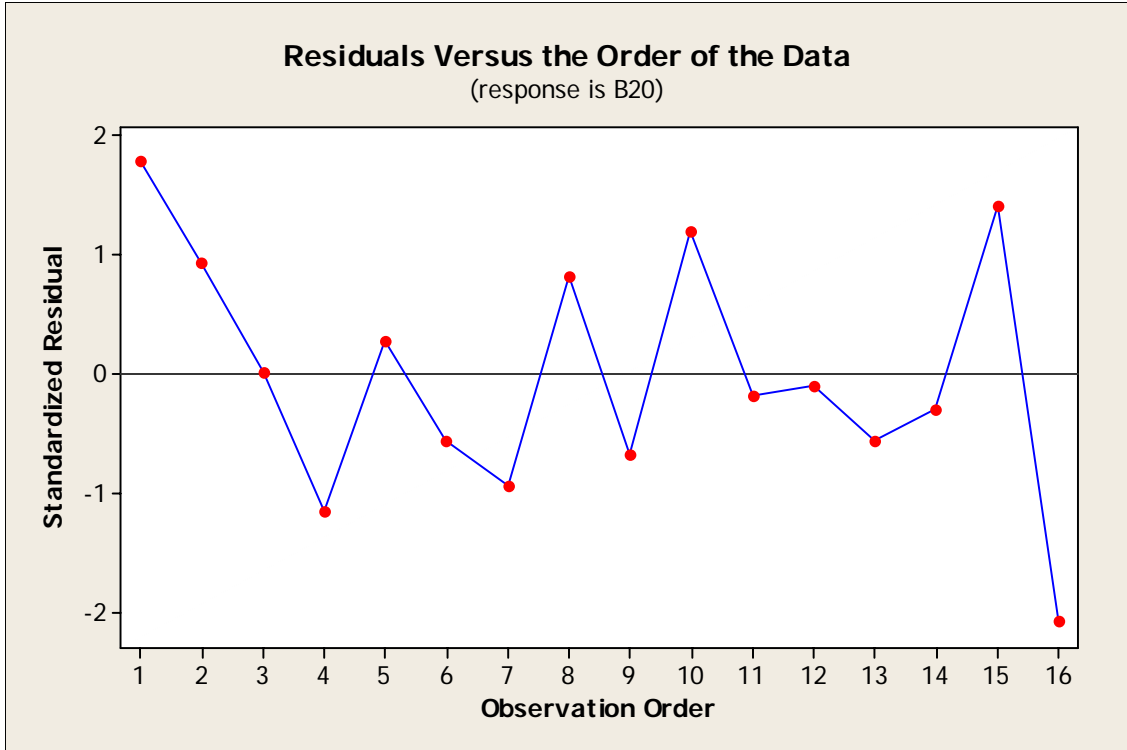


Figure 4.33 Effect of order of data collection on B₂₀ data values.

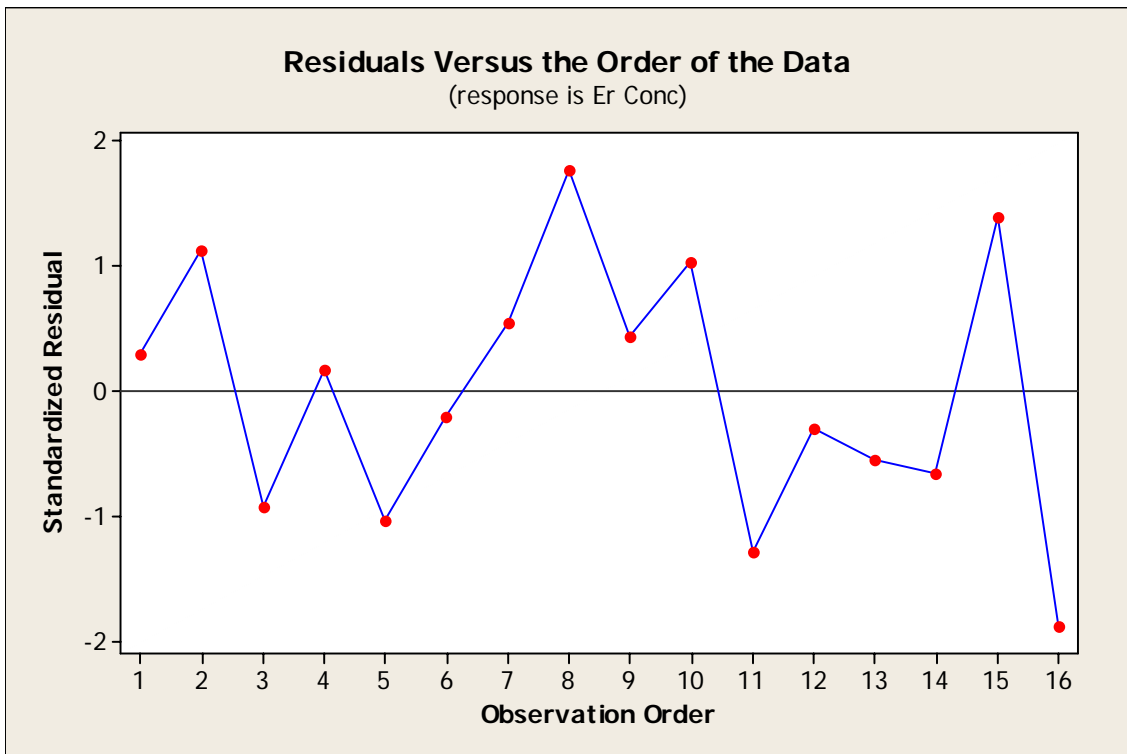


Figure 4.34 Effect of order of data collection on Er/Zn ratio values.

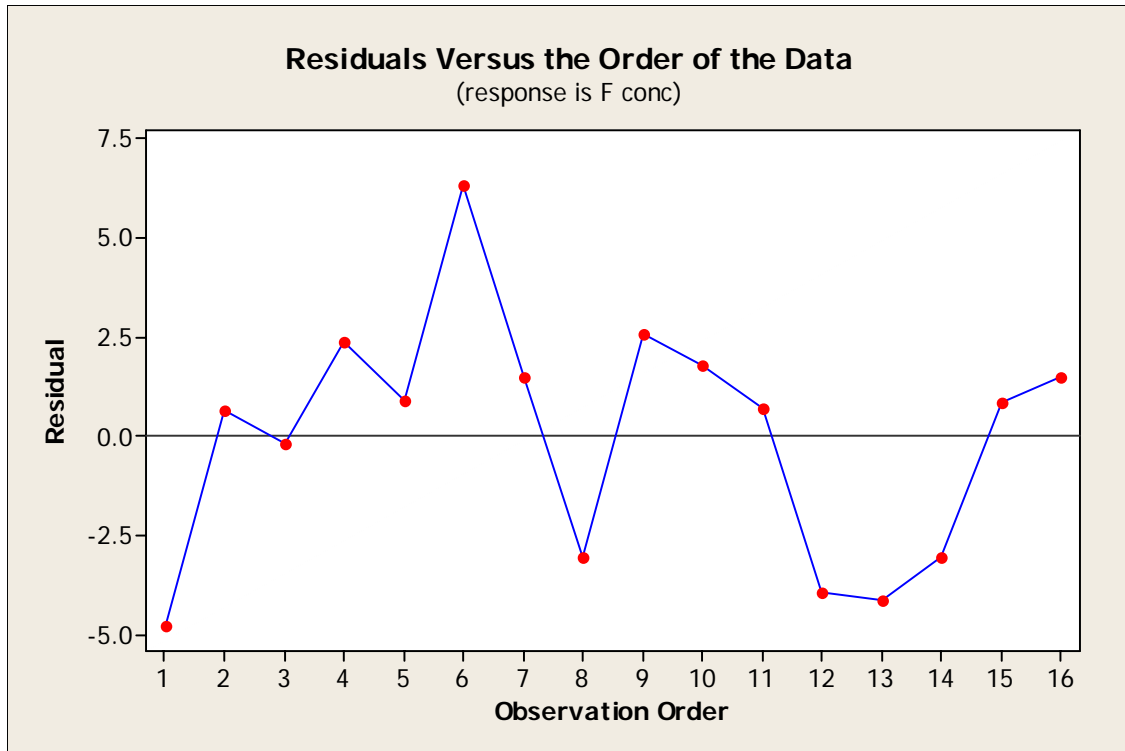


Figure 4.35 Effect of order of data collection on F concentration values.

4.5 Summary

In this study, ZnS:ErF₃ films were deposited under a number of different processing conditions. Deposition temperature was varied between 120°C and 150°C. Duty cycle on the doped target was varied between 25% and 75%. The duty cycle on the undoped target was maintained at 100% and power applied to both targets at a 100% duty cycle was kept at 100 W. The pressure of the argon sputtering gas was varied between 1 mTorr and 24 mTorr. After deposition of the phosphor layer, half of the samples produced were annealed in nitrogen ambient for 1 hour at 425°C. Statistical analysis of data showed no statistically significant effect on threshold voltages for changes to deposition temperature, sputtering gas pressure and annealing temperature. Increase in the duty cycle resulted in an increase in threshold voltage from 77.5 V at 25% to 113 V at 75%. The near infrared (1550 nm) electroluminescence emission intensity from Er

showed a more pronounced effect as a result of changes in processing conditions. Increases in substrate deposition temperature resulted in an increase in B_{20} by approximately 180%, which is attributed to better dopant activation in the phosphor. Increasing deposition temperature had a negligible effect on the Er and F concentrations. The Er and F concentration increased by ~80% and ~70%, respectively, with an increase in duty cycle. Increasing of the duty cycle also showed the greatest effect on brightness, an increase of a factor of six. This is attributed to a greater amount of dopant incorporated into the phosphor layer with increasing duty cycle. Sputtering gas pressure showed increase of 80% in B_{20} with increasing pressure. An increase of the argon sputter gas pressure increase resulted in a ~40% decrease in Er concentration but no significant change in the F concentration. This was attributed to the effects of gas pressure on the energy of negative ions and energetic neutrals. At lower sputter gas pressures, ions and energetic neutrals lose less kinetic energy from particle-particle collisions. As a result they are able to strike the surface causing resputtering of the Zn, S and F constituents. These effects result in an increased concentration of Er in the film. Post-deposition annealing did not cause the Er concentration to change, but did cause a ~40% decrease in the F concentration of the film. This is attributed to fluorine diffusing through the film to the surface and desorbing. The effect of fluorine reduction, through annealing, resulted in an increase of ~60% in device brightness. The optimum device was produced using a deposition temperature of 150°C, a duty cycle of 75%, an argon sputtering gas pressure of 24 mTorr and post-deposition annealing at 425°C for 1 hour in UHP N_2 . This resulted in 1550 nm emission of $146.5 \mu W/cm^2$, at 20 V above threshold. Analysis of the data for all effects showed a normal distribution with no outliers and no effect resulting from the

order of data collection. These facts support the conclusion that the data are statistically valid.

CHAPTER 5 EFFECTS OF PROCESSING PARAMETER INTERACTIONS ON ELECTROLUMINESCENCE AND CHEMICAL COMPOSITION

5.1 Introduction

The effects of parameters used during radio frequency (RF) magnetron sputter deposition as well as during post-deposition annealing on the electroluminescence and chemical composition of ZnS:ErF₃ ACTFEL devices were described in Chapter 4. The interactions of processing parameters on the resulting electroluminescence and chemical composition of ZnS:ErF₃ phosphors are reported and discussed in this chapter.

5.2 Experimental Procedure

Thin films of ZnS:ErF₃ were RF magnetron sputter deposited onto standard glass/ITO/ATO substrates. The process flow for device fabrication was shown previously in Figure 4.4. The device structure used is the “half-stack” structure described in Section 2.3 with the exception that the opaque top electrode is not deposited on the phosphor layer to allow for easier chemical analysis.

5.2.1 Substrate

Substrates consist of Corning 7059 glass, 0.04 inches thick, coated with 360 nm of polycrystalline indium tin oxide (ITO) (90 wt% In₂O₃ + 10 wt% Sn₂O₃) as the transparent conducting electrode and 160 nm of amorphous aluminum titanium oxide (ATO) (Al₂O₃ / TiO₂) as the bottom insulating layer. These coated substrates were supplied by Planar Systems. Additional substrates of bare Corning 7059 glass were prepared for use in measurement of the thickness of the ZnS:Er films.

Table 5.1 Processing parameters for ZnS:ErF₃ phosphors.

Dep T (°C)	Duty Cycle	Pressure (mTorr)	Anneal (°C)
120	25	1	25
120	25	1	425
120	25	24	425
120	25	24	25
120	75	24	25
120	75	24	425
120	75	1	425
120	75	1	25
150	75	1	25
150	75	1	425
150	75	24	425
150	75	24	25
150	25	24	25
150	25	24	425
150	25	1	425
150	25	1	25

5.2.2 Phosphor Layer Deposition

As described in Section 4.2, the ZnS:ErF₃ phosphor layer is deposited by two independently controlled RF magnetron sputter guns. One sputter gun contains a CVD grown polycrystalline pure ZnS target source purchased from Morton Thiokol, Inc. The other sputter gun uses a ZnS:1.5 wt% ErF₃ compound target purchased from SCI Engineering Materials. The deposition chamber is evacuated to a base pressure between 6.5×10^{-7} and 1×10^{-6} Torr prior to phosphor deposition. Argon is used as the sputter gas and is introduced into the chamber using Unit UFC 1100A 20, 50 or 100 sccm mass flow controllers on three inlet lines. The Ar pressure was kept at either 1 mTorr or 24 mTorr as described in Table 5.1. The power applied to both the targets was 100 W for all samples, but the duty cycle for the doped target was varied between 25% or 75%. During deposition, the substrates are heated by carbon cloth resistors to either 120°C or 150°C. Following phosphor layer deposition, a portion of the devices were annealed in a quartz

tube with an ultra high purity nitrogen (99.9999%) ambient at 425°C for 60 minutes prior to deposition of the opaque electrode. Samples not annealed are noted to have been ‘annealed’ at room temperature (25°C).

5.2.3 Chemical Composition Analysis

As previously described in Section 4.4, the chemical constituents of the film were characterized using secondary ion mass spectroscopy (SIMS) [101] and by energy dispersion spectroscopy (EDS) on the scanning electron microscope (SEM) [102]. SIMS is a quantitative characterization technique that provides a high element sensitivity and excellent depth resolution. A beam of primary ions is used to sputter the sample surface as described in Section 4.2.4.

5.3 Effects of Processing Parameter Interactions

While each processing parameter may act independently on chemical composition and electroluminescence, parameters may act in concert to alter properties as well. To determine which interactions are significant, a comparison of p-values to the α -level is used as in Section 4.4. To avoid discussion of a large number of insignificant interactions, only those interactions which are statistically significant will be described.

5.3.1 Effects on Erbium Concentration

The most important parameters effecting Er concentration are duty cycle and deposition pressure as described in Section 4.4. The interaction of these two processing parameters is also statistically significant. Figure 5.1 shows the interaction of duty cycle and deposition pressure in two panels. An interaction is indicated by different trends when both parameters are varied. The graph displays the Er concentration, as the ratio of Er-to-Zn SIMS peak intensities from the phosphor film, on the left, bottom and right, top of the graphs. The values for sputtering gas pressure and duty cycle are displayed on the

top-right and bottom-left, respectively, with the second parameter being designated by the color symbol in the legend box. In this case, the top right box shows that the Er concentration decreases when the Ar pressure increases from 1 to 24 mTorr, but the effect is greater from a 75% duty cycle than at a 25% duty cycle. Similarly, the bottom right box shows that the erbium concentration is higher at 1 mTorr for a duty cycle of

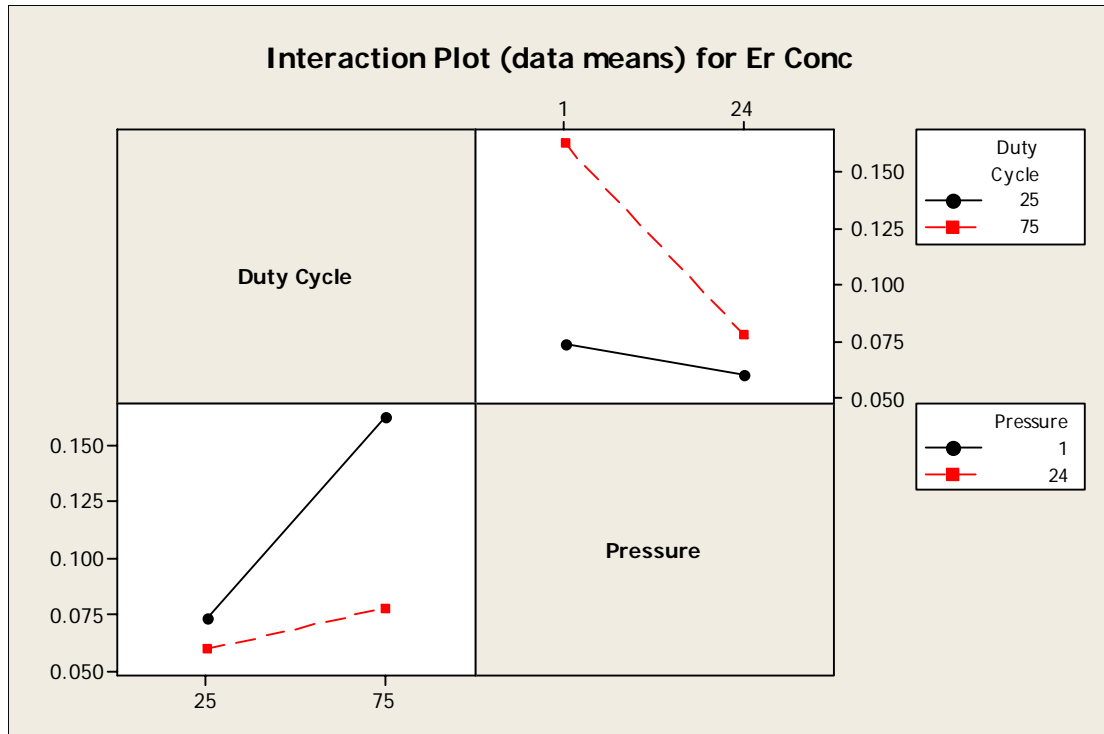


Figure 5.1 Effect of interaction of duty cycle (25 and 75%) and Ar gas pressure (1 and 24 mTorr) on Er concentration.

either 25 or 75% versus the concentration at 24 mTorr. In addition, the Er concentration remains higher at 75% versus 25% duty cycle regardless of pressure.

5.3.2 Effects on Fluorine concentration

As reported in Chapter 4, the processing parameters with the greatest effects on F concentration were duty cycle and annealing temperature. Interactions of other parameters with duty cycle or annealing temperature were statistically insignificant based on $p < \alpha = 0.3$, as discussed and summarized below. However the fluorine concentration

was strongly affected by the interaction of deposition temperature and sputtering gas pressure as shown in Figure 5.2

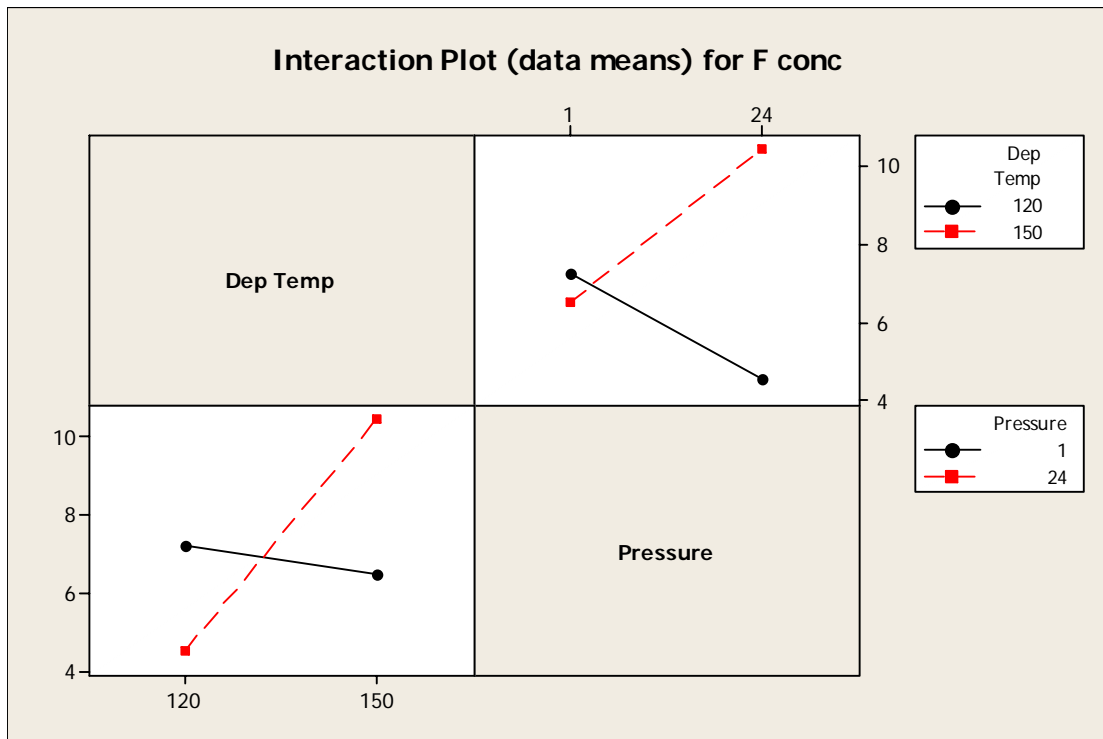


Figure 5.2 Effect of interaction of deposition temperature (120 and 150°C) and Ar gas pressure (1 and 24 mTorr) on F concentration.

With increasing deposition temperature, there is a decrease in F concentration of ~10% at 1 mTorr. However at 24 mTorr, there is an increase in F concentration of ~130% with increasing deposition temperature.

5.3.4 Effects on Threshold Voltage

The processing parameter with the greatest effect on threshold voltage (V_{th}) is duty cycle. No significant effects from interactions of duty cycle with other parameters were observed for V_{th} . However the interaction of deposition temperature and sputtering gas pressure was statistically significant for V_{th} , as shown in Figure 5.3.

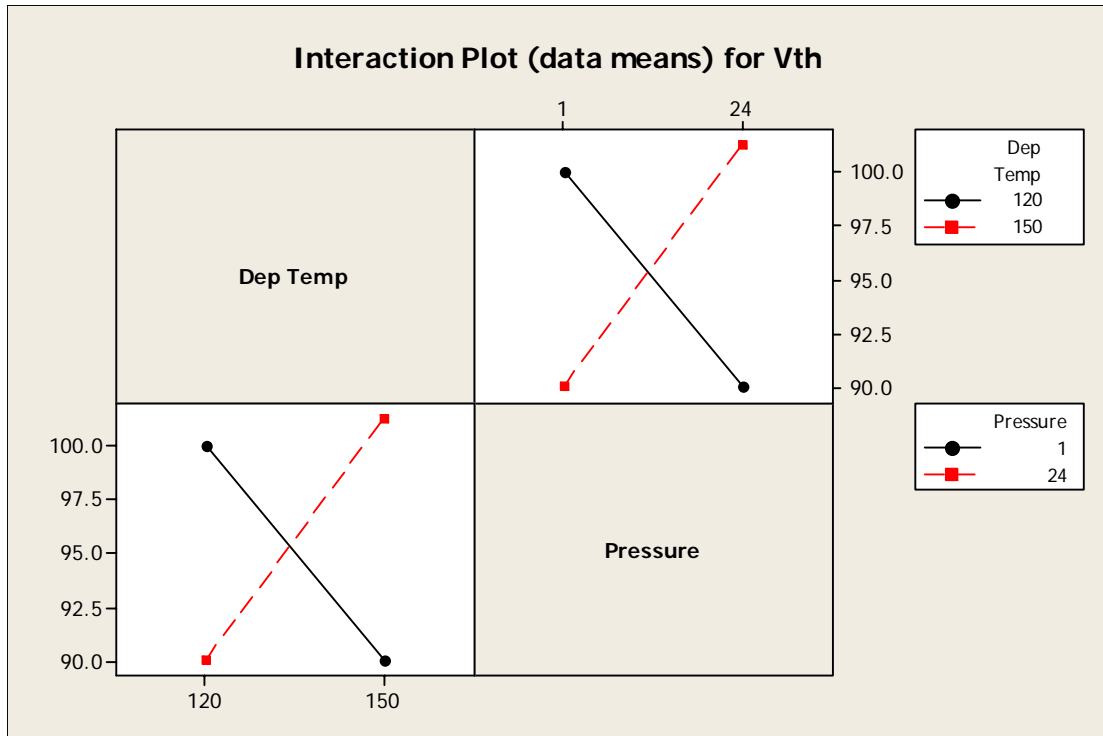


Figure 5.3 Effect of interaction of deposition temperature (120 and 150°C) and Ar gas pressure (1 and 24 mTorr) on V_{th} .

At a deposition temperature of 120°C, the mean V_{th} at 1 mTorr is larger at 100 V versus 24 mTorr at 90 V, a 10% decrease. At a deposition temperature of 150°C, the effect is opposite with V_{th} at 1 mTorr smaller at 90 V and larger at 24 mTorr (101 V), a 12% increase.

5.3.4 Effects on Electroluminescent Brightness

All processing parameters were reported in Chapter 4 to have a statistically significant effect on brightness at 20 V above threshold (B_{20}). However, not all parameters interacted with one another. Significant interactions were observed for deposition temperature with duty cycle, deposition temperature with sputtering gas pressure, and of duty cycle with sputtering gas pressure.

The interaction of deposition temperature with duty cycle is shown in Figure 5.4. As the duty cycle on the doped target is increased from 25% to 75%, the brightness

increases from 0.0027 to 0.0104 (arbitrary units) at 120°C ($\Delta \sim 290\%$) and from 0.0031 to 0.0333 at 150°C ($\Delta \sim 960\%$). The interaction of deposition temperature and sputtering gas pressure is shown in Figure 5.5. As the Ar sputtering gas pressure is increased from 1 mTorr to 24 mTorr, the brightness increased from 0.0059 to 0.0073 ($\sim 20\%$) at 120°C and from 0.0118 to 0.0247 ($\sim 110\%$) at 150°C. The interaction of duty cycle and pressure is shown in Figure 5.6. At a duty cycle of 25%, the brightness decreased from 0.0035 at 1 mTorr to 0.0023 at 24 mTorr ($\sim 34\%$). At a duty cycle of 75%, the brightness increased from 0.0142 at 1 mTorr to 0.0296 at 24 mTorr ($\sim 110\%$).

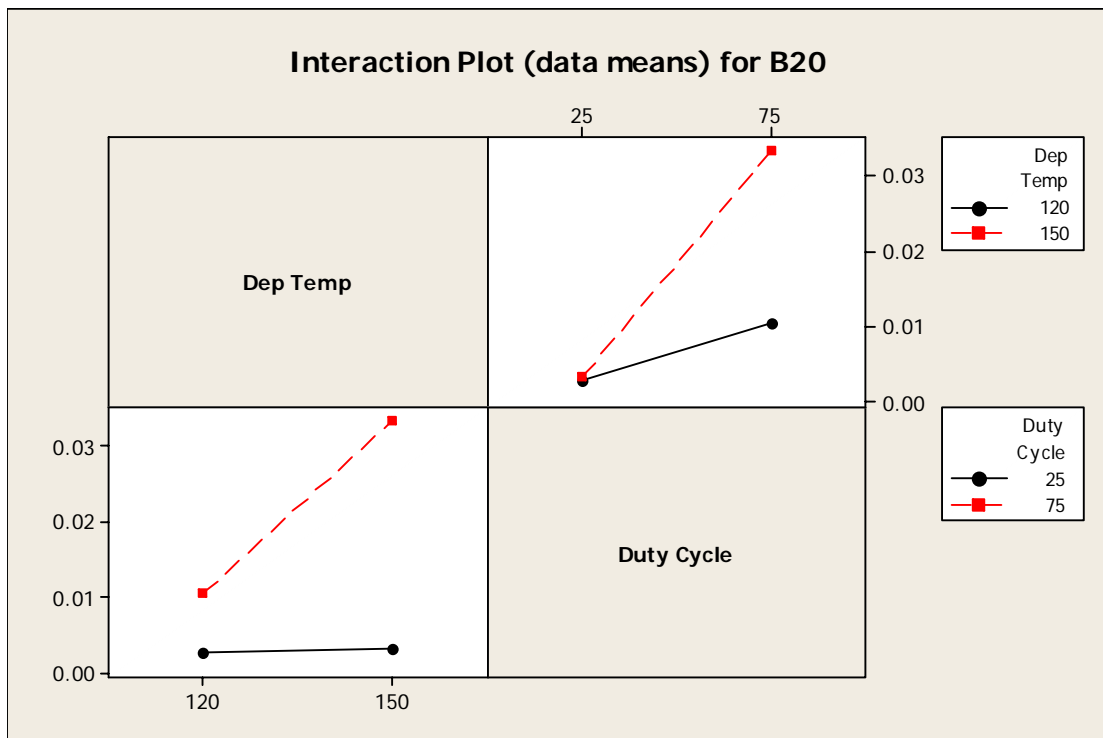


Figure 5.4 Effect of interaction of deposition temperature (120 and 150°C) and duty cycle (25 and 75%) on B₂₀.

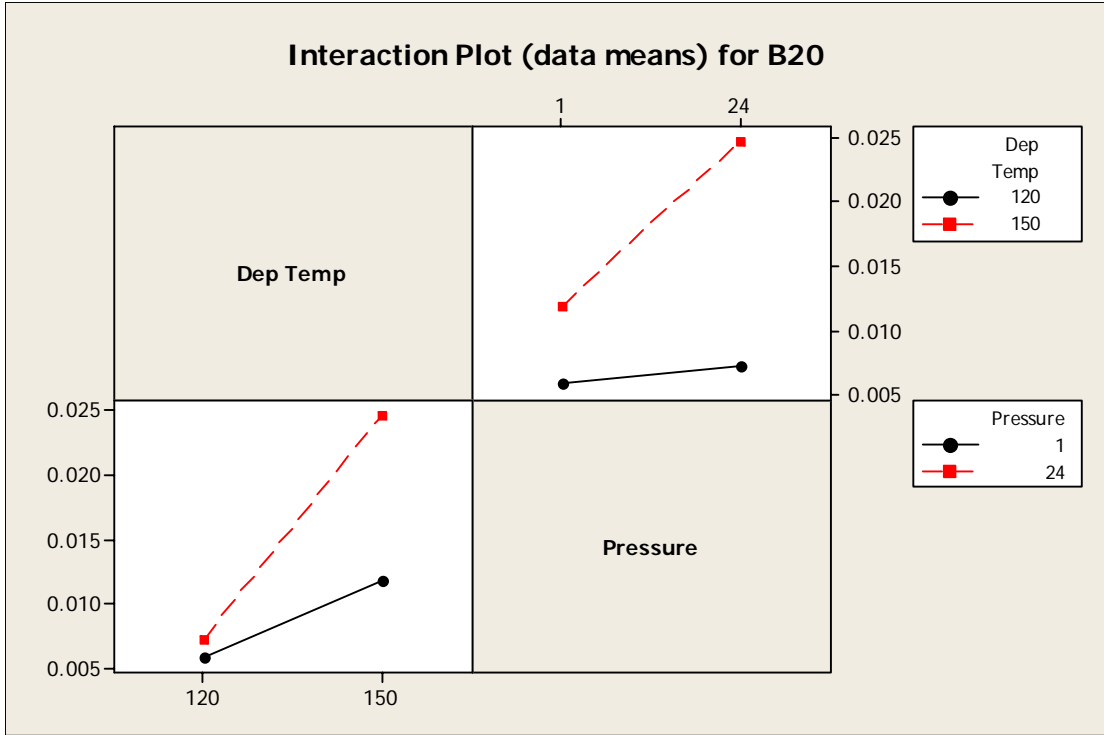


Figure 5.5 Effect of interaction of deposition temperature (120 and 150°C) and Ar gas pressure (1 and 24 mTorr) on B₂₀.

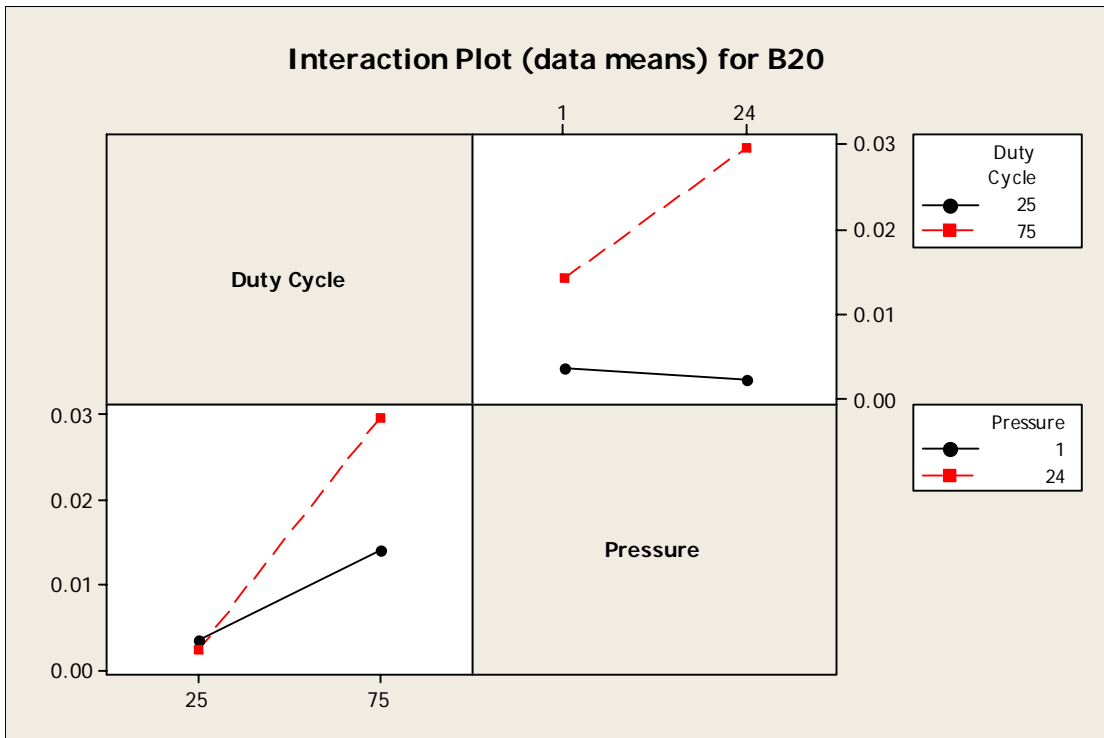


Figure 5.6 Effect of interaction of duty cycle (25 and 75%) and Ar gas pressure (1 and 24 mTorr) on B₂₀.

5.4 Discussion

The statistical significance of changes in the experimental data with interactions of the experimental parameters must be established by the choice of a suitable confidence level. The confidence level chosen for this data set is 70%, based in part as discussed in Chapter 4, on the fact that the sample film thickness may vary by $\pm 15\%$. Additionally, measurements of B_{20} have an estimated random error of $\pm 20\%$ due to sample misalignment, and sample charging during SIMS analysis may result in $\pm 20\%$ deviation in compositional data, leading to an estimated error ($[\sum x_i^2]^{1/2}$) of $\pm 30\%$. An α -level (0.30) derived from the confidence level will be compared to the p-values of each interaction's effect as described in Section 4.4. The p-values for Er and F concentration, V_{th} and B_{20} are tabulated in Table 5.2.

Table 5.2 Comparison of P-values for processing parameter interactions.

Interaction	Er conc	F conc	V_{th}	B_{20}
	P-values	P-values	P-values	P-values
Dep. T & Duty Cycle	0.758	0.625	0.75	0.039
Dep. T & Pressure	0.843	0.259	0.115	0.215
Dep. T & Annealing	0.461	0.963	0.599	0.733
Duty Cycle & Pressure	0.076	0.962	0.599	0.095
Duty Cycle & Annealing	0.717	0.61	0.468	0.336
Pressure & Annealing	0.789	0.551	0.599	0.594

Evaluating the statistical significance of each interaction, results in only 6 significant interactions out of 24 possible interactions: the interaction of duty cycle and sputtering gas pressure for Er concentration and B_{20} , the interaction of deposition temperature and duty cycle for B_{20} , and the interaction of deposition temperature and sputtering gas pressure for F concentration, V_{th} and B_{20} . Some of these interactions involve the two significant processing parameters of duty cycle and gas pressure, as

discussed in Section 4.4, and others are independent interactions with processing parameters of minor significance.

The interaction of duty cycle and Ar sputtering gas pressure as it relates to Er concentration (Figure 5.1) and B_{20} (Figure 5.6) is the result of two significant processing parameters acting together, as both duty cycle and sputtering gas pressure effect Er concentration and B_{20} independently. At the 25% duty cycle, increasing sputtering gas pressure resulted in a decrease of ~20% in the Er concentration and a decrease of ~30% in brightness. As previously described in Section 4.4, when the sputtering gas pressure is lower, negative ions (e.g. S^- or O_x^-) may be accelerated towards the deposited film with energies sufficient to cause re-sputtering of the film constituents [108]. Negative ion re-sputtering of the film primarily preferentially removes Zn, S and F, because the large mass of Er will reduce its energy transfer coefficient and therefore its sputter yield. This leads to films with higher luminescent center concentrations and crystalline damage. With the sputtering gas pressure at 1mTorr and 25% duty cycle, the Er concentration increased enough to produce a higher brightness compared to the 24 mTorr, 25% duty cycle films.

In contrast, at 75% duty cycle increasing sputtering gas pressure reduced Er concentration by ~50% but increased brightness by ~110%. In this case, the Er concentration of the films is relatively large using 75% duty cycle. Negative ion re-sputtering at the lower pressure (1 mTorr) produces a film in which Er luminescent centers are within close proximity resulting in concentration quenching. Concentration quenching is the interaction between centers resulting in non-radiative relaxation through

self-quenching, limiting the overall brightness [107]. At 24 mTorr, the reduction in re-sputtering results in limited concentration quenching greatly increasing brightness.

The interaction of deposition temperature and duty cycle as it relates to B_{20} is also the result of two significant processing parameters acting together. In this case increasing duty cycle from 25% to 75% resulted in a ~290% increase in the brightness of films deposited at 120°C (Figure 5.4). Likewise, as duty cycle was increased for films deposited at 150°C, brightness increased by ~960%. As the deposition temperature increases, Er luminescent centers have greater surface mobility making it more likely that they find the appropriate lattice position on which to activate. Film brightness is dependent on adequate dopant activation. As such, the brightness of devices deposited at 25% duty cycle increase with increasing deposition temperature. While there are a greater number of Er luminescent centers in films produced at 75% duty cycle, the lower deposition temperature limits the number of activated centers present in the film. Increasing the deposition temperature from 120°C to 150°C will result in a greater increase in brightness as the greater number of Er luminescent centers become activated. Based on the fact that brightness increases linearly with increasing duty cycle at 120°C, no concentration quenching appears to occur.

Fluorine concentration in the phosphor films is affected by duty cycle and post-deposition annealing as described in Section 4.4. Contrary to the previously described interactions, neither duty cycle nor post-deposition annealing interacts significantly with other factors to affect F concentration. However the interaction of deposition temperature and sputtering gas pressure produce a statistically significant effect in F concentration. ZnS:ErF₃ phosphor films have been shown to consist of Er luminescent centers

surrounded by a nearest neighbor shell of F ions [109]. At higher deposition temperatures, F surface mobility is increased just as Er surface mobility is increased. When Er ions find appropriate cation lattice positions, the increased surface mobility allows F ions the opportunity to find adjacent anion positions. At lower sputtering gas pressures, there is an increase in negative ion re-sputtering reducing the F concentration of the film and negating the effects of greater surface mobility. This is seen by the relatively small decrease of ~10% in F concentration as deposition temperature is increased at 1 mTorr (Figure 5.2). However, at 24 mTorr the overall effect of re-sputtering is greatly reduced, allowing for greater F incorporation (~130%) resulting from increased deposition temperature.

The effect of the interaction of deposition temperature and sputtering gas pressure on threshold voltage (Figure 5.3) is similar to that for F concentration, in that neither parameter affects threshold voltage independently. Phosphor film crystallinity should significantly affect threshold voltage. As previously described, negative ion re-sputtering results in damage to the phosphor film during deposition. The damage decreases film crystallinity. In contrast, higher deposition temperatures will result in better crystallinity as atoms are able to find appropriate lattice sites. Additionally a higher concentration of Er centers may result in both concentration quenching and inadequate activation. This results in a complex system, where evaluation of the electrical nature of the films may produce a better understanding of the parameter interaction.

The interaction of deposition temperature and sputtering gas pressure on B_{20} is, again, the interaction of two significant processing parameters. At 120°C, the brightness increased with increasing pressure by ~20%, while at 150°C brightness increased ~110%.

Negative ion re-sputtering at low sputtering pressures results in an increase in the concentration of luminescent centers and a decrease in the overall crystallinity of the phosphor film. The smaller increase in brightness with increasing sputtering gas pressure at 120°C is the result of limited dopant activation preventing significant improvement from the reduction in re-sputtering. Conversely, the better dopant activation at 150°C combined with lower re-sputtering results in substantial improvement in brightness.

5.5 Summary

In this chapter, the interactions of multiple processing parameters and their effect on B_{20} , V_{th} , Er and F concentrations in ZnS:ErF₃ films deposited using a number of different processing conditions were reported. Deposition temperature was varied between 120°C and 150°C. Duty cycle on the doped target was varied between 25% and 75%. The duty cycle on the undoped target was maintained at 100% and power applied to both targets at a 100% duty cycle was kept at 100 W. The pressure of the argon sputtering gas was varied between 1 mTorr and 24 mTorr. After deposition of the phosphor layer, half of the samples produced were annealed in nitrogen ambient for 1 hour at 425°C.

The interaction of duty cycle and sputtering gas pressure resulted in films that experience greater negative ion re-sputtering at low pressures. This increased the number of Er luminescent centers resulting in 30% improvement in brightness for 25% duty cycle films deposited at 1 mTorr compared to those deposited at 24 mTorr. For films deposited using 75% duty cycles, the increase in Er concentration limited the overall brightness due to concentration quenching. When films were deposited at 24 mTorr and 75% duty cycle, they showed a ~110% increase in brightness compared to those deposited at 1 mTorr.

The interaction of deposition temperature and duty cycle illustrated that dopant activation plays a key role in phosphor film brightness. Increasing duty cycle from 25%

to 75% at 120°C resulted in an increase of ~290%, presumably from the increase in luminescent centers. The increase in brightness at 150°C was larger, ~960%, due to the increased surface mobility of Er luminescent centers providing better dopant activation presumably from better crystallinity.

The interaction of deposition temperature and sputtering gas pressure affects the F concentration, threshold voltage and brightness of the films. While increasing deposition temperature from 120°C to 150°C results in greater surface mobility and greater F incorporation in the film, this is offset by increased negative ion re-sputtering at 1 mTorr. When re-sputtering is limited at 24 mTorr, F concentration increases by ~130% with increasing temperature. Likewise, the smaller improvement in brightness at 120°C (~20%) with increasing sputtering gas pressure is the result of lower dopant activation. At 150°C, the better dopant activation combined with the reduction in re-sputtering results in an ~110% improvement in brightness. Understanding of the interaction of deposition temperature and sputtering gas pressure's effect on threshold voltage is difficult. The effect that each parameter has on film crystallinity limits the ability to draw conclusions without better understanding of the electrical nature of the films.

CHAPTER 6 DISCUSSION

6.1 Introduction

Alternating current thin film electroluminescent (ACTFEL) devices with a ZnS:ErF₃ phosphor layer have been studied using statistical design-of-experiment (DOE) software to determine the effect of processing parameters and their interactions on electroluminescence and chemical composition. The increases in electroluminescent brightness and threshold voltages and their relationship to changes in the chemical composition of the films are discussed in this chapter.

As presented in Chapter 4, brightness at 20 volts above the threshold voltage (B_{20}) increased as each processing parameter was increased for emission at 1550 nm. The greatest increase in irradiance, from 7.4 to 46.4 $\mu\text{W}/\text{cm}^2$, occurred in films deposited at a duty cycle of 75% as compared to films deposited at a 25% duty cycle. These data are shown in Figure 4.12. These data also showed an increase in threshold voltage of ~45% from 77.5 to 113 V that was greater than for any other parameter.

The primary measure of ACTFEL device performance is optical output (irradiance). This is measured relative to the voltage at which emission begins (V_{th}). Based on literature reports, [12, 14, 54, 86, 99] the chemical composition of the film, especially erbium and fluorine concentrations, is of seminal importance to understanding the emission properties. The goal of this research is to relate the optical properties and chemical composition of the films to processing parameters. Based upon the physics of ACTFEL devices several mechanisms for increased performance will be discussed.

6.2 Processing Parameter Effects on ZnS:ErF₃ ACTFELDs

The increase in brightness of the 1550 nm NIR emission peak is a factor of two brighter for a substrate deposition temperature of 150°C versus 120°C, as shown in Figure 4.8. At the higher deposition temperature, the atomic species present on the depositing film surface will have a greater mobility and therefore are better able to find equilibrium lattice positions in the crystal [46]. The increase in brightness is the result of better activation of Er³⁺ as it substitutes for Zn²⁺ in the lattice. Little thermal desorption of Zn and S occurred; as changes in these would alter the ratio of Er/Zn. There is no significant change in the Er/Zn ratio, i.e. Er concentration, with changes in deposition temperatures, as shown in Figure 4.9. Likewise, fluorine concentration shows no significant change as a function of deposition temperature as shown in Figure 4.10.

The increase in brightness with increasing duty cycle applied to the doped target is, 7.4 to 46.4 μW/cm² as discussed above and shown in Figure 4.12. As the percentage of time over which power is applied to the doped target increases (with continuous power applied to the undoped target), the flux of dopant Er (and F) arriving at the depositing film surface and being incorporated into the deposited film will increase, resulting in higher Er and F concentrations as shown in Figures 4.13 and 4.14. The data show that changing the duty cycle from 25% to 75% resulted in an increase of ~80% and ~70% for the Er/Zn ratio and F concentration, respectively. The brightness of ACTFEL devices have been shown to scale linearly with activator concentration over a dilute concentration range [33]. Therefore an increase in the concentration of erbium in the phosphor layer is expected to result in an increase in the number of radiative events, i.e. the brightness of the device will increase with an increase in erbium concentration. At high erbium concentrations (>3% Er³⁺), there is the possibility of increased nonradiative relaxation due

to energy hopping between luminescent centers in close proximity, a phenomenon known as concentration quenching [107]. Once this concentration threshold has been reached luminescence will decrease with increasing concentration. In this study, no quenching of luminescence appeared for films doped at the highest concentration.

The increase in threshold voltage with increasing duty cycle may be attributed to greater incorporation of erbium dopant into the film. The larger size of the erbium ion (radius of Er^{3+} is 0.1 nm) substituted onto a zinc ion lattice position (radius of Zn^{2+} is 0.06 nm) results in greater distortion of the crystal lattice increasing the number of scattering events in which hot electrons may encounter before dopant ion excitation. As a result, higher threshold voltages are necessary to induce electroluminescence.

Brightness increased by 80% with increasing argon sputtering gas pressure as shown in Figure 4.16. As the sputtering gas pressure increases from 1 mTorr to 24 mTorr, little change occurs in the fluorine concentration, while a large decrease (~40%) occurs in the Er/Zn ratio as shown in Figure 4.17. This decrease is due to a higher amount of negative ion re-sputtering preferentially of Zn, S, and F at the lower Ar pressure [108]. During sputtering, Ar^+ ions are generated and accelerated towards the ZnS:ErF_3 target to cause sputtering and deposition of the phosphor film. However, if negative ions, e.g. O_x^- or S^- , are formed, they are accelerated towards the deposited film and be sufficiently energetic to cause re-sputtering of the Zn, S and/or F. In addition, some of the negative ions may be neutralized in the sputter plasma after being accelerated to high energies, and these excited neutrals may also cause re-sputtering. At lower pressures, negative ions and energetic neutrals are thus better able to maintain sufficiently high energies to cause re-sputtering of the Zn and S atoms in the deposited film. As a result, Zn and S exhibit a

larger negative ion sputter yield than does Er, leading to Er enrichment in the film deposited at low Ar pressure. Re-sputtering of the deposited surface will result in some damage to the crystal structure, limiting the ability of Er to find cation sites on which to activate [108]. The limited activation of Er will reduce the brightness of the film without great change in the threshold voltage. Given adequate time and energy, there will be diffusion of Zn and S constituents through the film to provide some healing of the damage. No change in F concentration (Figure 4.18) resulted from increasing Ar sputtering gas pressure. This is due to the relatively low concentration, <2 at%, resulting in a substantially lower probability that F will be sputtered out of the film.

Annealing phosphor films at 425°C for 1 hour resulted in an increase of 60% in brightness and no change in V_{th} as shown in Figure 4.20 and Figure 4.19, respectively. No significant change in erbium concentration occurs for samples annealed at 425°C compared to as-deposited samples (Figure 4.21), since the 2% increase is within the $\pm 15\%$ experimental error resulting from varying thickness in the film. This conclusion is reasonable since post-deposition annealing should not lead to Er removal from the film either by desorption or by diffusion. There is however a large reduction in fluorine concentration as a function of annealing, from 8.8×10^{20} to $5.1 \times 10^{20} \text{ cm}^{-3}$ as shown in Figure 4.22. Annealing has been shown to reduce the overall concentration of fluorine in ZnS:TbF₃ ACTFELDs with the suggested mechanism being diffusion and desorption [86]. This reduction in F is suggested to alter the local crystal field around the erbium luminescent centers [109]. Erbium has a nearest neighbor shell composed of F at different distances. Reduction of F results in S diffusion into the nearest neighbor shell as shown

by XAFS [109]. This change in local crystal field allows for the increase in near infrared luminescence at the expense of lower visible emission [99].

6.3 Interaction of Processing Parameter Effects

Before discussion of the interactions, it is important to understand how a number of phenomena have been shown to affect the properties of ACTFELDs. The concentration of luminescent centers has a large effect on the emission properties of ACTFELDs. At low concentrations, typically $< 1\text{mol}\%$, the luminescence increases steadily with increasing dopant concentration [33]. Once an optimum concentration is reached, increasing dopant concentration will result in decreased luminescence. Ehrmann and Campbell [107] attributed this decrease to concentration quenching which results from interactions between luminescent centers. Luminescence is also a function of the Er/F ratio. Hsu et al. determined that reduction of F in ACTFELDs enhanced luminescence and film crystallinity [86]. Proper substitution of luminescent centers also effects device brightness [46]. Dopant ions will not be activated unless properly positioned [111]. High surface mobility greatly contributes to this. Surface mobility will increase as the deposition temperature is increased. However as more large luminescent centers are incorporated into the film, film crystallinity is reduced [112].

Negative-ion bombardment during film growth can lead to changes in growth rate, surface morphology, and composition of the film through resputtering of the deposited material. Negative ion re-sputtering involves O_x^- and S^- ions being excited towards the film and striking it with enough energy to eject lower mass elements. This results in a reduction of Zn and S in the film when compared to Er and lowered film crystallinity [108]. Experimental observations have also shown the threshold voltage for ACTFELDs is related to device crystallinity. The primary source of carriers is electrons trapped at the

phosphor/insulator interface. As crystallinity is altered, through annealing or sputtering of the deposited film, the number of interfaces states is changed [14]. The relationship of these phenomena, in large part, affects the performance and composition of ACTFELDs.

The interaction of duty cycle and Ar sputtering gas pressure as it relates to Er concentration (Figure 5.1) and B_{20} (Figure 5.6) is the result of two significant processing parameters acting together, as both duty cycle and sputtering gas pressure effect Er concentration and B_{20} independently. At the 25% duty cycle, increasing sputtering gas pressure resulted in a decrease of ~20% in the Er concentration and a decrease of ~30% in brightness. In contrast, at 75% duty cycle increasing sputtering gas pressure reduced Er concentration by ~50% but increased brightness by ~110%. In this case, the Er concentration of the films is relatively large using 75% duty cycle. Negative ion re-sputtering at the lower pressure (1 mTorr) produces a film in which Er luminescent centers are within close proximity resulting in concentration quenching. At 24 mTorr, the reduction in re-sputtering results in limited concentration quenching greatly increasing brightness.

The interaction of deposition temperature and duty cycle as it relates to B_{20} is also the result of two significant processing parameters acting together. In this case increasing duty cycle from 25% to 75% resulted in a ~290% increase in the brightness of films deposited at 120°C shown in Figure 5.4. Likewise, as duty cycle was increased for films deposited at 150°C, brightness increased by ~960%. As the deposition temperature increases, Er luminescent centers have greater surface mobility making it more likely that they find the appropriate lattice position on which to activate. While there are a greater number of Er luminescent centers in films produced at 75% duty cycle, the lower

deposition temperature limits the number of activated centers present in the film. Increasing the deposition temperature from 120°C to 150°C will result in a greater increase in brightness as the greater number of Er luminescent centers become activated. Based on the fact that brightness increases linearly with increasing duty cycle at 120°C, no concentration quenching appears to occur.

Contrary to the previously interactions, neither duty cycle nor post-deposition annealing interacts significantly with other factors to affect F concentration. However the interaction of deposition temperature and sputtering gas pressure produce a significant effect in F concentration. ZnS:ErF₃ phosphor films have been shown to consist of Er luminescent centers surrounded by a nearest neighbor shell of F ions [109]. At higher deposition temperatures, F surface mobility is increased just as Er surface mobility is increased. When Er ions find appropriate cation lattice positions, the increased surface mobility allows F ions the opportunity to find adjacent anion positions. At lower sputtering gas pressures, there is an increase in negative ion re-sputtering reducing the F concentration of the film and negating the effects of greater surface mobility. This is seen by the relatively small decrease of ~10% in F concentration as deposition temperature is increased at 1 mTorr shown in Figure 5.2. However, at 24 mTorr the overall effect of re-sputtering is greatly reduced, allowing for greater F incorporation (~130%) resulting from increased deposition temperature.

The effect of the interaction of deposition temperature and sputtering gas pressure on threshold voltage (Figure 5.3) is similar to that for F concentration, in that neither parameter affects threshold voltage independently. Phosphor film crystallinity should significantly affect threshold voltage. As previously described, negative ion re-sputtering

results in damage to the phosphor film during deposition. The damage decreases film crystallinity. In contrast, higher deposition temperatures will result in better crystallinity as atoms are able to find appropriate lattice sites. Additionally a higher concentration of Er centers may result in both concentration quenching and inadequate activation. This results in a complex system, where evaluation of the electrical nature of the films may produce a better understanding of the parameter interaction.

The interaction of deposition temperature and sputtering gas pressure on B₂₀ is, again, the interaction of two significant processing parameters. At 120°C, the brightness increased with increasing pressure by ~20%, while at 150°C brightness increased ~110% as shown in Figure 5.5. Negative ion re-sputtering at low sputtering pressures results in an increase in the concentration of luminescent centers and a decrease in the overall crystallinity of the phosphor film. The smaller increase in brightness with increasing sputtering gas pressure at 120°C is the result of limited dopant activation preventing significant improvement from the reduction in re-sputtering. Conversely, the better dopant activation at 150°C combined with lower re-sputtering results in substantial improvement in brightness.

6.4 Statistical Data Analysis

This study utilizes a statistical software package, Minitab, to design the experiments and analyze the data from simultaneous variation of experimental parameters [106]. The design-of-experiments used a factorial experiment method. A factorial experiment is a statistical study in which each observation is categorized according to more than one factor [107]. This experiment allows analysis of the effect of each factor on the response variables. For this study the factors investigated were deposition temperature, duty cycle on the doped target, sputtering gas pressure and post-deposition

annealing. The response variables were threshold voltage, brightness at 20 V above threshold and erbium and fluorine concentrations. Factorial design also allows investigation of the effect of interaction between factors on the response variables. If the number of experiments needed is very large, a fractional factorial design may be used that employs a limited number of experiments performed over a specific confidence interval to extrapolate experiments that were not performed.

Main effects plots were utilized to determine the magnitude that each factor contributed to the response variables. For each factor the average of the low level data was calculated and subtracted from the average of the high level data. This allows a calculation of the percent change as the factor is increased. In this study, main effects plots were used to quantify the effect of each experimental factor on the response variables. This provided a method by which comparisons could be addressed.

The use of statistical analysis must be evaluated after experimental data has been collected to determine if any systematic error has resulted from the analysis method. To do this, a variety of techniques may be used. For this study, normal probability plots and plots of residuals versus order were used. A normal probability plot is a plot of the expected order of the data against the data actual data. For a normally distributed population, the normal probability plot should approximate a straight line. A wide normal distribution signifies a data set with a large amount of deviation from the mean. The normal probability plots for V_{th} , B_{20} , Er/Zn ratio and F concentration are shown in Figures 4.28, 4.29, 4.30 and 4.31, respectively [110]. There are no apparent deviations from the normal distributions for this data, i.e. outliers, change in slope, justifying the use of the data in the study.

The plot of residuals versus order of data collection was also used to evaluate the possibility of error in this work. Residuals are the deviation of each sample from the overall sample average for each response variable. These are plotted relative to the order in which each experiment was performed. This plot is used to determine if the time at which the data was taken affected the response variable or if the previous experiment altered the effect of the current experiment. The residuals should fluctuate randomly around the center line. The residual versus order plots for V_{th} , B_{20} , Er/Zn ratio and F concentration are shown in Figures 4.32, 4.33, 4.34 and 4.35, respectively [110]. The data fluctuate randomly about the center, showing that the data show no time dependent effects.

CHAPTER 7 CONCLUSIONS

7.1 Processing Parameter Effects

ZnS:ErF₃ alternating current thin film electroluminescent (ACTFEL) devices were fabricated using RF plasma magnetron sputtering. Films were deposited using an undoped ZnS target and a doped ZnS:(1mol%)ErF₃ target simultaneously. The effects of increasing deposition temperature, duty cycle on the doped target and sputtering gas pressure all showed increases in the 1.55 μm near infrared (NIR) electroluminescence (EL) irradiance. Additionally, post-deposition annealing of ACTFEL devices at 425 $^{\circ}\text{C}$ for 1 hr also improved the NIR EL irradiance. These changes in processing parameters resulted in changes in the Er and F concentrations in the films. A design-of-experiments with a factorial method was used to determine the effects of each variable with a limited number of experiments.

Irradiance increased, from 16.8 to 46.4 $\mu\text{W}/\text{cm}^2$ (~180%), as deposition temperature was increased from 120 $^{\circ}\text{C}$ to 150 $^{\circ}\text{C}$, while the threshold voltage for EL remained relatively constant. Chemical analysis of the film showed no change in the erbium or fluorine concentration at the higher deposition temperatures. The increase in brightness is attributed to greater mobility of atomic species on the growing surface allowing erbium to find equilibrium activator lattice positions in the crystal.

The greatest increase in irradiance (from 7.4 to 55.9 $\mu\text{W}/\text{cm}^2$ or 650%) occurred as the duty cycle applied to the doped target was increased from 25% to 75%. The threshold voltage also increased from 77.5 to 113V (45%) with increasing duty cycle. As the

percentage of time over which power was applied to the doped target increased, the number of dopant ions incorporated into the film increased. As a result the Er and F concentration increased by 80% and 70%, respectively. With a larger number of luminescent centers in the film, there was a greater probability of EL emission. The increase in threshold voltage is postulated to result from an increase in the distortion of the crystal lattice resulting in a greater number of scattering events.

Irradiance increased from 22.7 to 40.6 $\mu\text{W}/\text{cm}^2$ (80%) as sputtering gas pressure was increased from 1 mTorr to 24 mTorr. Threshold voltage remained constant and little change occurred in F concentration at $\sim 7.2 \times 10^{20} \text{ cm}^{-3}$, while the Er concentration was reduced by 40%. These changes are attributed to greater negative ion re-sputtering at lower pressures. The longer mean free path at low gas pressure allows higher energy particles to strike the growing film surface and remove Zn, S and F from the film. This process results in a higher Er concentration at low pressures, but also a greater amount of physical damage to the crystal lattice. This damage probably increases the number of inelastic scattering events between the ballistic electrons and the lattice, resulting in lower excitation probability and reduced luminescence.

Post-deposition annealing at 425°C resulted in increased brightness from 24.8 to 38.8 $\mu\text{W}/\text{cm}^2$ (60%). There were no significant changes in the threshold voltage or Er concentration. However the F concentration was reduced from 8.8×10^{20} to 5.1×10^{20} atoms/ cm^{-3} (40%) as a result of annealing. The increase in brightness is attributed to better activation of Er luminescent centers in the film. Some enhancement in irradiance may also be due to the reduction in fluorine. By reducing the fluorine concentration of the film the nearest neighbor shell around the erbium ions is changed. This may alter the

erbium bonds from highly ionic Er-F to a more polar covalent Er-S bond. Though the erbium $4f-4f$ transitions are shielded, alterations of the local crystal field likely result in enhancement of the NIR transitions. Reduction of F results in S diffusion into the nearest neighbor shell. This change in local crystal field should result in higher oscillator strengths for the ${}^4I_{13/2} \rightarrow {}^4I_{15/2}$ transition at 1550 nm, which increases the overall near infrared luminance at the expense of lower visible emission [99].

7.2 Processing Parameter Interactions

The interaction of duty cycle and Ar sputtering gas pressure as it relates to Er concentration and B_{20} is the result of two independently significant processing parameters acting together. At the 25% duty cycle, increasing sputtering gas pressure resulted in a ~20% decrease in the Er concentration and a ~30% decrease in brightness. At 75% duty cycle, increasing sputtering gas pressure reduced Er concentration by ~50% but increased brightness by ~110%. In this case, the Er concentration of the films is relatively large using 75% duty cycle. Negative ion re-sputtering at the lower pressure (1 mTorr) likely produces a film in which Er centers are within close proximity resulting in concentration quenching. At 24 mTorr, the reduction in re-sputtering results in limited concentration quenching greatly increasing brightness.

In the case of interaction of deposition temperature and duty cycle as it relates to B_{20} , increasing duty cycle from 25% to 75% resulted in a ~290% increase in the brightness of films deposited at 120 °C. As duty cycle was increased for films deposited at 150 °C, brightness increased by ~960%. As the deposition temperature increases, Er luminescent centers have greater surface mobility making it more likely that they find the appropriate lattice position on which to activate. While there are a greater number of Er luminescent centers in films produced at 75% duty cycle, the lower deposition

temperature probably limits the number of activated centers present in the film.

Increasing the deposition temperature from 120 °C to 150 °C should result in a greater increase in brightness as the greater number of Er luminescent centers become activated. Based on the fact that brightness increases linearly with increasing duty cycle at 120 °C, no concentration quenching appears to occur.

The interaction of deposition temperature and sputtering gas pressure produce a significant effect in F concentration. At higher deposition temperatures, F surface mobility should be increased just as Er surface mobility is increased which allows F ions the opportunity to find adjacent anion positions. At lower sputtering gas pressures, there should be an increase in negative ion re-sputtering reducing the F concentration of the film and negating the effects of greater surface mobility. This is seen by the relatively small decrease of ~10% in F concentration as deposition temperature is increased at 1 mTorr however, at 24 mTorr the overall effect of re-sputtering is greatly reduced, allowing for greater F incorporation (~130%) resulting from increased deposition temperature.

The effect of the interaction of deposition temperature and sputtering gas pressure on threshold voltage is similar to that for F concentration, in that neither parameter affects threshold voltage independently. Phosphor film crystallinity should significantly affect threshold voltage. As previously described, negative ion re-sputtering should result in damage to the phosphor film during deposition. The damage decreases film crystallinity. In contrast, higher deposition temperatures should result in better crystallinity as atoms are able to find appropriate lattice sites. Further evaluation of the

electrical nature of the films may produce a better understanding of the parameter interaction.

In the interaction of deposition temperature and sputtering gas pressure on B₂₀, at 120 °C, the brightness increased with increasing pressure by ~20%, while at 150 °C brightness increased ~110%. Negative ion re-sputtering at low sputtering pressures should result in an increase in the concentration of luminescent centers and a decrease in the overall crystallinity of the phosphor film. The smaller increase in brightness with increasing sputtering gas pressure at 120 °C is probably the result of limited dopant activation preventing significant improvement from the reduction in re-sputtering. Conversely, the better dopant activation at 150 °C combined with lower re-sputtering results in substantial improvement in brightness.

7.3 Experimental Evaluation

The brightest device was produced using a deposition temperature of 150 °C, a duty cycle of 75%, an argon sputtering gas pressure of 24 mTorr and post-deposition annealing at 425 °C for 1 hour in ultra high purity nitrogen. This resulted in a luminance at 1550 nm of 146.46 $\mu\text{W}/\text{cm}^2$ at 20 V above threshold.

This study utilized a statistical software package, Minitab, to design the experiments and analyze the data from simultaneous variation of experimental parameters. The design-of-experiments used a factorial experiment method. Main effects plots were utilized to determine the magnitude that each factor contributed to the response variables. For each factor the average of the low level data was calculated and subtracted from the average of the high level data. For this study, normal probability plots and plots of residuals versus order were used to determine if any systematic error resulted from the analysis method. There are no apparent deviations from normal distributions for

these data, i.e. no outliers and no change in slope, justifying the use of the data in the study. The data also fluctuate randomly as a function of order, therefore the data show no time dependent effects. As such the statistical methods used in this research is valid.

7.4 Future Work

Additional work is needed to determine if the mechanisms postulated in this study adequately describe the observations. To do this, measurements of the electrical properties of charge versus voltage, Q-V plots, are needed. Q-V plots provide a better understanding of the flow of electrons as voltage is applied to the device. This allows for determination of conduction charge, relaxation charge and leakage charge across the phosphor layer. These charge values give direct measurement of when current flow across the device begins, the amount of charge that flows when the voltage reaches the maximum and the amount of charge that escapes from shallow interface states at zero voltage.

Q-V data can also be used to determine a number of useful parameters about the ACTFEL device. First, the slope of the Q-V plot below the threshold voltage is equal to the total capacitance of the device. Second, above the threshold voltage the phosphor is considered a conductor and the slope of the Q-V plot is used to measure the capacitance of the insulating layers. If the device is not completely shorted, however, the slope will be greater than that of the insulating layers themselves as it will incorporate some residual component of the phosphor layer. Also if there is a build-up of space charge in the phosphor, the slope will be larger than the insulator capacitance [83]. Third, the area inside the Q-V plot is proportional to the input electrical power density delivered per pulse [100].

LIST OF REFERENCES

1. Kobayashi, H., and S. Tanaka, J. SID, 1996. 4(3): p. 157-163
2. Mauch, R.H., J. SID, 1997. 5(3): p. 173-178.
3. Rack, P.D., A. Naman, P.H. Holloway, S.S. Sun and R.T. Tuenge, MRS Bulletin, 1996. 21(3): p. 49-58.
4. Ono, Y.A., Annual Reviews Materials Science, 1997. 27: p. 283-303.
5. King, C.N., J. SID, 1996. 4(3): p. 153-153.
6. Mach, R. and G.O. Mueller, Semiconductor Science and Technology, 1991. 6: p. 305-323.
7. Parker, D.W., A.G. Knapp and T.S. Baller, IEE Conf. Pub., 1997. CP447: p. 575-580.
8. Anderson, M.T., R.J. Walko and M.L.F. Philips, Materials Research Society Symposium, 1995. 345: p. 269.
9. Kester, D.J. and R. Messier, J. Vac. Sci. Tech. A, 1986. 4(3): p. 496-499.
10. Smith, S.D., A. Vass, P. Bramley, J.G. Crowder and C.H. Wang, IEE Proc. Optoelectron, 1997. 144: p. 266.
11. Lord Bowden of Chesterfield, IEE Proceedings, 1985. 32: p. 436.
12. Ono, Y.A., *Electroluminescent Displays*, 1995, Singapore: World Scientific Publishing Co.
13. Tannas, L.E., *Flat-Panel Displays and CRT's*, 1985, New York: Van Nostrand Reinhold. 468.
14. Rack, P.D. and P.H. Holloway, Materials Science and Engineering, 1998. R21(4): p.171-219.
15. Saleh, B.E.A. and M.C. Teich, *Fundamentals of Photonics*, 1991, New York: John Wiley and Sons Inc.
16. Sakai, R., T. Katsumata, S. Komuro and T. Morikawa, J. Luminescence, 1999. 85: p. 149.

17. Kim, D-J., H-M. Kim, M-G. Han, Y-T. Moon, S. Lee and S-J. Park, *J. of Vac. Sci. Technol.*, 2003. B21: p. 641.
18. Tomilin, M.G., *J. Optical Tech. (A Translation of Opticheski Zhurnal)*, 2003. 70: p. 454.
19. Hitt, J.C., J.P. Bender and J.F. Wager, *Crit Rev Sol State & Mat. Sci.*, 2000. 25: p. 29.
20. Destriau, G., *J. Chim. Phys.*, 1936. 33: p. 587.
21. Vecht, A., *Journal of Applied Physics*, 1968. 1: p. 134.
22. Kahng, D., *Applied Physics Letters*, 1968. 13: p. 210.
23. Russ, M.J. and D.I. Kennedy, *J. Electrochem. Soc.*, 1967. 114: p. 1066.
24. Inoguchi, T., M. Takeda, Y. Kakihara, Y. Nakata and M. Yoshida, *SID Digest*, 1974: p. 84-95.
25. Uede, H., Y. Kanatani, H. Kishishita, A. Fujimori and K Okano, *SID Digest*, 1981: p. 28.
26. Takeda, M., Y. Kanatani, H. Kishishita, T. Inoguchi and K. Okano, *SID proceedings*, 1981. 57: p. 22.
27. Mito, S., C. Suzuki, Y. Kanatami and M. Ise, *SID 74 Digest International Symposium*, 1974: p. 86-87.
28. Jayaraj, M.K. and C.P.G. Vallabhan, *J. Electrochem. Soc.*, 1991. 138(5): p. 1512-1516.
29. Kobayashi, H., S. Tanaka, V. Shanker, M. Shiiki, T. Kunou, J. Mita and H. Sasakura, *Physica Status Solidi A- Applied Research*, 1985. 88(2): p. 713-720.
30. Leskela, M., *J. Alloys and Compounds*, 1998. 275: p. 702.
31. Shikada, M., *Telecommunications*, 1992. 26: p. 4.
32. Goodnick, S.M., M. Dur, R. Redmer, M. Reigrotzki and N. Fitzer, *Proceed. of SPIE*, 2000. 3940: p. 217.
33. Keir, P.D., C. Maddix, B.A. Baukol, J.F. Wager, B.L. Clark and D.A. Keszler, *J. Appl. Phys.*, 1999. 86: p. 6810.
34. Ronda, C.R., T. Justel and H. Nikol, *Journal of Alloys and Compounds*, 1998. 277: p. 669-676.

35. Silveira, J.P. and F. Grasdepot, *Infrared Physics & Technology*, 1996. 37(1): p. 143-147.
36. Perdotti, F.L., S.J. Leno and S. Perdotti, *Introduction to Optics*, 2nd ed., 1987, Englewood Cliffs, NJ: Prentice-Hall.
37. Godlewski, M. and M. Leskela, *Crit. Rev. Solid State Mater. Sci.*, 1994. 19: p. 199.
38. Ochiai, S., T. Kato, T. Ogawa, K. Kojima, Y. Uchida, A. Ohashi, M. Ieda and T. Mizutani, *Conf. on Elec. Ins. and Dielec. Phenom.*, 1994. p. 681.
39. Haaranen, J., R. Tornqvist, J. Koponen, T. Pitänen, M. Surma-aho, W. Barrow and C. Laakso, *SID 92 Digest*, 1992. 23: p. 348.
40. Khormanei, R., S. Thayer, K. Ping, G. Dolney, A. Ipri, F.L. Hsueh, R. Stewart, T. Keyser, G. Becker, D. Kagey and M. Spitzer, *SID 94 Digest*, 1994. 25: p. 137.
41. Wu, X., *EL*, 1996. 96: p. 285.
42. Minami, T. *Display and Imaging*, 1999. 8, suppl.: p. 83-93.
43. Moorehead, D., *Optical and electrical characterization of alternating current thin film electroluminescent displays*, M.S. thesis. 2000, University of Florida.
44. Bringuier, E., *J. Appl. Phys.*, 1994. 75(9): p. 4291-4312.
45. Okamoto, S., E. Nakazawa and Y. Tsuchiya, *Japanese Journal of Applied Physics Part 1- Regular Papers Short Notes & Review Papers*, 1989. 28(3): p. 406-409.
46. Sze, S.M., *Physics of Semiconductor Devices*, 2nd ed., 1981, New York: Wiley Interscience.
47. Kittel, C., *Introduction to Solid State Physics*, 6th ed., 1986, New York: John Wiley and Sons, Inc.
48. Brennan, K., *J. Appl. Phys.*, 1998. 64(8): p. 4024-4030.
49. Mach, R. and G.O. Mueller, *Journal of Crystal Growth*, 1990. 101: p. 967-975.
50. Bhattacharyya, K. S.M. Goodnick and J.F. Wager, *J. Appl. Phys.*, 1993. 73(7): p. 3390-3395.
51. Bringuier, E., *J. Appl. Phys.*, 1991. 70(8): p. 4505-4512.
52. Baraff, G.A., *Phys Rev.*, 1962. 128(6): p. 2507-2517.
53. Wager, J.F. and P.D. Keir, *Ann. Rev. Mater. Sci.*, 1997. 27: p. 223-248.

54. Blasse, G. and B.C. Grabmaier, *Luminescent materials*, 1994, Berlin: Springer-Verlag.
55. Harkonen, G., M. Leppanen, E. Soininen, R. Tornqvist and J. Viljanen, *Journal of Alloys and Compounds*, 1995. 225(1-2): p. 552-554.
56. Mayer, J.W., *Electronic Materials Science: For Integrated Circuits in Si and GaAs*, 1990, New York: Macmillan.
57. Holloway, P.H. and S.L. Jones, *Journal of Surface Anal.*, 1998. 3(2): p. 226-231.
58. Stevens, H. 2000, Dow Corning, Inc.
59. Keir, P.D., *Fabrication and characterization of ACTFEL devices*, M.S. thesis. 1999, Oregon State University: Corvallis.
60. Prazision Glass & Optics, <http://www.pgo-online.com>, retrieved January 2006.
61. Alt, P.M., *SID Digest*, 1984. p. 79.
62. Ono, Y., *Encyclopedia of Applied Physics*. Ed. G.L. Trigg. 1993, New York: VCH publishers.
63. Ono, Y., *SID Seminar lecture notes, Volume II, F-1, F-1/1*, 1993.
64. Ono, Y. *Progress in Information Display Technology*, ed. S. Kobayashi. Vol. 1. 1995, Singapore: World Scientific Publishing Co.
65. Howard, W.E., *IEEE Transactions on Electron Devices*, 1977. ED-24: p.903.
66. Tiku, S.K. and G.C. Smith, *IEEE Transactions on Electron Devices*, 1984. ED-31.
67. Callister, W.D., *Materials Science and Engineering, An Introduction*, 1997, New York: John Wiley and Sons, Inc.
68. Keir, P.D., H. Le, R.L. Thuemler, H. Hitt and J.F. Wager, *Appl. Phys. Lett.*, 1996. 2421.
69. Kim, H. and C.M. Gilmore, *J. Appl. Phys.*, 199. 86(11): p. 6451-6461.
70. Honda, S., A. Tsujimoto, M. Watamori and K. Oura, *J. Vac. Sci. Tech. A*, 1995. 13(3): p. 1100-1103.
71. Suzuki, M., Y. Maeda, M. Muraoka, S. Higuchi and Y. Sawada, *Mater. Sci. Eng. B*, 1998. 54: p.43-45.
72. Jia, Q.X., J.P. Zheng, H.S. Kwok and W. A. Anderson, *Thin Solid Films*, 1995. 258: p. 260-263.

73. Kamei, M. Y. Shigesato, I. Yasui, N. Taga and S. Takaki, *J. Non-Crystalline Solids*, 1997. 218: p. 267-272.
74. Laux, S., N. Kaiser, A. Zoller, R. Gotzelmann, H. Lauth and H. Bernitzki, *Thin Solid Films*, 1998. 335: p. 1-5.
75. Tominaga, K., T. Ueda, T. Ao, M. Kataoka and I. Mori, *Thin Solid Films*, 1996. 281-282: p. 194-197.
76. Utsumi, K., O. Matsunaga and T. Takahata, *Thin Solid Films* 1998. 334: p.30-34.
77. Aduodija, F., H. Izumi, T. Ishihara and H. Yoshioka, *Appl. Phys. Lett.*, 1999. 74(20): p. 3059-3061.
78. Paine, D.C., T. Whitson, D. Janiac, R. Beresford and C. Ow Yang, *J. Appl. Phys.*, 1999. 85(12): p. 8445-8450.
79. Chopra, K.L., S. Major and D.K. Pandya, *Thin Solid Films*, 1983. 102: p. 1.
80. Rack. P.D., A. Namen, P.H. Holloway, S-S. Sun and R.T. Tuenge, *MRS Bulletin*, 1996. 21: p. 49.
81. Nakamura, S., Y. Yamada and T. Taguchi, *J.Cryst. Grow*, 2000. 214: p. 1091.
82. Georgobiani, A.N., A.N. Gruzintsev, C. Barthou, P. Benalloul, J. Benoit, B.G. Tagiev, O.B. Tagiev and R.D. Zhabborov, *Journal of the Electrochemical Society*, 2001. 148(11): p. H167-H170.
83. Smith, D.H., *J. Luminescence*, 1981. 23: p. 209.
84. Oberacker, T.A. and H.W. Schock, *J. of Cryst. Growth*, 1996. 159: p. 935-938.
85. Sohn, S.H., D.G. Hyun, A. Yamada and Y Hamakawa, *Appl. Phys. Lett.*, 1993. 62(9): p. 991-993.
86. Hsu, C.T., Y.J. Lin, Y.K. Su and M. Yokoyama, *Jpn. J. Appl. Phys.*, 1993. 93: p. 1983-1986.
87. Hirate, T., T. Ono and T. Satoh, *SID International Disp. Res. Conf.*, 2002. p.693.
88. Drum, K.A., K. Dovidenko, A.W. Topol, G.S. Shekhawat, R.E. Geer and A.E. Kaloveros, *MRS Symp. Proc.*, 2002. 695: p. 41.
89. Wang, Y-J., C-X. Wu, M-Z. Chen and M-C. Huang, *J. Appl. Phys.*, 2003. 93: p. 9625.
90. Lide, D.R., and H.P.R. Freerike, eds. *CRC Handbook of Chemistry and Physics 78th ed.*, 1997, Boca Raton: CRC Press.

91. Potenza, M., IEEE Communications Magazine, 1996. 34: p. 96.
92. Favennec, P.N., H. L'Haridon, M. Salvi, D. Moutonnet and Y. Le Guilou, Electron. Lett., 1989. 25: p.718.
93. Neuhalfen, A.J. and B.W. Wessels, Appl. Phys. Lett., 1992. 60: p. 2657.
94. Choyke, W.J., R.P. Devaty, L.I. Clemen, M. Yoganathan, G. Pensl and C. Hassler, Appl. Phys. Lett., 1994. 65: p. 1668.
95. Coffa, S., A. Polman and R.N. Schwartz, eds. *Mater. Res. Symp. Proc., Vol. 422*, 1996, Pittsburgh: MRS.
96. Zavada, J.M. and D. Zhang, Solid-state Electron, 1995. 38: p. 1285.
97. Hoven, G.N.v.d., E. Snoeks, A. Polman, C. van Dam, J.W.M. van Uffelen and M.K. Smith, Journal of Applied Physics, 1995. 79(3): p. 1258-1266.
98. Chase, E.W., R.T. Hepplewhite, D.C. Krupka and D. Kahng, Journal of Applied Physics, 1969. 40(6): p. 2512-2519.
99. Kale, A., N. Shepherd, D. DeVito, W. Glass, M. Davidson and P.H. Holloway, Journal of Applied Phys., 2003. 94(6): p. 3147-3152.
100. Ono, Y.A., H. Kawakami, M. Fuyama and K. Onisawa, Jpn. J. Appl. Phys, 1987. 26: p. 1482.
101. Brundle, C.R., J.C.A. Evans and S. Wilson, *Encyclopedia of Materials Characterization*, Materials Characterization Series, ed. J.C.A. Evans, 1992, Boston: Butterworth-Heinemann.
102. Newbury, D.E., D.C. Joy, P. Cechlin, C. Fiori and J.I. Goldstein, *Advanced Scanning Electron Microscopy and X-ray Microanalysis*, 1986, New York: Plenum Press.
103. Goldstein, J.I., D. Newbury, P. Cechlin, D.C. Joy, C.E. Lyman, E. Lifshin, L. Sawyer, J.R. Michael and M. Staniforth, *Scanning Electron Microscopy and X-ray Microanalysis*, 1981, New York: Plenum Press.
104. Minitab, Inc., <http://www.minitab.com>, retrieved March 2006.
105. Vining, G.G., *Statistical Methods for Engineers*, 1998, Pacific Grove: Brooks/Cole Publishing.
106. Zhang, J.H. and X.W. Fan, Journal of Crystal Growth, 1992. 121: p.769.
107. Ehrmann, P.R. and J.H. Campbell, J. Am. Ceram. Soc., 2002. 85: p. 1061.
108. Kester, D.J. and R. Messier, J. Vac. Sci. Tech. A, 1986. 4(3): p. 496-499.

109. Stoupin, S., M. Davidson, J. Collingwood, A. Kale, D. DeVito and P. Holloway, *to be published*, 2006.
110. Hines, W.W. and D.C. Montgomery, *Probability and Statistics in Engineering and Management Science*, 1990, New York: John Wiley & Sons.
111. McKelvey, J.P., *Solid State Physics for Engineering and Materials Science*, 1993, Malabar: Krieger Publishing.
112. Glass, W.R., *Sputter Deposition of Rare Earth Doped Zinc Sulfide for Near Infrared Electroluminescence*, Ph.D. dissertation, 2003, University of Florida: Gainesville.

BIOGRAPHICAL SKETCH

David Michael DeVito was born in Winter Haven, Florida, on December 7, 1977. He lived in Winter Haven until 1992 when he moved to Agana, Guam. He returned to Winter Haven in 1993 and graduated from Winter Haven High School in 1996.

He attended the University of Florida from 1996 until 2001, when he graduated with a Bachelor of Science degree in materials science in engineering specializing in polymer science with a minor in business. During his undergraduate studies he interned with Cargill, Inc. in Frostproof, Florida, working in chemical engineering of citrus juice processing.

After receiving his bachelor's degree, he was admitted to the University of Florida, Department of Materials Science and Engineering, in August 2001 for graduate work. In the summer of 2002, he joined Dr. Paul Holloway's research group and worked on the development of near infrared alternating current thin film electroluminescent (ACTFEL) phosphors. He received his Ph.D. from the Department of Materials Science and Engineering at the University of Florida under the advisement of Dr. Paul H. Holloway in May 2006.